Examining Unusual Ground States in Transition Metal Compounds

A Thesis submitted for the degree of
Doctor of Philosophy
in
Physics (Theoretical)
by

Krishnendu Patra

Department of Physics
University of Calcutta
2025

Dedicated to my parents,
who have been my guiding light.

Acknowledgement

I would like to express my heartfelt gratitude to my supervisor Prof. Priya Mahadevan for her continuous guidance and support throughout my Ph.D. journey. I am deeply thankful to her for choosing me as a Ph.D. student and mentoring me with such dedication. Her numerous treats and kind gestures always served as a source of motivation and energy for my research. I owe an eternal debt of gratitude to my parents for their unwavering support, countless sacrifices, and constant encouragement. I also acknowledge my wife, Riya, for always standing beside me with patience, love, and strength. I am grateful to my collaborators, Dr. Nitesh Kumar, Dr. Debraj Choudhury, Dr. Srimanta Middey, and Prof. Ferdi Aryasetiawan, for their valuable collaborations and fruitful discussions. I sincerely thank Sagar da, Banik Rai, Ranjan Kumar Patel, Pratap da, and Viktor Christianson for engaging discussions and their generous help. To the PM group, my deep thanks go to Poonam di for her invaluable support. I also extend my gratitude to Sumanti di for her motivation, encouragement, and physics discussions. Prasun da has been a constant source of inspiration. Our discussions on physics and coding were always enlightening, and his academic help was priceless. I appreciate Debayan da for his kind personality and his support in various aspects of my Ph.D. life. I acknowledge my Shivam Mishra and my juniors, Shinjini, Maitrayee, Sanuja, Shivam Jani, Madhurita for their invaluable assistance and constant willingness to help. I also thank my super juniors Kaustav, Anurag and Anita. A special thanks to my "Fantastic Five" group. Without them, it would have been impossible to navigate the challenges of Ph.D. life. Samir's calmness, Riks' unique personality, Manodip's hard work, and Anirban's positivity have always uplifted me. Their support and our endless gossip sessions made this journey more bearable. From Mandarmani to the Radhachura chhaad, life is more beautiful when they are with you. From anxiety attacks to the excitement of publishing a paper, they have been there. I also thank Ramu and Samrat. Ramu has been my TT (table tennis) guru,without him, my TT season at SN Bose would never have started. To my second-floor bay members, thank you for being like a second family. Premasish's determination inspired me, and I learned a lot about paper reading and writing from him. Tanmoy's thoughtful nature and communication style helped me immensely. Apart from that, he was also a great roommate whose cheerful mood always kept the room's environment light and pleasant. Dibyendu and Krishnendu gave me a new direction in coding, they were always ready for any technical to reasech support and late-night food breaks. Krishnendu also doubled as my TT coach, and Dibyendu's consistent coffee-making kept my night research sessions alive. Even during times of depression, I was always eager to go to the bay because of the companionship and support of my baymates. I thank Sayari and Sutanu for being a great baymate and also acknowledge Shobhan da for his support. I

extend my heartfelt thanks to Dulal da and Utpal da for their tea services,without them, research wouldn't have felt complete. I also thank the SNB mess cooking team, especially Kajol, and highly appreciate Hari da for keeping us energized with his coffee service. I would like to acknowledge Barnabha and Swarup. Although we did not pursue our PhDs together, their friendship has been truly invaluable. I also extend my gratitude to Sweta for her support in various non-academic matters. I acknowledge my school friends, Akash, Subharanjan, and Sheelbhadra and my brother Raju for their constant support. Lastly I acknowledge SNBNCBS.

Krishnendu Patra

Abstract

Transition metal compounds display diverse unusual electronic, magnetic, and structural properties. In this thesis, we investigate several such systems using density functional theory (DFT) and tight-binding models to understand their ground states. We first study rare-earth nickelates ($RENiO_3$), which exhibit a temperature-driven metal-insulator transition accompanied by bond disproportionation. Using $NdNiO_3$ as a prototype, we show that this disproportionated phase, characterized by inequivalent Ni sites and parametrized by negative charge-transfer energy (Δ), remains stable under moderate hole/electron doping. Carriers tend to localize on specific Ni atoms, preserving the overall lattice structure, as the change in Δ is site-dependent and remains small within the regime where bond disproportionation persists. We propose that this localization can be experimentally detected through X-ray absorption spectroscopy at the Ni K-absorption edge. Next, we explore the magnetic ground state of Ca_3CoMnO_6, which belongs to the $Ca3Co_{2-x}Mn_xO_6$ series. Although the $\uparrow\uparrow\downarrow\downarrow$ order near $x = 1$ is not the ground state, we show that cation disorder can stabilize this multiferroic configuration even at $x = 1$ and the reason for the stabilization is also elucidated. We then examine Fe-intercalated $2H$-$NbSe_2$. Upon Fe intercalation, magnetic ordering emerges in this system. We investigate the antiferromagnetic ground state in 25% intercalated $NbSe_2$ using DFT+U calculations and a multiband Hubbard model. We identify the key exchange pathways responsible for the antiferromagnetic order. In CrSb, we investigate the direction-dependent conduction polarity (DDCP), where electrons and holes dominate transport in orthogonal directions. DFT results suggest this arises from a multicarrier mechanism inherent to the band structure with spin-orbit coupling. Finally, we study RhSi, a chiral topological semimetal hosting multifold Weyl points. GGA+U calculations reveal a low-energy double-hump feature originating from Rh d–Rh d and Rh d–Si p interactions. This double hump causes multiple Lifshitz transitions. Slight doping significantly alters the Fermi surface topology, with implications for thermal transport. Tuning the Si p levels suppresses this feature.

List of Publications

1. **Hole doping in a negative charge transfer insulator**
   Ranjan Kumar Patel*, Krishnendu Patra*, Shashank Kumar Ojha, Siddharth Kumar, Sagar Sarkar, Akash Saha, Nandana Bhattacharya, John W. Freeland, Jong-Woo Kim, Philip J. Ryan, Priya Mahadevan, Srimanta Middey, *Communication Physics* **5**, 216 (2022). (*equal contribution)

2. **Direction-dependent conduction polarity in altermagnetic CrSb**
   Banik Rai*, Krishnendu Patra*, Satyabrata Bera, Sk Kalimuddin, Kakan Deb, Mintu Mondal, Priya Mahadevan, Nitesh Kumar, *et al.*, *Advanced Science* **2025**, 2502226. (*equal contribution)

3. **Origin of multiple Lifshitz transitions in the Weyl semi-metal RhSi**
   Krishnendu Patra, Viktor Christiansson, Ferdi Aryasetiawan, Priya Mahadevan, `arXiv:2403.19370v1`, 28 March 2024.

4. **Stability of the collinear ↑↑↓↓ magnetic ordering in partial cation-disordered Ising chain magnet Ca_3CoMnO_6**
   Pratap Pal, Krishnendu Patra *et al.*(submitted)

5. **Fe_xNbSe_2: Intercalant Assisted Tuning of Magnetic Properties in Layered Transition Metal Dichalcogenides**
   Subham Naik, Krishnendu Patra *et al.* (Manuscript under preparation)

.

Contents

List of Figures

List of Tables

Chapter 1

Introduction

Transition metal compounds are well known for their diverse physical properties primarily due to the strong coupling among their electronic, magnetic, and structural characteristics. These compounds form a distinctive class of solids with remarkably rich physics. Among them are excellent conductors, wide-gap insulators, and systems that exhibit metal-insulator transitions. Their magnetic properties are equally varied, with many strong magnets belonging to transition metals or rare-earth-based compounds. Transition metals serve an important role in the field of systems with strong electron correlations. Many ground breaking concepts,such as Mott insulators,were first proposed and developed in the context of these compounds. The magnetic behavior of transition metal compounds has been extensively investigated and applied over many years. However, their electronic behavior has recently gained more attention. Concepts like spintronics, magnetoelectricity,multiferroicity, and high-temperature superconductivity have created a rich and promising research field, with significant applications already emerging. Recently, topological properties have also been emerged based on transition metal compounds. Various members have been found to show different topological properties like topological insulator, Weyl semimetal etc. These materials can be identifed by examining the transport, such as anomalous Hall effect, planar Hall effect. Some of the materials display various ordered states, including magnetic, orbital, and charge order, driven by interactions such as exchange interactions, crystal field effects, and strong Coulomb repulsion. In this thesis, we have considered different transition metal compounds and examined their ground state behavior.

1.1 Electronic structure of Transition metal compounds

In transition metal compounds, we are often dealing with materials such as transition metal oxides or fluorides, which are typically insulating. Transitional metals could belong to 3d, 4d or 5d group of the periodic table. Those that contain 3d transition metal atoms are found to be more correlated with their behavior deviating from the standard prediction of the band theory. In these systems, it is essential to consider not only the correlated 3d electrons of the transition metals but also the valence s and p electrons of ligands such as oxygen or fluorine. These transition metal compounds exhibit complex

electronic interactions. Band theory generally predicts that materials possessing an even number of electrons per unit cell can be either metallic or insulating. In contrast, systems having an odd number of electrons per unit cell are expected to exhibit metallic behavior. However, this theoretical framework does not always hold. A notable exception is cobalt monoxide (CoO), which crystallizes in a rock salt structure consisting of one cobalt atom and one oxygen atom per unit cell. Cobalt, with an electron configuration of $3d^7 4s^2$, and oxygen, with $2s^2 2p^4$, together contribute a total of 15 electrons per unit cell, an odd number. Based on conventional band theory, CoO should behave as a metal, yet experimental studies have shown that it is an insulator [1,2]. This indicates the limitations of simple band theory in accurately describing the behavior of transition metal compounds. Standard band theory does not include electron-electron Coulomb interactions term(U) in a mean-field way [3]. To solve this discrepancy, both electron hopping and correlation effects were introduced to provide a more realistic description of the electronic structure in these systems. Using onsite Columb interaction as electron correlation gives the correct magnetic order. Although it gives the insulating picture, which is not an insulator in band theory, it often underestimates the band gap. The electronic properties of transition metal compounds, particularly those containing 3d elements, are predominantly governed by three key parameters:

- The on-site interaction energy U, which accounts for the Coulomb repulsion among 3d electrons.
- The charge-transfer energy Δ, defined as the energy required to transfer an electron from a ligand p orbital to a vacant metal d orbital.
- The metal-ligand hybridization strength t_{pd}, which controls the coupling between transition metal 3d and ligand 2p orbitals and affects the system's overall bandwidth W.

Considering mainly metal d orbitals and ligand p orbitals, due to their strong spatial overlap and hybridization, the energy levels of the ligand p orbitals typically lie below those of the transition-metal d orbitals. For example,in oxides, oxygen typically exists as O^{2-}, meaning its p orbitals are fully occupied. This configuration can be schematically represented as in Fig 1.1.

The d-orbitals of transition metals can either be empty or contain a specific number of electrons, typically described by a d^n configuration. Unlike the standard Hubbard model, where electrons localized at certain lattice sites can hop to other already occupied sites at an energy cost, U_{dd}. The process results in a change in the electronic configuration as:

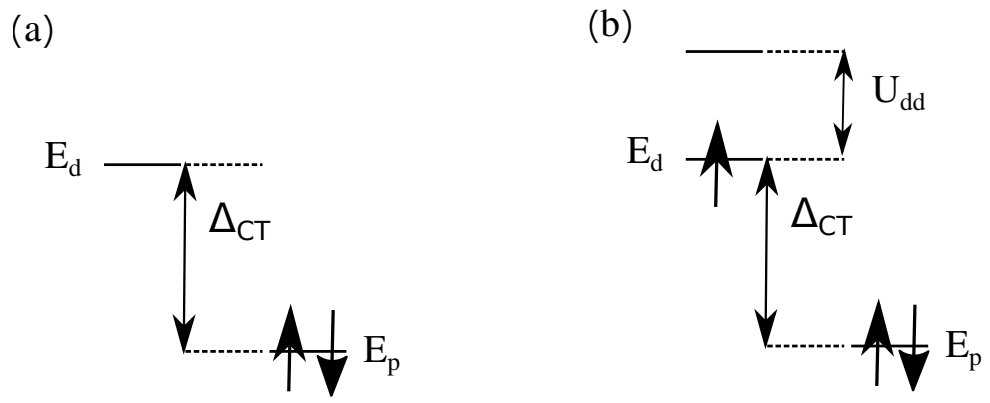

Figure 1.1: Energy level alignment of p and d orbitals in transition metal oxides, illustrating the charge-transfer gap: (a) for transition metal ions with a d^0 configuration, and (b) for ions with a d^1 electronic configuration.

$$\mathrm{d^n d^n} \longrightarrow \mathrm{d^{n-1} d^{n+1}}, \quad E_{(\mathrm{d^{n-1} d^{n+1}})} - E_{(\mathrm{d^{n-1} d^{n+1}})} = U = U_{dd} \tag{1.1}$$

When an electron transfers from one d^n site to another, it results in one site with a d^{n-1} configuration and another with a d^{n+1} configuration. The associated energy cost of this process is the on-site Coulomb repulsion, denoted by U_{dd} (U).

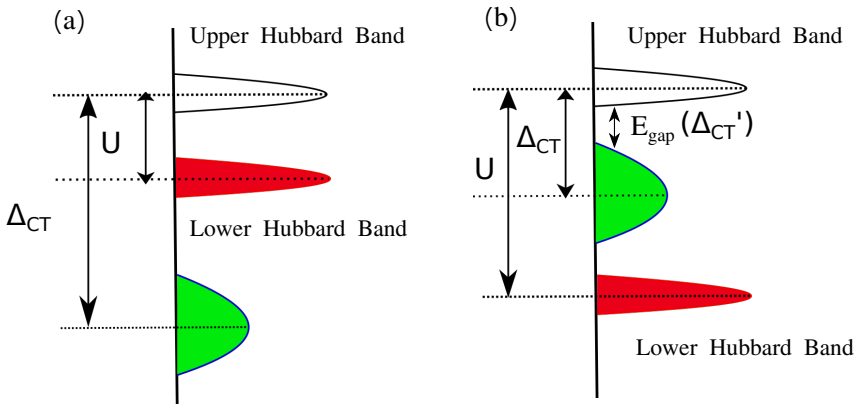

Figure 1.2: Schematic diagram of the density of states for (a) a Mott-Hubbard insulator when $U > \Delta_{\mathrm{CT}}$, and (b) a charge-transfer insulator when $U < \Delta_{\mathrm{CT}}$.

Another important type of excitation involves to move an electron from the fully occupied oxygen (ligand atom) $2p$ orbital to the transition metal ion. This process requires an energy Δ_{CT}, known as the charge-transfer energy.

$$\mathrm{d^n p^6} \longrightarrow \mathrm{d^{n+1} p^5}, \quad E_{(\mathrm{d^n p^6})} - E_{(\mathrm{d^{n+1} p^5})} = \Delta_{\mathrm{CT}} \tag{1.2}$$

Here, one additional d-electron is introduced to the transition metal ion, and a hole is simultaneously created in the oxygen p orbital due to the removal of an electron from the filled p^6 shell. Chemically, this corresponds to a transition of oxygen from its usual O^{2-} state to the ionic state O^-. The resulting configuration is typically written as $d^{n+1}L$, where L denotes a ligand hole. In the simplest scenario, where the transition metal ion has an empty d shell (i.e., d^0), the charge-transfer energy is:

$$\Delta_{\mathrm{CT}}(d^0) = \varepsilon_d - \varepsilon_p \tag{1.3}$$

However, if the transition metal ion already has one electron in its d orbital (i.e., d^1),the incoming electron experiences an additional Coulomb repulsion. Therefore, the charge-transfer energy becomes:

$$\Delta_{\mathrm{CT}}(d^1) = (\varepsilon_d + U_{dd}) - \varepsilon_p \tag{1.4}$$

This correction incorporates the electron correlation effects inherent in the transition metal d-electrons. When the on-site Coulomb repulsion U exceeds a critical value, a half-filled d-band splits into two sub-bands separated by an energy gap (see Fig 1.2). These bands are referred to a as the lower and upper Hubbard bands,representing the fully occupied and unoccupied states, respectively. This correlation-driven insulating phase is referred to as a Mott insulator. The corresponding insulating gap, known as the Mott-Hubbard gap, is approximately given by $\sim U - W_{\mathrm{eff}}$, where $W_{\mathrm{eff}} = zt$ is the effective d-bandwidth, with z being the coordination number and t the hopping amplitude. However, the nature of the lowest charge-carrying excitations depends on the relative magnitudes of the on-site Coulomb repulsion U_{dd} and the charge-transfer energy Δ_{CT}. If $\Delta_{\mathrm{CT}} > U_{dd}$, the lowest-energy excitations involve transitions of the type $d^n d^n \rightarrow d^{n+1} d^{n-1}$, which is found in Mott-Hubbard insulators. In this scenario, the oxygen p-orbitals can effectively be neglected, allowing a simplification from the full d-p model with an effective hopping parameter $t = t_{dd}$.On the other hand, if $\Delta_{\mathrm{CT}} < U_{dd}$, the lowest-energy charge excitations are no longer dominated by d-d transitions but instead by p-d transitions,involving electron transfer from the oxygen $2p$ orbitals to the transition metal d-states. In this case, electronic excitations correspond to added electrons in the d-orbitals, while hole excitations are located on the oxygen p-orbitals. Materials exhibiting this behavior are classified as charge-transfer insulators. In such cases, the gap scales with Δ' as shown in Fig 1.2 .

1.2 ZSA phase diagram

Zaanen, Sawatzky, and Allen proposed a phase diagram that categorizes the metallic and insulating behavior of strongly correlated electron systems based on the ratios U/t_{pd} and $\Delta_{\mathrm{CT}}/t_{pd}$. This phase diagram is illustrated in Fig 1.3. Here, Δ'_{CT} denotes the effective charge-transfer energy, defined as the energy difference between the oxygen p-band and the transition metal d-band. When the Coulomb repulsion U is smaller than Δ, the system

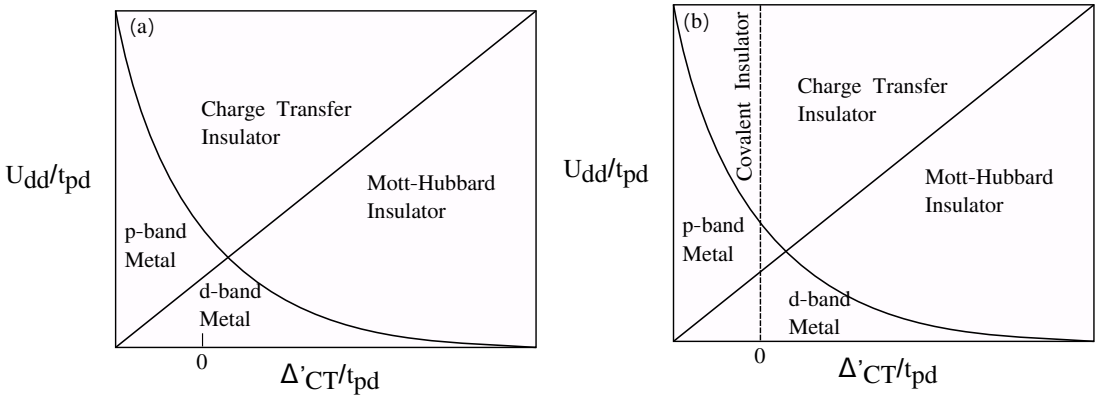

Figure 1.3: (a)ZSA phase diagram (b) Extended ZSA phase diagram showing the covalent insulator regime.

is in the Mott-Hubbard regime. If $U > W_{\mathrm{eff}}$,with $W_{\mathrm{eff}} = zt$ representing the effective d bandwidth,the material becomes a Mott-Hubbard insulator. Examples of such materials include $LaVO_3$, $LaTiO_3$, V_2O_3, and Ti_2O_3 [4]. On the other hand, if $U < W_{\mathrm{eff}}$, the lower and upper Hubbard bands overlap, leading to a metallic phase known as a d-band metal as for TiO and VO [4].

When $U > \Delta$, the system transitions into the charge-transfer regime. If the modified charge-transfer energy Δ' is greater than a critical value Δ_C and remains positive, the material behaves as a charge-transfer insulator, such as CuO [4]. However, when $\Delta' < \Delta_C$, the oxygen p-band overlaps with the upper Hubbard band, resulting in a p-type metallic state. Compounds such as CuS, NiSe, and $LaNiO_3$ are representative examples of this behavior [4].Further refinements of the model based on multiband Hubbard model calculations have shown that insulating behavior can also emerge for negative values of Δ, provided that U is sufficiently large. This insulating state originates from strong covalent interactions between transition metal d orbitals and ligand p orbitals and is referred to as a covalent insulator. This region appears in the extended ZSA phase diagram [Fig 1.3 b], positioned between the p-type metal and charge-transfer insulator domains. Without accounting for strong p–d hybridization, systems with negative Δ_{CT} would otherwise exhibit metallic conductivity.

1.3 Bond Disproportionated State

Although the covalent insulator phase is predicted by the extended ZSA phase diagram, its experimental realization is limited, as other interactions often dominate. The family of rare-earth nickelates $RENiO_3$ (RE = Pr, Nd, Sm, ..., Lu)(except La), which belong to the negative Δ_{CT} regime [5,6], exhibit temperature-driven metal-insulator transitions [7] as shown in Fig 1.4.

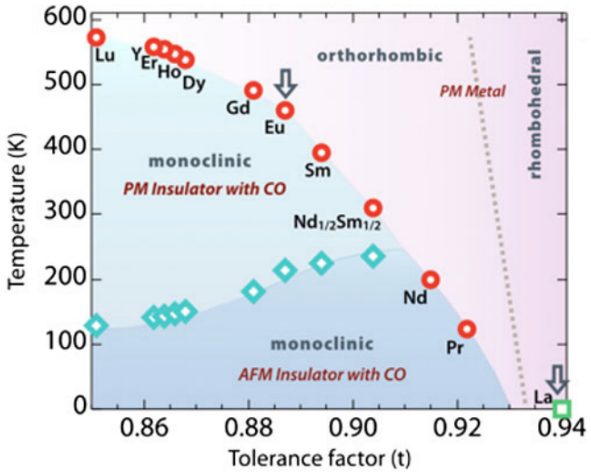

Figure 1.4: Temperature dependent Metal-insulator transition of Rare-earth nickelates. Adapted from [8].

Here, the insulating state is mainly accompanied by the formation of a bond disproportionated (BD) state. This state arises from a breathing-mode distortion in which alternating NiO_6 octahedra have different Ni–O bond lengths: shorter bonds(s) of approximately 1.90 Å and longer bonds(l) around 2.00 Å as shown schematically in Fig 1.5.

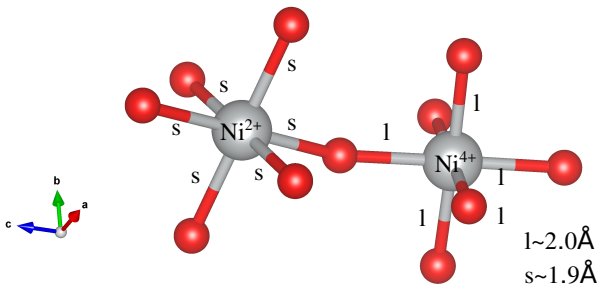

Figure 1.5: Two inequivalent NiO_6 octahedra.

Sometimes they are called charge-ordered states, but this is different from conventional charge ordering as there is no significant charge difference between the two Ni sites [9,10].

The difference arises from asymmetric hybridization with the oxygen p orbitals. In the short-bond sites, the Ni ions form singlet states ($S = 0$) due to strong antiferromagnetic coupling with ligand holes, resulting in a $3d^8L^2$ configuration. Conversely, the long-bond sites retain a more ionic $3d^8$ character. The Ni ions in the short-bond octahedra mimicked as Ni^{4+} show a negligible magnetic moment, whereas those in the long-bond octahedra mimicked as Ni^{2+} exhibit a moment of approximately 1.5 μ_B consistent with a high-spin Ni^{2+} ($3d^8$, S = 1) state. The electronic configuration for both Ni atoms is schematically shown in Fig 1.6.

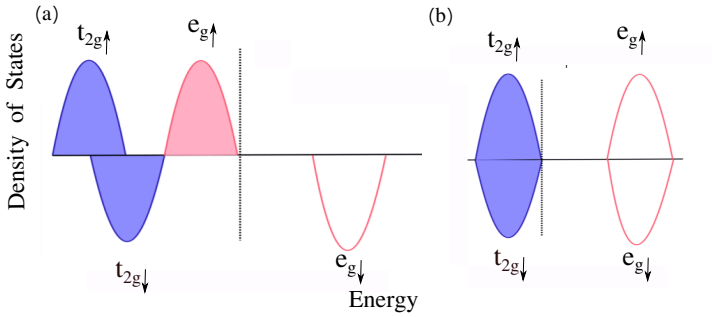

Figure 1.6: The schematic diagram of spin resolved density of states for (a)Ni^{2+} and (b)Ni^{4+} atoms.

Due to the octahedral crystal field effect,the Ni d orbitals split into t_{2g} and e_g orbitals. For Ni^{2+}, all the t_{2g} orbitals are occupied in the majority and minority spin channels, while for the e_g orbitals, only the majority spin channel is occupied. In contrast, for Ni^{4+}, both channels of the t_{2g} orbitals are occupied, whereas both spin channels of the e_g orbitals remain unoccupied.

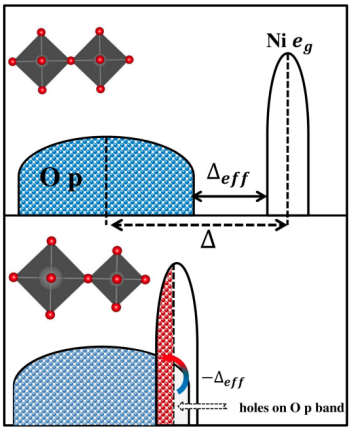

Figure 1.7: The schematic diagram showing the energy level of oxygen occupied p band Ni unoccupied e_g band. The onset of bond disproportionated state is presented when Ni-e_g band enters in O-p band defining Δ_{eff} [11].

This form of bond disproportionation is rare among undoped transition metal oxides that possess identical chemical formulas and oxidation states. It is believed to originate from the evolution of negative charge-transfer energy across the $3d$ transition metal series. When the hybridized Ni d band merges with the O p band, holes begin to populate the oxygen p-orbitals, leading to the onset of a bond-ordered insulating state [12].

1.4 Magnetic Ordering

The partial filling of the d-orbitals in transition metal compounds usually lead to the material exhibiting magnetic ordering. Different types of exchange interactions, between transition atoms are responsible for the preferred magnetic configuration. Magnetic ordering in solids arises from the specific alignment patterns of magnetic moments among neighboring atomic sites. The exchange interaction is key to the formation of long-range magnetic order. The Columb electrostatic interaction is

$$\hat{H}_U = \sum_{i<j} \frac{1}{|\mathrm{r}_i - \mathrm{r}_j|} \tag{1.5}$$

The Coulomb interaction term $\hat{H}_U$ is explicitly independent of spin. However, due to the antisymmetric nature of the many-electron wavefunction, the resulting eigenenergies exhibit spin dependence. This underlies the origin of atomic multiplet structures and forms the basis for Hund's first and second rules.

To elucidate the mechanism of Coulomb exchange, we consider a simple system comprising two electrons. Within the tight-binding approximation, we assume that the two-electron Hamiltonian $\hat{H}_0$ is solved by approximating the interaction term $\hat{H}_U$. Specifically, we examine a system with two orbitals, labeled $\alpha = a, b$. The corresponding two-electron Slater determinant, which includes spin states σ and σ', is expressed as:

$$\Psi_{a,\sigma;\,b,\sigma'}(\mathbf{r}_1, s_1 :\, \mathbf{r}_2, s_2) = \frac{1}{\sqrt{2}} \begin{vmatrix} \phi_a(\mathbf{r}_1)\,\sigma(s_1) & \phi_a(\mathbf{r}_2)\,\sigma(s_2) \\ \phi_b(\mathbf{r}_1)\,\sigma'(s_1) & \phi_b(\mathbf{r}_2)\,\sigma'(s_2) \end{vmatrix} \tag{1.6}$$

which simplifies to

$$\Psi_{a,\sigma:\,b,\sigma'}(\mathbf{r}_1, s_1;\, \mathbf{r}_2, s_2) = \frac{1}{\sqrt{2}} \left[\phi_a(\mathbf{r}_1)\phi_b(\mathbf{r}_2)\sigma(s_1)\sigma'(s_2) - \phi_b(\mathbf{r}_1)\phi_a(\mathbf{r}_2)\sigma'(s_1)\sigma(s_2)\right] \tag{1.7}$$

These Slater determinants represent degenerate eigenstates of the non-interacting Hamiltonian $\hat{H}_0$, all sharing the same eigenvalue $\varepsilon_a + \varepsilon_b$,irrespective of the spin orientations of the electrons. To understand how this degeneracy is lifted by electron-electron interactions,we evaluate the matrix elements of the Coulomb interaction term $\hat{H}_U$ in the basis formed by the two-electron Slater determinants $\Psi_{a,\sigma;\,b,\sigma'}$. When both electrons have identical spin states (i.e., $\sigma = \sigma'$), the spin part of the wavefunction can be factored out, and the two-electron Slater determinant simplifies to:

$$\Psi_{a,\sigma;\,b,\sigma}(\mathbf{r}_1, s_1;\, \mathbf{r}_2, s_2) = \frac{1}{\sqrt{2}} \left[\phi_a(\mathbf{r}_1)\phi_b(\mathbf{r}_2) - \phi_b(\mathbf{r}_1)\phi_a(\mathbf{r}_2)\right] \sigma(s_1)\sigma(s_2) \tag{1.8}$$

Next, we calculate the Coulomb interaction's expectation value for a spatial wave function that is antisymmetric, considering the case where both electrons share the same spin state.

$$\left\langle \Psi_{a,\sigma;\,b,\sigma} \left| \frac{1}{|\mathbf{r}_1 - \mathbf{r}_2|} \right| \Psi_{a,\sigma;\,b,\sigma} \right\rangle = \frac{1}{2} \left(U_{ab} - J_{ab} - J_{ba} + U_{ba}\right) \tag{1.9}$$

Since $U_{ab} = U_{ba}$ and $J_{ab} = J_{ba}$, this simplifies to:

$$= U_{ab} - J_{ab} \tag{1.10}$$

The direct terms correspond to the Coulomb integral, given by:

$$U_{ab} = \int d^3\mathrm{r}_1 \int d^3\mathrm{r}_2 \, \frac{|\phi_a(\mathrm{r}_1)|^2 \, |\phi_b(\mathrm{r}_2)|^2}{|\mathrm{r}_1 - \mathrm{r}_2|} \tag{1.11}$$

The cross terms correspond to the exchange integral, expressed as:

$$J_{ab} = \int d^3\mathrm{r}_1 \int d^3\mathrm{r}_2 \, \frac{\phi_a(\mathrm{r}_1)\, \phi_b(\mathrm{r}_1)\, \phi_b(\mathrm{r}_2)\, \phi_a(\mathrm{r}_2)}{|\mathrm{r}_1 - \mathrm{r}_2|} \tag{1.12}$$

For the states where the two electrons have opposite spins ($\sigma' = -\sigma$), the expectation value of the Coulomb interaction is given by:

$$\left\langle \Psi_{a,\sigma;\,b,-\sigma} \left| \frac{1}{|\mathrm{r}_1 - \mathrm{r}_2|} \right| \Psi_{a,\sigma;\,b,-\sigma} \right\rangle = U_{ab} \tag{1.13}$$

The diagonal matrix elements do not include any exchange contribution because the spin functions of the cross terms are orthogonal and therefore their overlap vanishes. However, there exist off-diagonal matrix elements such as

$$\left\langle \Psi_{a\uparrow;b\downarrow} \left| \frac{1}{|\mathrm{r}_1 - \mathrm{r}_2|} \right| \Psi_{a\downarrow;b\uparrow} \right\rangle = -J_{ab} \tag{1.14}$$

Since the interaction $\hat{H}_U$ preserves spin states, only these matrix elements are non-zero. Considering the basis states $\Psi_{\uparrow\uparrow}, \Psi_{\uparrow\downarrow}, \Psi_{\downarrow\uparrow}, \Psi_{\downarrow\downarrow}$, the Coulomb interaction operator can be expressed as the matrix:

$$\hat{H}_U = \begin{pmatrix} U_{ab} - J_{ab} & 0 & 0 & 0 \\ 0 & U_{ab} & -J_{ab} & 0 \\ 0 & -J_{ab} & U_{ab} & 0 \\ 0 & 0 & 0 & U_{ab} - J_{ab} \end{pmatrix} \tag{1.15}$$

The triplet states $\Psi_{\uparrow\uparrow}$ and $\Psi_{\downarrow\downarrow}$ are clearly eigenstates of $\hat{H}_U$ with the corresponding eigenenergy

$$\Delta\varepsilon_{\text{triplet}} = U_{ab} - J_{ab}. \tag{1.16}$$

By diagonalizing the 2×2 submatrix, we find the third triplet state

$$\frac{1}{\sqrt{2}} \left(\Psi_{\uparrow\downarrow} + \Psi_{\downarrow\uparrow} \right)$$

and the singlet state

$$\frac{1}{\sqrt{2}} \left(\Psi_{\uparrow\downarrow} - \Psi_{\downarrow\uparrow} \right) = \frac{1}{\sqrt{2}} \left[\phi_a(\mathbf{r}_1)\phi_b(\mathbf{r}_2) + \phi_b(\mathbf{r}_1)\phi_a(\mathbf{r}_2) \right] \frac{1}{\sqrt{2}} \left(|\downarrow\uparrow\rangle - |\uparrow\downarrow\rangle \right),$$

with the corresponding energy eigenvalue

$$\Delta\varepsilon_{\text{singlet}} = U_{ab} + J_{ab}. \tag{1.17}$$

The difference in energy between the singlet and triplet configurations is $2J_{ab}$, with the triplet states being lower in energy. If the orbitals ϕ_α are degenerate, the resulting energy ordering follows Hund's first rule, which states that the ground state within an atomic shell prefers the configuration with the highest possible total spin. In a simplified model involving two electrons, the exchange interaction,represented by the exchange integral J,originates from the energy difference between the triplet state (E_T) and the singlet state (E_S).

1.5 Kinetic Exchange

When the two electrons occupy different atoms, the formation of a chemical bond enables them to hop between these atoms, which lowers their energy by preserving kinetic energy. In situations where electron hopping dominates the exchange interaction, this mechanism is referred to as kinetic exchange. This interatomic exchange interaction is the primary driving mechanism behind different magnetic orders [13, 14]. The following sections present a detailed discussion of the primary exchange mechanisms.

1.5.1 Direct Exchange Interaction

Direct exchange refers to the interaction of electrons on magnetic atoms through an exchange interaction without involving any intermediary atoms. This mechanism relies on a significant overlap between the magnetic orbitals of the interacting atoms, making it a short-range coupling that rapidly diminishes with increasing distance between atoms. A simplified illustration of this concept is shown in Fig. 1.8. When two atoms are close, electrons tend to localize between them due to interatomic hopping. In accordance with the Pauli exclusion principle, the occupation of the same spatial region by two electrons necessitates opposite spin states, thereby inducing a negative exchange interaction and an associated energy cost arising from Coulomb repulsion U. However, the energy gained from hopping between neighboring sites dominates, thereby favoring antiparallel spin alignment in the direct exchange mechanism.

If the separation between atoms increases, the hopping energy t decreases due to reduced orbital overlap, and the condition $U_{dd} > t$ prevails. Under such circumstances, parallel spin alignment is preferred to minimize electron-electron repulsion, resulting in a positive exchange interaction. The sign of the direct exchange constant J is determined by the interplay between Coulomb repulsion and kinetic energy arising from electron hopping. In materials such as rare-earth elements, the $4f$ electrons are highly localized and strongly bound to the atomic core, resulting in a typically weak direct exchange interaction. Even in $3d$ transition metals like Ni, Co, and Fe where the orbitals are more extended than those of $4f$ electrons ,the influence of direct exchange on magnetic properties remains relatively minor. Consequently, an additional indirect exchange mechanism is often invoked to account for the dual localized and itinerant nature of the electrons.

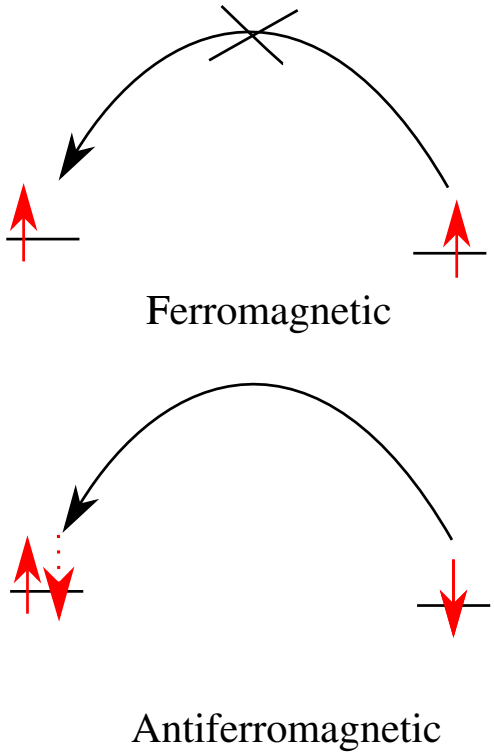

Figure 1.8: The schematic diagram of virtual hopping exchange between two atoms in ferromagnetic and antiferromagnetic configurations.

1.5.2 Indirect Exchange: Superexchange

The notion of kinetic exchange, initially introduced in [15], was further developed by Anderson [16, 17], who emphasized its importance in systems where magnetic ions are separated by large non-magnetic anions—conditions under which direct orbital overlap becomes negligible. To illustrate the mechanism of superexchange, a configuration in which two transition metal ions,each carrying a magnetic moment from a single unpaired d-electron,are separated by an oxygen atom that hosts two valence p-electrons (see Fig. 1.9). An antiferromagnetic alignment in the singlet configuration is favored, allowing two distinct hopping processes to occur. Through these processes, electron delocalization across the system is facilitated, leading to a reduction in total energy via kinetic energy gain. As discussed earlier, the antiferromagnetic exchange constant is defined as

$$J_{\mathrm{AFM}} = \frac{4t_{pd}^4}{(U_{dd} + \Delta_{pd})^2}\left(\frac{1}{U_{dd}} + \frac{1}{U_{dd} + \Delta_{pd}}\right) \tag{1.18}$$

Here, U_{dd} represents the Coulomb repulsion between d-electrons, t_{pd} denotes the hopping amplitude between d and p orbitals, and $\Delta_{pd} = \epsilon_d - \epsilon_p$ is the charge transfer energy. The first term in this expression represents hopping processes that involve a single doubly

occupied d-orbital, whereas the second term captures contributions from configurations with two doubly occupied d-orbitals

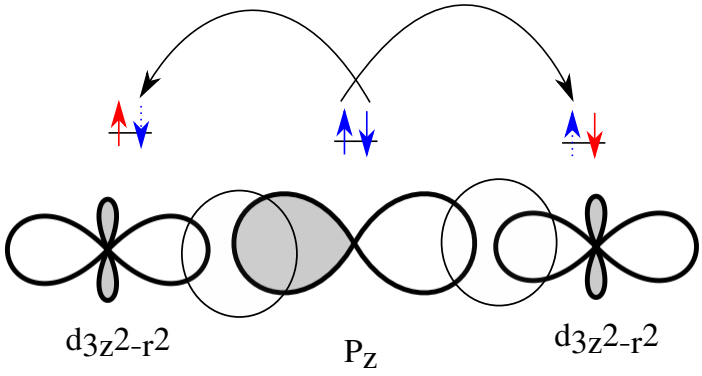

Figure 1.9: Superexchange interaction between two transition metal atoms via an oxygen atom, with a TM-O-TM bond angle of 180°, favors an antiferromagnetic configuration.

The superexchange interaction is highly sensitive to the angle formed by the cation-anion-cation bond. In Fig. 1.9, this angle is assumed to be 180°. If the angle is 90°, however, a different type of superexchange, often referred to as reverse superexchange, can occur, which may promote ferromagnetic alignment. This occurs when orbitals on the cations (e.g., $d_{3x^2-r^2}$ and $d_{3y^2-r^2}$) interact through distinct orbitals on the anion (e.g., p_x and p_y), as illustrated in Fig. 1.10. Because two different p orbitals are involved, the resulting hopping process is anisotropic and constrained by symmetry, allowing only unidirectional hopping. This results in a weak ferromagnetic interaction between the cations.

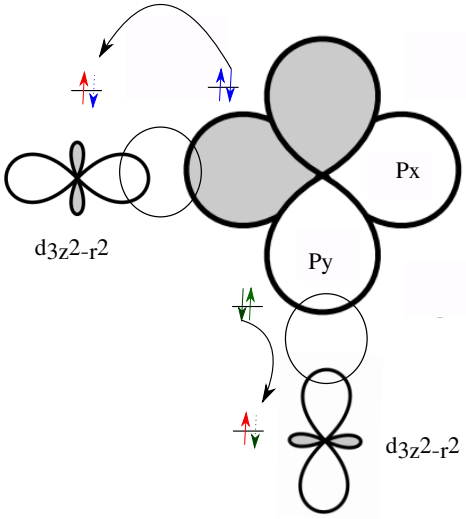

Figure 1.10: Superexchange interaction between two transition metal atoms via an oxygen atom, with a TM-O-TM bond angle of 90°, favors an ferromagnetic configuration.

The presence of two holes on the anion orbitals allows a triplet state to form on the oxygen, reducing the energy by $2J_p$. The ferromagnetic exchange constant in this case is expressed as:

$$J_{\mathrm{FM}} = \frac{4t_{pd}^4}{(U_{dd} + \Delta_{pd})^2} \left(\frac{2J_p}{4(U_{dd} + \Delta_{pd})^2 - J_p^2} \right) \tag{1.19}$$

This ferromagnetic interaction is significantly weaker than the antiferromagnetic counterpart. This scenario typically involves e_g orbitals. However, when t_{2g} orbitals are involved and oriented towards each other via the oxygen atom, direct d–d hopping becomes important and can support antiferromagnetic superexchange. This behavior is more common in compounds containing lighter transition metals. For heavier transition metals, d–p–d hopping tends to dominate . If both direct (d–d) and indirect (d–p–d) hopping channels are active, the total exchange interaction depends on the relative signs of the hopping parameters t_{dd} and t_{pd}. If both have the same sign, their effects reinforce, enhancing the exchange. If their signs are opposite, they partially cancel, leading to a reduction in the overall exchange strength.

In real crystals, structural distortions frequently alter the ideal bond angles, resulting in values different from 90° or 180°. This introduces a competition between ferromagnetic and antiferromagnetic superexchange mechanisms. These interactions are often interpreted using a set of semi-empirical rules known as the Goodenough-Kanamori-Anderson (GKA) rules [18–20]. In summary: when both cations have orbitals that are either half-filled or both empty, the superexchange interaction typically leads to antiferromagnetic coupling. Conversely, if one cation has a half-filled orbital while the other possesses an empty or fully occupied orbital, the interaction usually favors ferromagnetic alignment.

1.5.3 Itinerant Exchange

In metallic systems, exchange interactions arise through a different mechanism involving conduction electrons. This process, referred to as itinerant exchange or the Ruderman–Kittel–Kasuya–Yosida (RKKY) interaction, occurs when conduction electrons become spin-polarized in the presence of a localized magnetic moment. These spin-polarized electrons mediate an indirect interaction with the magnetic moment of a neighboring atom located at a distance r, resulting in a long-range exchange coupling. The RKKY interaction, named after Ruderman, Kittel, Kasuya, and Yosida [21–25], is characterized by a long-range and oscillatory nature. The exchange constant $J_{\mathrm{RKKY}}(r)$ is given by:

$$J_{\mathrm{RKKY}}(r) \propto \frac{\cos(2k_F r)}{r^3}, \tag{1.20}$$

where k_F is the Fermi wavevector, which defines the radius of the spherical Fermi surface. The oscillatory behavior of $J_{\mathrm{RKKY}}(r)$ as a function of r results in alternating ferromagnetic and antiferromagnetic interactions, depending on the separation between magnetic atoms.

1.5.4 Double Exchange

The emergence of ferromagnetic exchange interaction due to mixed valency [26] i.e., the presence of magnetic ions in more than one oxidation state, is referred to as double exchange. This mechanism involves the simultaneous contribution of both kinetic exchange and Coulomb exchange. In systems where the average number of electrons per cation is non-integral due to mixed valency, some sites possess more electrons than others. As a result, electrons can hop between these sites without incurring the on-site Coulomb repulsion energy U. A classic example is $LaMnO_3$, which contains Mn^{3+} ions and exhibits

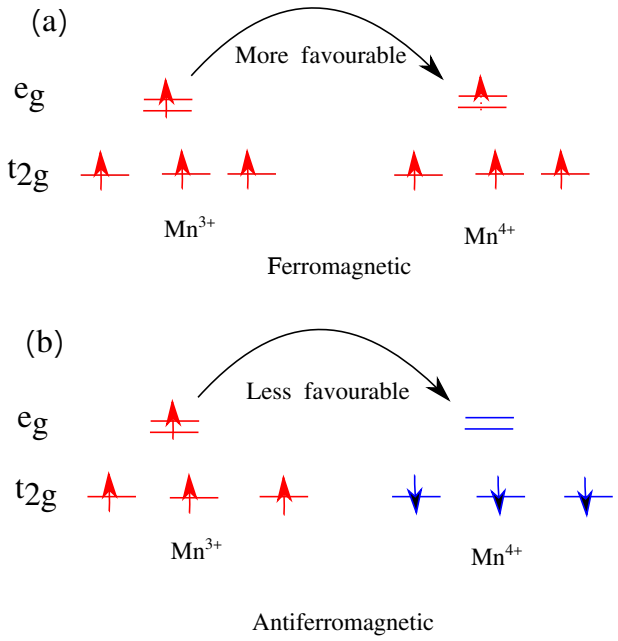

Figure 1.11: Schematic diagram of double exchange interaction pathways between two identical atoms(Mn) with different valencies: (a) favoring a ferromagnetic configuration, and (b) not favoring an antiferromagnetic configuration.

an A-type antiferromagnetic ground state. When approximately 17.5% of La is replaced by Sr, the material becomes ferromagnetic with a Curie temperature near room temperature, below which it also becomes metallic. In the compound $La_{1-x}Sr_xMnO_3$, the divalent nature of Sr^{2+}, compared to trivalent La^{3+}, and the -2 valency of oxygen imply that a

fraction x of the Mn ions become Mn^{4+}, while the remaining $1-x$ remain Mn^{3+}. The ferromagnetic ordering observed in this doped system [27, 28] is a direct consequence of the double exchange mechanism, which is illustrated in Fig. 1.11. In this context, an e_g electron from an Mn^{3+} ion can hop to a neighboring Mn site, provided the destination is an Mn^{4+} ion with an available e_g orbital of the same spin. Intra-atomic exchange interactions, particularly between the t_{2g} and e_g electrons, tend to align spins in the same direction in accordance with Hund's first rule, thereby lowering the total energy. Thus, a ferromagnetic alignment of neighboring ions becomes energetically favorablefor the maintenance of a high-spin configuration. This spin alignment facilitates electron hopping, which in turn reduces the system's kinetic energy and drives the transition to a metallic state. However, suppression of the double exchange mechanism can occur if the oxygen dumbbells adopt an orthogonal arrangement, hindering the overlap required for effective electron hopping [29].

1.6 Hubbard model

In condensed matter physics, one of the primary objectives is to solve the many-electron problem. If the Coulomb interaction among electrons were neglected, the Hamiltonian would reduce to a simpler form, essentially representing a single-electron system. The simplified Hamiltonian, without electron-electron interactions, is expressed as

$$H_0 = \sum_{n=1}^{N} h(r_n) = \sum_{n=1}^{N} \left(-\frac{1}{2}\nabla_n^2 + V_{\text{ext}}(r_n) \right), \tag{1.21}$$

and can be further rewritten as

$$H = H_0 + V, \tag{1.22}$$

here

$$V = \frac{1}{2}\sum_{i \neq j} v(r_i - r_j), \quad v(r_i - r_j) = \frac{1}{|r_i - r_j|}$$

where atomic units are adopted ($\hbar = e = m = 1$, implying 1 a.u. = 27.2 eV). The variable $r_n = (r_n, \sigma_n)$ is used to represent both the position and spin of the n-th electron, and the external potential V_{ext} is assumed to originate from sources such as nuclear charges. When the Coulomb interaction among electrons is introduced, the problem is significantly

complicated, and the Hamiltonian becomes that of a true many-body system. Exact solutions to the many-electron problem are generally feasible only for small systems, such as isolated atoms or simple molecules with a limited number of electrons. When excited states are of interest, as in this study, the complexity increases further. As a result, one must rely on a range of approximations and computational methods to achieve physically meaningful insights. When expressed in terms of field operators within the occupation number representation, the Hamiltonian takes the form [30]:

$$\hat{H} = \int d^3r\, \hat{\psi}^\dagger(r) \left[h_0(r) + \frac{1}{2}\hat{V}^H(r) \right] \hat{\psi}(r), \tag{1.23}$$

where the interaction term $\hat{V}^H(r)$ is given by

$$\hat{V}^H(r) = \int \mathrm{d}r'\, v(r-r')\, \hat{\psi}^\dagger(r')\hat{\psi}(r') = \int \mathrm{d}r'\, v(r-r')\, \hat{\rho}(r') \tag{1.24}$$

The conventional approach is followed for performing spatial integration, with $\int dr \equiv \int d^3r$. The field operator $\hat{\psi}(r)$ can be written in terms of single-particle basis functions $\varphi_n(r)$ as

$$\hat{\psi}(r) = \sum_{n,\sigma} \varphi_n(r)\, c_{n\sigma}, \tag{1.25}$$

where $c_{n\sigma}$ is the annihilation operator for the state labeled by n and spin σ. Substituting this expansion into the Hamiltonian yields:

$$\hat{H} = \sum_{i,j} c_i^\dagger \left(h_{ij}^0 + \frac{1}{2}\hat{V}_{ij}^H \right) c_j \tag{1.26}$$

where the two-body interaction contribution is defined as

$$\hat{V}_{ij}^H = \sum_{k,l} v_{ij,kl}\, c_k^\dagger c_l, \tag{1.27}$$

and the single-particle matrix elements are given by

$$h_{ij}^0 = \int d^3r\, \varphi_i^*(r)\, h_0(r)\, \varphi_j(r). \tag{1.28}$$

The two-electron Coulomb matrix element is defined as

$$v_{ij,kl} = \int d^3r \int d^3r' \, \varphi_i^*(r)\varphi_j(r) \, v(r-r') \, \varphi_k^*(r')\varphi_l(r'). \tag{1.29}$$

The set of one-particle orbitals $\{\varphi_n\}$ is, in principle, arbitrary; however, they are frequently chosen to be Kohn–Sham orbitals for practical purposes. It is important to note that the index n encompasses both the spatial component and the spin part of the wavefunction.

$$\varphi_n(r) = \varphi_k(r) \, \xi(\sigma), \quad n = (k, \xi). \tag{1.30}$$

A major simplification of the full many-electron Hamiltonian was proposed by Hubbard, leading to what is now known as the Hubbard model. He noted that much of the essential physics could be captured by focusing on electrons residing in the narrow, partially filled $3d$ bands that cross the Fermi level. To describe this scenario, a simplified, heuristic Hamiltonian was proposed, which later became widely known as the Hubbard model [31]:

$$\hat{H} = \sum_{i,j \in 3d} c_i^\dagger h_{ij}^0 c_j + \frac{1}{2} \sum_{i,j,k,l \in 3d} U_{ij,kl} \, c_i^\dagger c_k^\dagger c_l c_j, \tag{1.31}$$

The creation and annihilation operators are restricted to the localized $3d$ orbitals, and the full Coulomb interaction in Eq. (1.31) is replaced by an effective on-site interaction denoted as U. Here, the index i labels both the atomic site and the corresponding localized $3d$ orbital.

It was proposed that the more delocalized electrons, which lie outside the $3d$ subspace, mainly serve to screen the Coulomb repulsion among the $3d$ electrons. Consequently, the bare Coulomb interaction is effectively renormalized to the so-called Hubbard U. Moreover, this effective interaction is assumed to be predominantly local, implying that the indices i, j, k, and l in $U_{ij,kl}$ all correspond to the same atomic site.

1.7 Magnetism at different filling in Hubbard Model

By restricting the model to a single orbital per site, it simplifies to the one-band Hubbard model—the most basic representation capturing the essential physics of electron correlation.

$$H = -t \sum_{\langle ij \rangle, \sigma} c^{\dagger}_{i\sigma} c_{j\sigma} + U \sum_{i} n_{i\uparrow} n_{i\downarrow} + \text{H.c.} \tag{1.32}$$

where $n_{i\sigma} = c^{\dagger}_{i\sigma} c_{i\sigma}$ is the number operator with σ either up ($\uparrow$) or down ($\downarrow$).Neighboring atoms are connected through matrix elements t, which can be intuitively understood as the probability amplitude for an electron to hop between sites. In the absence of additional interactions, such hopping leads to the formation of an electronic band. Another important energy scale is the on-site Coulomb repulsion U, representing the energy cost of placing two electrons on the same atom. When U is comparable to or exceeds the bandwidth, electron motion becomes strongly correlated, and the independent-particle picture breaks down.

In the non-interacting or band limit, where $t \gg U$, the system is governed primarily by the hopping term, and the Hamiltonian becomes exactly solvable in momentum space. In this regime, the energy levels form a continuous band, leading to metallic behavior—except in cases where the band is completely filled, resulting in a band insulator.

In contrast, the opposite limit is known as the atomic limit, where the interaction term dominates, i.e., $U \gg t$. Under these conditions, the Coulomb repulsion governs the system's behavior. To minimize the interaction energy, electrons tend to localize and distribute themselves uniformly across the lattice sites, thereby suppressing charge fluctuations and inhibiting electronic motion.

In the atomic limit, the electrons are distributed as uniformly as possible. For a half-filled,non-degenerate system, this implies that each lattice site is occupied by exactly one electron. In this configuration, electronic hopping is strongly suppressed, as any hopping event would lead to double occupancy of a site and thereby incur an energy cost on the order of U. Consequently, under these conditions, a half-filled system becomes insulating.

Between the two limiting cases,the band limit and the atomic limit,there exists a critical interaction strength, denoted as U_c, at which the system transitions from a metallic to an insulating state. This transition is known as the Mott transition. It generally occurs when the interaction strength U becomes comparable to the bandwidth W of the non-interacting system.

In the strong coupling regime, where $U \gg t$, the Hubbard Hamiltonian can be approximated by a low-energy effective model referred to as the t-J model. This model operates within a projected Hilbert space where double occupancy is explicitly excluded, and it captures both the kinetic and magnetic interactions of the electrons. The corresponding Hamiltonian is given by [32]:

$$H_{t\text{-}J} = \mathcal{P}_S \left[T + H_H + T_0 \right] \mathcal{P}_S, \tag{1.33}$$

where doubly occupied states is removed by the projection operator $\mathcal{P}_S$.

The hopping term is

$$T = -t \sum_{\langle ij \rangle, \sigma} c^\dagger_{j\sigma} c_{i\sigma}, \tag{1.34}$$

and the second-order correction reads

$$T_0 = -\frac{t^2}{U} \sum_{\substack{\langle ij \rangle \langle jk \rangle \\ \sigma}} \left[c^\dagger_{k\sigma} (1 - n_{j\sigma}) c_{i\sigma} - c^\dagger_{k,-\sigma} c_{j\sigma} c_{j,-\sigma} c_{i\sigma} n_{j,-\sigma} \right], \quad i \neq k, \tag{1.35}$$

While the effective spin interaction term is given by

$$H_H = \frac{4t^2}{U} \sum_{\langle ij \rangle} \left(S_i \cdot S_j - \frac{1}{4} n_i n_j \right). \tag{1.36}$$

At half-filling ($n_i = 1$), the hopping terms T and T_0 are projected out by $\mathcal{P}_S$. the t-J model reduces to the spin-$\frac{1}{2}$ Heisenberg model.

$$H_H = J \sum_{\langle ij \rangle} S_i \cdot S_j + \text{const}, \tag{1.37}$$

with the exchange coupling

$$J = \frac{4t^2}{U}, \tag{1.38}$$

which emerges from the kinetic exchange mechanism via virtual hopping.

Considering the non-degenerate Hubbard model described by Equation (1.32) at exactly half-filling (i.e., one electron per site, $n = 1$) and in the regime where Coulomb repulsion dominates over hopping ($U \gg t$), the system behaves as a Mott insulator exhibiting an antiferromagnetic ground state, as discussed earlier. When the ratio U/t is reduced while maintaining $n = 1$, one might anticipate a phase transition from the insulating regime to metallic behavior (the Mott transition). However, in some materials featuring the special condition known as Fermi surface nesting [33], the metallic state becomes unstable. Instead, the system may develop a spin density wave (SDW) or charge density wave (CDW), which creates a gap at the Fermi level, thereby maintaining the insulating behavior even for relatively weak interactions.

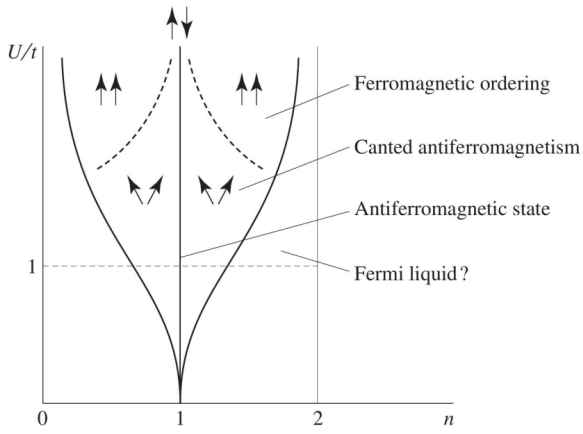

Figure 1.12: Phase diagram derived from the Hubbard model for varying electron fillings and a range of interaction strengths U/t [34].

For electron densities away from half-filling ($n \neq 1$), the situation becomes more intricate. Although strong Coulomb repulsion ($U/t \gg 1$) and antiferromagnetic correlations characteristic of the undoped system remain intact, the introduction of additional electrons or holes significantly complicates the system's dynamics. The antiferromagnetic background restricts the motion of these doped carriers because the spins on neighboring sites tend to be oppositely aligned, impeding hopping due to the Pauli exclusion principle. Consequently, the kinetic energy gain for the extra carriers is significantly reduced in this antiferromagnetic environment. Conversely, in a ferromagnetic background where spins are aligned, the doped electrons or holes can move more freely, resulting in a kinetic energy gain on the order of the bandwidth $W \sim zt$ (with z the coordination number). Although this ferromagnetic state costs exchange energy approximately $\sim \frac{t^2 V_f}{U}$ (where V_f denotes the volume fraction of the ferromagnetic region), it compensates through the kinetic energy gain $\sim t\delta$ from doping concentration δ. In the limit of infinite Coulomb repulsion ($U = \infty$), Nagaoka [35, 36] demonstrated that even a minimal doping destabilizes the antiferromagnetic state, driving the system into ferromagnetism. For large finite U values and finite doping levels ($\delta = 1 - n$), numerical studies reveal a complex phase diagram as illustrated in Fig 1.12. In strongly correlated systems, the doping region where the transition from antiferromagnetic (AFM) to ferromagnetic (FM) order occurs can host a variety of intermediate magnetic states, such as spin canting or spiral magnetic structures. The critical doping level δ_c for this AFM-FM transition approximately satisfies the relation

$$0.25\,\delta_c = \frac{t}{U}. \tag{1.39}$$

For the non-degenerate Hubbard model on bipartite lattices, electron-hole symmetry is preserved [37]. However, this symmetry may be broken if additional effects such as further-

neighbor hopping or orbital degeneracy are included. In such cases, the electronic behavior upon electron doping can differ substantially from that upon hole doping [37].

1.8 Altermagnetism

Altermagnetism is a newly identified form of collinear magnetic ordering, initially predicted theoretically and subsequently confirmed experimentally in MnTe [38, 39]. Similar magnetic characteristics have also been observed in RuO_2, [40, 41] although the precise magnetic nature of this material remains an active area of research. In conventional ferromagnets, the system exhibits a net magnetization arising from a strong nonrelativistic origin in real space. This leads to spin-polarized bands in momentum space that are typically isotropic (s-wave), as illustrated in Fig. 1.13 a. The energy bands split into majority and minority spin channels, thereby breaking time-reversal (T) symmetry [42]. The splitting of energy bands into majority and minority spin channels results in the breaking of time-reversal (T) symmetry [42]. In contrast, conventional antiferromagnets are characterized by a staggered magnetic order in real space with zero net magnetization. In the absence of spin-orbit coupling (SOC), their energy bands remain spin-degenerate and time-reversal symmetric, resembling nonmagnetic systems [Fig. 1.13 b] [42]. Altermagnets represent a distinct magnetic phase. They feature alternating magnetic moments in real space with no net magnetization, even in the absence of SOC. However, unlike antiferromagnets, they exhibit an alternating spin-polarization in momentum space, leading to spin-split bands that break T symmetry despite the absence of relativistic effects [Fig. 1.13 c]. These spin bands are equally populated, and the spin is a a good quantum number due to the common spin quantization axis preserved in this nonrelativistic regime [42]. The unique spin splitting in altermagnets originates from their symmetry properties: opposite-spin sublattices are related through real-space symmetries such as rotation or mirror reflection, rather than inversion or translation. Altermagnets can be categorized as planar or bulk, depending on symmetry and dimensionality. They exhibit characteristic d-, g-, or i-wave symmetries, corresponding to two, four, or six spin degenerate nodal planes at the Γ point,respectively [42]. The local atomic structure,particularly the spatial arrangement of nonmagnetic atoms around magnetic ions plays a crucial role in defining the spin-group symmetry. Unlike in typical antiferromagnets, where opposing spins are connected by inversion or translation, in altermagnets they are related by crystal rotational symmetries. This leads to the breaking of time-reversal (T), combined translation time-reversal (tT), and inversion time-reversal (PT) symmetries, thereby enabling momentum-dependent spin splitting even in the absence of SOC. A defining feature of

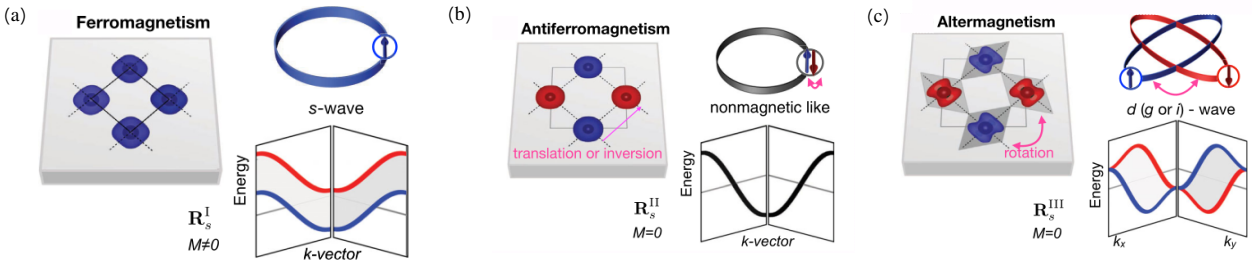

Figure 1.13: Illustration of collinear magnetic configurations—ferromagnetic, antiferromagnetic, and altermagnetic—in both real-space crystal structures and their corresponding momentum-space electronic band structures. (a) Ferromagnetism: A uniform spin sublattice induces finite magnetization and breaks time-reversal symmetry. This leads to momentum-independent spin splitting, resulting in isotropic s-wave spin-split Fermi surfaces. (b) Antiferromagnetism: Comprising two oppositely aligned spin sublattices (depicted in red and blue) related through translation or inversion symmetry, this configuration yields zero net magnetization and spin-degenerate electronic bands, similar to nonmagnetic materials. (c) Altermagnetism: Here, spin sublattices are related by rotational (but not translational or inversion) symmetry. Despite having no net magnetization, the system exhibits time-reversal symmetry breaking, with spin splitting that alternates in sign across momentum space, producing anisotropic sublattice spin textures and nontrivial d-, g-, or i-wave spin-split Fermi surfaces. Adapted from Ref. [42].

altermagnets is the lifting of Kramers degeneracy without requiring relativistic SOC or inversion symmetry breaking. The degeneracy is lifted through the nonrelativistic collinear magnetic order governed by the system's spin-group symmetry. This symmetry also ensures the preservation of a global spin-quantization axis, distinguishing altermagnetic spin splitting from that in SOC-driven systems. This underscores the fundamentally different nature of altermagnets compared to conventional ferromagnetic and antiferromagnetic materials [42].

1.9 Weyl semimetal

In 1937, Conyers Herring analyzed the conditions under which electronic states in crystalline solids can remain degenerate,having the same energy and crystal momentum,even in the absence of explicit symmetry protection [43]. These so-called accidental band crossings give rise to low-energy excitations that can be effectively described by the Weyl equation. In modern condensed matter physics, such crossings are known as Weyl points, and the associated quasiparticles are referred to as Weyl fermions [44, 45]. In these materials, the wavefunction of an electron accumulates a geometric phase, known as the Berry phase, when it completes a closed path in momentum space. This phase is analogous to

that acquired by an electron encircling a magnetic monopole in real space. Thus, Weyl points act as sources or sinks of Berry curvature in momentum space, functioning as momentum-space monopoles. Each Weyl node carries a chiral charge, which corresponds to the chirality of the Weyl fermion.

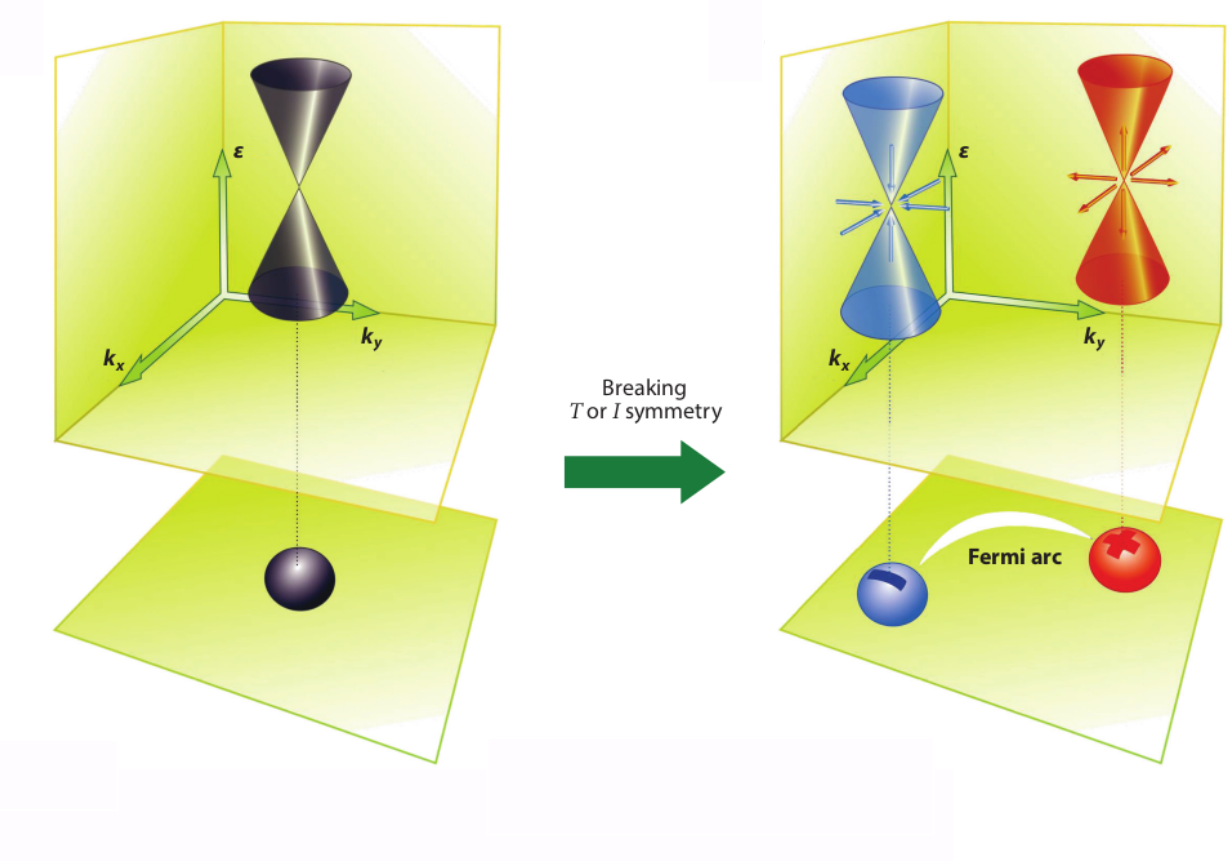

Figure 1.14: Weyl fermions can emerge in crystals when a Dirac point—formed by the intersection of two doubly degenerate bands—is present under both time-reversal and inversion symmetries. This Dirac point typically marks the boundary between trivial and topological insulating phases. If either time-reversal or inversion symmetry is broken, the Dirac point splits into two non-degenerate Weyl points with opposite chiralities. Each Weyl node acts as a source or sink of Berry curvature, carrying a quantized topological charge (Chern number). These topological features guarantee the existence of Fermi arc states on the surface, which connect the projections of Weyl nodes across the Brillouin zone. Adapted from Ref. [46].

This topological charge is protected by the crystal symmetry, making Weyl points robust against perturbations that preserve translational invariance. As a result, Weyl semimetals define a distinct class of topological phases that extend beyond topological insulators. In real space, Weyl fermions behave as chiral particles, while in reciprocal space, Weyl points appear as topological defects in the Berry curvature field. Weyl nodes typically emerge in systems that break either time-reversal or inversion symmetry. In such

systems, a transition from a topological insulator to a Weyl semimetal phase is possible. A key feature of Weyl semimetals is their unconventional surface-state structure, instead of closed Fermi surfaces as seen in topological insulators, they host open surface states known as Fermi arcs, [47, 48] which connect projections of Weyl nodes on the surface Brillouin zone.

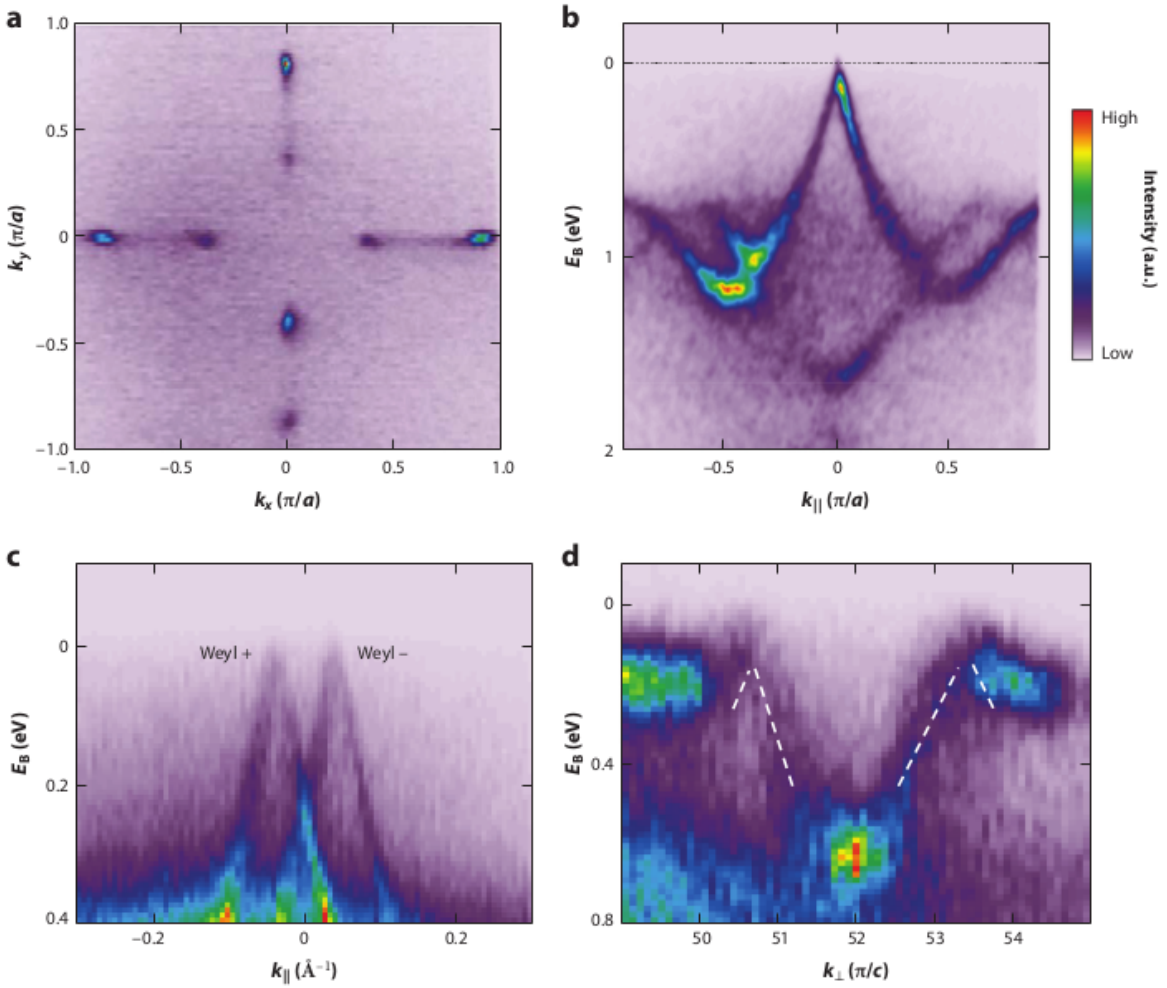

Figure 1.15: Experimental observation of topologically protected Weyl fermions in TaAs. (a) Bulk Fermi surface in the k_x–k_y plane, as revealed by angle-resolved photoemission spectroscopy (ARPES), showing discrete features attributed to Weyl nodes. (b) Energy–momentum dispersion along an in-plane cut intersecting a W1-type Weyl node, where a characteristic linear band crossing—indicative of a Weyl cone—is observed. (c) In-plane energy dispersion along a trajectory passing through a pair of W2-type Weyl nodes. (d) Out-of-plane dispersion along $k_\perp$, demonstrating band crossings at two W2 nodes located at the same k_x and k_y, but separated along k_z. Adapted from Reference. [46]

Theoretical studies have identified several materials, such as TaAs, as Weyl semimetal candidates [46]. These predictions have been confirmed using ab initio calculations and

angle-resolved photoemission spectroscopy (ARPES) [49]. ARPES enables direct probing of the electronic structure by measuring the energy and momentum of photoemitted electrons, providing access to both bulk Weyl points and surface Fermi arcs. Weyl semimetals also give rise to novel transport phenomena. These phenomena include the chiral anomaly, where parallel electric and magnetic fields result in the non-conservation of chiral charge, as well as the emergence of an anomalous Hall effect. Additionally, surface-state quantum oscillations and other exotic effects can emerge. When superconductivity is introduced, these materials may host quasiparticles that obey non-Abelian statistics, offering potential applications in spintronics and topological quantum computation. The stability of Weyl points is protected by a topological quantity known as the Chern number, which also plays a fundamental role in the integer quantum Hall (IQH) effect. The Chern number, denoted as χ, is expressed as:

$$\chi = \frac{1}{2\pi} \int dk_x dk_y \, \hat{z} \cdot \mathbf{\Omega}, \quad \mathbf{\Omega} = \nabla_{\mathbf{k}} \times \mathbf{A}, \quad \mathbf{A} = -i\langle \mathbf{k}, n | \nabla_{\mathbf{k}} | \mathbf{k}, n \rangle.$$

Here,Ω is the Berry curvature and A is the Berry connection. In two-dimensional systems, the integration is done over the full Brillouin zone, and the total Hall conductivity is obtained by summing over all filled bands.In contrast, for Weyl semimetals, which are three-dimensional systems, the Chern number is calculated over a closed two-dimensional surface within the Brillouin zone. When this surface is chosen to be a small sphere surrounding a Weyl point, the point contributes a quantized Chern number of $\chi = \pm 1$. This value, termed the chiral charge, represents the Berry flux through the surface, analogous to how Gauss's law describes electric flux from a point charge. Similar to electromagnetic theory, the chiral charge is quantized, and the Chern number associated with any closed surface depends solely on the net chiral charge contained within.

1.10 Lifshitz transition

About fifty years ago, Lifshitz proposed a type of electronic phase transition that arises due to changes in the topology of the Fermi surface, triggered by smooth lattice deformations in a system of noninteracting fermions. This transition, now referred to as the Lifshitz transition (LT), is distinct because it does not involve any symmetry breaking, unlike traditional Landau-type phase transitions [50]. It is generally viewed as a continuous transition that strictly occurs at absolute zero temperature ($T = 0$), while at higher temperatures, it transforms into a crossover. Lifshitz identified two fundamental types of Fermi surface topological changes, the neck-disrupting type, where a cylindri-

cal Fermi surface collapses, and the pocket-vanishing type, where a new Fermi surface pocket emerges. Numerous experimental studies have attempted to understand the Lif-

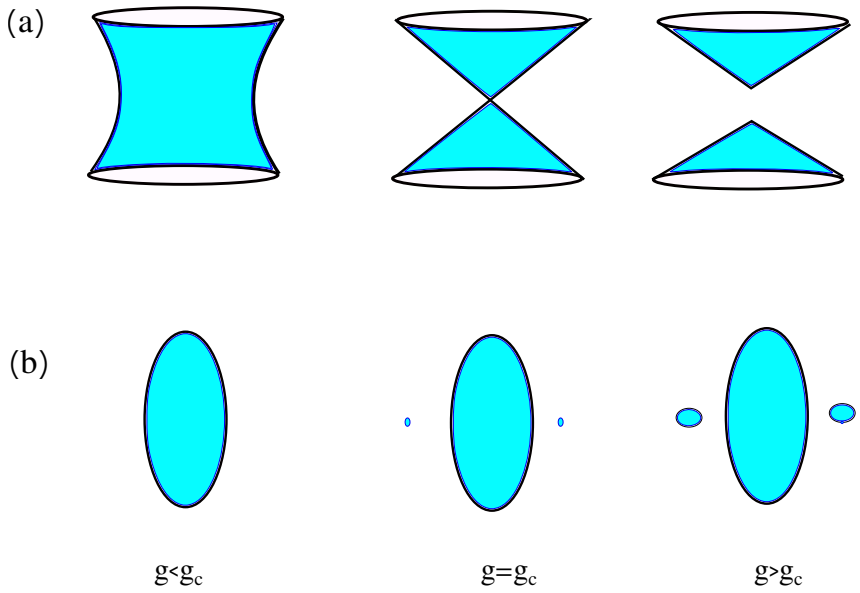

Figure 1.16: Schematic diagram of two different classes of Lifshitz transitions governed by the parameter g: (a) a cylindrical Fermi surface disrupted by neck-breaking, and (b) The appearance of two additional pockets near ellipsoidal Fermi pockets beyond the critical value of g.

shitz transition. In early work, anomalies in the superconducting transition temperatures of Tl and Re [51, 52] under pressure were interpreted as consequences of the Lifshitz transition. Subsequently, pressure-induced Lifshitz transitions have been suggested in various systems, including intermetallic compounds like $AuIn_2$ [53] and itinerant ferromagnets such as UGe_2 and $ZrZn_2$ [54, 55]. However, the Fermi surface topology's direct impact is often subtle and can be overshadowed by temperature effects and complex Fermi surface geometries. The transition tends to become more prominent when other degrees of freedom, such as spin or lattice, are strongly coupled with the electronic states. The essence of this transition lies in the relation between the density of electronic states $\frac{dN(E)}{dE}$ and the structure of constant-energy surfaces $E(\mathbf{p}) = E$ in momentum space. Critical energies $E = E_k$, at which the topology of these surfaces changes,such as when an open Fermi surface neck closes or a new disconnected pocket forms, lead to anomalies in the density of states. These critical surfaces contain singularities that alter the electron dynamics significantly. Although such critical points E_k are usually far from the chemical potential μ and are typically observed using x-ray spectroscopy, a continuously varying parameter that brings $\mu - E_k$ to zero can induce a topological change in the Fermi surface. Near this point, strong anomalies can emerge in the thermodynamic and transport properties of the electron system [56].

1.11 Seebeck Coefficient

Thermoelectric effects describe the interconversion between thermal and electrical energies in a material, where a temperature gradient can generate an electromotive force and, conversely, an electric current can produce a temperature difference. The strength of this effect is characterized by the Seebeck coefficient, denoted as α, which is defined as the ratio of the induced electric potential difference ϕ to the applied temperature gradient T across the thermoelectric material. This can be expressed as

$$\alpha = -\left(\frac{\phi}{T}\right), \tag{1.40}$$

In the limit where the temperature difference becomes infinitesimally small, the Seebeck coefficient is more precisely defined as the partial derivative of the electric potential with respect to temperature:

$$\alpha = -\left(\frac{\partial\phi}{\partial T}\right). \tag{1.41}$$

The Seebeck coefficient is a thermodynamic quantity that describes how the electric potential responds to a small temperature variation, under equilibrium conditions at constant pressure. According to the Cutler-Mott theory [57], the Seebeck coefficient α can be expressed as

$$\alpha = \frac{1}{qT} \cdot \frac{\int (\varepsilon - \mu)\, \sigma(\varepsilon)\, d\varepsilon}{\int \sigma(\varepsilon)\, d\varepsilon}, \tag{1.42}$$

where $q = \pm e$ denotes the carrier charge (with the negative sign corresponding to electrons and the positive sign to holes), μ is the Fermi level,ε is the electronic energy,and $\sigma(\varepsilon)$ represents the energy-dependent differential electrical conductivity. Within the framework of Boltzmann transport theory [58], the conductivity function $\sigma(\varepsilon)$ in Eq. (1.42) can be evaluated as

$$\sigma(\varepsilon) = e^2 \sum_{\mathbf{k}} f_{\mathbf{k}}(1 - f_{\mathbf{k}})\, \mathbf{v}_{\mathbf{k}} \cdot \mathbf{v}_{\mathbf{k}}\, \tau_{\mathbf{k}}, \tag{1.43}$$

where $f_{\mathbf{k}}$ is the Fermi-Dirac distribution, $\mathbf{v}_{\mathbf{k}}$ is the group velocity of carriers at wavevector $\mathbf{k}$, and $\tau_{\mathbf{k}}$ is the corresponding relaxation time. Here, $\mathbf{v}_{\mathbf{k}}$ denotes the group velocity of charge carriers associated with the crystal momentum $\mathbf{k}$. Within the framework of Boltzmann transport theory, in the low-temperature limit ($T \to 0$), the Seebeck coefficient is given by: [59]

$$\alpha = -\frac{\pi^2 k_B^2 T}{3e} \left[\frac{\partial \ln \bar{n}(\varepsilon, V)}{\partial \varepsilon}\bigg|_{\varepsilon=\varepsilon_F} + \frac{\partial \ln v^2(\varepsilon)}{\partial \varepsilon}\bigg|_{\varepsilon=\varepsilon_F} + \frac{\partial \ln \tau(\varepsilon)}{\partial \varepsilon}\bigg|_{\varepsilon=\varepsilon_F} \right], \tag{1.44}$$

where $\bar{n}(\varepsilon, V) = n(\varepsilon - \varepsilon_F, V)$ denotes the electronic density of states relative to the Fermi level ε_F,τ is the relaxation time, v is the average electron velocity, and which may depend on energy. In many first-principles calculations, the relaxation time τ is typically assumed to be constant. However, this is only one of several possible approximations in the zero-temperature regime. By accounting for screening effects in a free-electron gas and assuming a constant mean free path instead of constant τ, it has been shown that, in the $T \to 0$ limit, the Seebeck coefficient reduces to : [59]

$$\alpha = -\frac{\pi^2 k_B^2 T}{3e\varepsilon_F}. \tag{1.45}$$

using the parabolic band approximation [60], where $\bar{n}(\varepsilon) \propto \varepsilon^{1/2}$ and $v^2(\varepsilon) \propto \varepsilon$.

1.12 Direction dependent Conduction polarity

In most materials, electronic transport is uniform across different crystallographic directions, and a single type of charge carrier—either electrons (n-type) or holes (p-type),predominantly governs the transport properties. This behavior is generally observed in both metals and doped semiconductors.

However, some materials display direction-dependent conduction polarity, meaning they exhibit hole-type transport occurring along certain crystallographic directions and electron-type transport occurring along others. Such materials hold promise for advanced electronic and energy harvesting technologies, including transverse thermoelectric devices.In most cases, this direction-dependent conduction polarity can be understood from the material's electronic structure. It is directly related to the inverse effective mass, which reflects the curvature of the electronic band structure. This curvature serves as a useful indicator of whether a given band will predominantly exhibit n-type or p-type behavior. In particular, the curvature of the Fermi surface is directly associated with the reciprocal of the effective mass tensor $\left(\frac{1}{m^*_{ij}}\right)$, defined as: :

$$m^*_{ij} = \hbar^2 \left[\frac{\partial^2 E}{\partial k_i \partial k_j}\right]^{-1}_{E=E_{\mathrm{F}}}. \tag{1.46}$$

Experimentally, the conduction type (p-type or n-type) along different directions is often inferred from the sign of the Hall effect or thermopower measurements. Among these, thermopower is generally considered more reliable, as it is unaffected by the magnetic

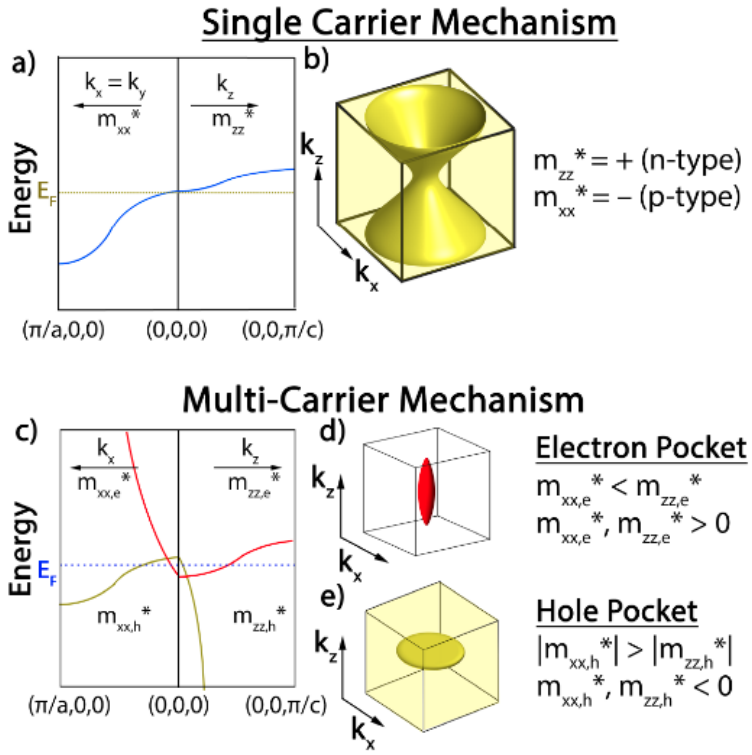

Figure 1.17: Electronic band structures and Fermi surface topologies for hypothetical tetragonal systems exhibiting crystallographic-direction-dependent conduction polarity. (a) Band structure and (b) hyperboloid-like Fermi surface for a case with single-band carrier transport. (c) Band structure, (d) Fermi surface of the conduction band, and (e) Fermi surface of the valence band for a scenario involving multiple carrier types. In (d), the electron pocket at the Fermi level (red, E_F) forms a prolate ellipsoid, indicative of higher mobility along the k_x and k_y directions. In contrast, panel (e) shows a hole pocket (yellow, E_F) shaped as an inverted oblate ellipsoid, suggesting increased mobility along the k_z axis. The yellow areas beyond the Fermi surfaces in (b) and (e) correspond to fully occupied electronic states. Adapted from [62].

field direction, unlike the Hall coefficient.The thermopower takes a positive value when conduction is dominated by holes (p-type), and a negative value when electrons (n-type) are the primary charge carriers. Being a second-rank tensor, thermopower (α_{ij}) can vary in sign and magnitude along different directions, especially in non-cubic crystals. The diagonal components α_{ii}, evaluated at the Fermi energy [61] E_{F}, are given by: [61, 62]

$$\alpha_{ii} = -\frac{\pi^2 k_B^2 T}{3|e|}\left[\frac{1}{n(E)}\frac{dn(E)}{dE} + \frac{1}{\tau_{ii}(E)}\frac{d\tau_{ii}}{dE} + m_{ii}^*\frac{d}{dE}\left(\frac{1}{m_{ii}^*}\right)\right]_{E=E_{\mathrm{F}}}, \tag{1.47}$$

where $n(E)$ is the density of states, T is the temperature,and k_B is Boltzmann's constant. For a crystal to exhibit differing signs of thermopower along various crystallographic axes, the integrated values of $1/m_{ij}^*$ over the Fermi surface, governing transport along

those directions, must have opposite signs. In other words, the net curvature of the band structure over the Fermi surface must differ across directions. Based on this understanding, two fundamental mechanisms can give rise to axis-dependent conduction polarity, categorized into two types of band structures: the single-carrier mechanism and the multicarrier mechanism. In the single-carrier mechanism, a single electronic band near the Fermi energy exhibits differing curvatures along orthogonal directions,concave (p-type) in one direction and convex (n-type) in another. For example, a band that curves upward along the k_z axis signifies a positive effective mass (m^*_{zz}) and hence n-type conduction in that direction. This type of band structure forms a saddle point and results in a Fermi surface with an open hyperboloid shape. Materials that display such direction-dependent carrier-type behavior are known as goniopolar materials. A well-studied example of this class is $NaSn_2As_2$ [61]. In contrast, the multicarrier mechanism involves different bands contributing to transport along different directions giving rise to p-type and another to n-type behavior. Each band dominates transport in a specific crystallographic direction. A typical example of such behavior is found in multicarrier semimetals, whose Fermi surfaces and band structures show separate valence and conduction bands contributing independently to transport along different directions. In these materials, the valence band may curve downward (negative curvature), signifying p-type conduction in some directions, while the conduction band exhibits opposite curvature in others [62].

1.13 Overview of the thesis

Our focus in this thesis is to investigate several unusual candidates among transition metal compounds using density functional theory (DFT) and tight-binding models to explore their ground state properties. In the introduction, we present the theoretical background relevant to various properties of transition metal compounds, which are directly applied in the different projects discussed in **Chapters 3 to 7**.

In **Chapter 2**, we describe the theoretical framework and methodological tools employed throughout this thesis.

In **Chapter 3**, we first focus on rare-earth nickelates ($RENiO_3$), which undergo a temperature-induced metal-insulator transition (MIT) that is accompanied by a structural transition involving bond disproportionation. This bond-disproportionated state consists of alternating expanded and contracted Ni–O octahedra, giving rise to two inequivalent Ni sites with different apparent valencies, though the formal valence remains unchanged. The bond-disproportionated state typically coexists within a specific range of negative charge transfer energy (Δ). While this state is known to exist in the undoped limit,

the insulating phase persists up to approximately 10% hole/electron doping. We choose $NdNiO_3$ as a prototypical system and examine whether the bond-disproportionated state survives under doping. Our results show that doped carriers tend to localize on specific sites, while the rest of the lattice retains the bond-disproportionated configuration. The variation in Δ, quantified through electrostatic potential changes, remains small further supporting the phase's stability. By analyzing the shift in the unoccupied $4p$ states of Ni,specifically at sites where electrons or holes are localized,we show that such localization can be experimentally detected using X-ray absorption spectroscopy (XAS).

In **Chapter 4**, we investigate the magnetic order in Ca_3CoMnO_6, part of the $Ca_3Co_{2-x}Mn_xO_6$ family. This compound exhibits a $\uparrow\uparrow\downarrow\downarrow$ magnetic ground state near $x = 1$, associated with multiferroicity induced by exchange striction. However, this magnetic order is not the true ground state at $x = 1$. Our systematic study reveals that this configuration can still be stabilized through moderate levels of cation (Co/Mn) positional disorder.

In **Chapter 5**, we study Fe-intercalated $2H$-$NbSe_2$, where $2H$-$NbSe_2$ is known for its superconductivity ($T_c \approx 7$ K) and charge-density wave. Upon Fe intercalation, magnetic order develops at the Fe sites. Using DFT+U calculations, we explore possible magnetic configurations and identify the antiferromagnetic ground state for 25% Fe-intercalated $NbSe_2$. We also derive a multiband Hubbard model by introducing a Hubbard U to a nonmagnetic tight-binding model, obtained by mapping the DFT band structure. This model helps us identify the exchange pathways responsible for the observed antiferromagnetic order.

In **Chapter 6**, we investigate the unusual transport properties of altermagnet CrSb,obtained by experimental observation, using DFT calculations. We explain the observation of direction-dependent conduction polarity (DDCP), where conduction is dominated by holes along the c-axis and by electrons in the ab-plane of the hexagonal crystal. Our calculations suggest that DDCP arises from a multicarrier mechanism, with electrons and holes in distinct bands dominating transport along different crystallographic directions.

In **Chapter 7**, we study RhSi, a transition metal compound that is a chiral topological semimetal hosting multifold Weyl points near the Fermi level. The low-energy states are dominated by Rh d orbitals. Using GGA+U calculations with $U_{\text{eff}} = 2.5$ eV, estimated via constrained random-phase approximation, we observe a double-hump feature in the electronic structure near the Fermi level. This arises from a competition between Rh d–Rh d and Rh d–Si p interactions. Artificially shifting the energy of the Si p orbitals reduces hybridization with Rh d states, eliminating the hump-like feature. The system

is highly sensitive to carrier concentration, and even slight doping significantly alters the Fermi surface topology transforming it from closed to open geometry with important implications for thermal transport properties.

Bibliography

[1] Patrik Fazekas. *Lecture notes on electron correlation and magnetism*, volume 5. World scientific, 1999.

[2] P. M. Sarte, M. Songvilay, E. Pachoud, R. A. Ewings, C. D. Frost, D. Prabhakaran, K. H. Hong, A. J. Browne, Z. Yamani, J. P. Attfield, E. E. Rodriguez, S. D. Wilson, and C. Stock. Spin-orbit excitons in CoO. *Phys. Rev. B*, 100:075143, Aug 2019.

[3] N. F. Mott. The basis of the electron theory of metals, with special reference to the transition metals. *Proceedings of the Physical Society. Section A*, 62(7):416, Jul 1949.

[4] Atsushi Fujimori, Yoshinori Tokura, DD Sarma, and SR Barman. Electronic structure of transition metal compounds. In *Spectroscopy of Mott Insulators and Correlated Metals: Proceedings of the 17th Taniguchi Symposium Kashikojima, Japan, October 24–28, 1994*, pages 126–138. Springer, 1995.

[5] S. R. Barman, A. Chainani, and D. D. Sarma. Covalency-driven unusual metal-insulator transition in nickelates. *Phys. Rev. B*, 49:8475–8478, Mar 1994.

[6] Valentina Bisogni, Sara Catalano, Robert J. Green, Marta Gibert, Raoul Scherwitzl, Yaobo Huang, Vladimir N. Strocov, Pavlo Zubko, Shadi Balandeh, Jean-Marc Triscone, George Sawatzky, and Thorsten Schmitt. Ground-state oxygen holes and the metal–insulator transition in the negative charge-transfer rare-earth nickelates. *Nature Communications*, 7(1):13017, Oct 2016.

[7] G. Catalan and. Progress in perovskite nickelate research. *Phase Transitions*, 81(7-8):729–749, 2008.

[8] S. Middey, D. Meyers, M. Kareev, Yanwei Cao, X. Liu, P. Shafer, J. W. Freeland, J.-W. Kim, P. J. Ryan, and J. Chakhalian. Disentangled cooperative orderings in artificial rare-earth nickelates. *Phys. Rev. Lett.*, 120:156801, Apr 2018.

[9] J. A. Alonso, J. L. García-Muñoz, M. T. Fernández-Díaz, M. A. G. Aranda, M. J. Martínez-Lope, and M. T. Casais. Charge disproportionation in $R\mathrm{nio}_3$ perovskites: Simultaneous metal-insulator and structural transition in ynio_3. *Phys. Rev. Lett.*, 82:3871–3874, May 1999.

[10] J. A. Alonso, M. J. Martínez-Lope, M. T. Casais, J. L. García-Muñoz, and M. T. Fernández-Díaz. Room-temperature monoclinic distortion due to charge disproportionation in RNiO$_3$ perovskites with small rare-earth cations (r = Ho, y, er, tm, yb, and lu): A neutron diffraction study. *Phys. Rev. B*, 61:1756–1763, Jan 2000.

[11] Sagar Sarkar. Role of structure in determining the properties of transition metal / post transition metal compounds. *Thesis*, 2018.

[12] Basudeb Mandal, Sagar Sarkar, Shishir Kumar Pandey, Priya Mahadevan, Cesare Franchini, A. J. Millis, and D. D. Sarma. The driving force for charge ordering in rare earth nickelates, 2017.

[13] Seymour H Vosko, Leslie Wilk, and Marwan Nusair. Accurate spin-dependent electron liquid correlation energies for local spin density calculations: a critical analysis. *Canadian Journal of physics*, 58(8):1200–1211, 1980.

[14] J. P. Perdew and Alex Zunger. Self-interaction correction to density-functional approximations for many-electron systems. *Phys. Rev. B*, 23:5048–5079, May 1981.

[15] John P. Perdew and Yue Wang. Accurate and simple analytic representation of the electron-gas correlation energy. *Phys. Rev. B*, 45:13244–13249, Jun 1992.

[16] Chengteh Lee, Weitao Yang, and Robert G. Parr. Development of the colle-salvetti correlation-energy formula into a functional of the electron density. *Phys. Rev. B*, 37:785–789, Jan 1988.

[17] Axel D. Becke. Density-functional thermochemistry. i. the effect of the exchange-only gradient correction. *The Journal of Chemical Physics*, 96(3):2155–2160, Feb 1992.

[18] P. Hohenberg and W. Kohn. Inhomogeneous electron gas. *Phys. Rev.*, 136:B864–B871, Nov 1964.

[19] John P. Perdew, Kieron Burke, and Matthias Ernzerhof. Generalized gradient approximation made simple. *Phys. Rev. Lett.*, 77:3865–3868, Oct 1996.

[20] Axel D. Becke. A new mixing of hartree–fock and local density-functional theories. *The Journal of Chemical Physics*, 98(2):1372–1377, 01 1993.

[21] C. Franchini, V. Bayer, R. Podloucky, J. Paier, and G. Kresse. Density functional theory study of mno by a hybrid functional approach. *Phys. Rev. B*, 72:045132, Jul 2005.

[22] C. Franchini, R. Podloucky, J. Paier, M. Marsman, and G. Kresse. Ground-state properties of multivalent manganese oxides: Density functional and hybrid density functional calculations. *Phys. Rev. B*, 75:195128, May 2007.

[23] Jochen Heyd, Gustavo E. Scuseria, and Matthias Ernzerhof. Hybrid functionals based on a screened coulomb potential. *The Journal of Chemical Physics*, 118(18):8207–8215, 05 2003.

[24] N. W. Ashcroft and N. D. Mermin. Solid state physics. *Brooks/Cole Thomson Learning Inc.*, 1976.

[25] C. Kitte. Introduction to solid state physics. *JohnWiley and Sons, Inc., seventh edition,*, 1996.

[26] D. Marx J. Grotendorst, S. Bl¨ugel. Computational nanoscience: Do it yourself ! *John von Neumann Institute for Computing, J¨ulich,NIC Series, Vol. 31, ISBN 3-00-017350-1, pp. 85-129*, 2006.

[27] O. Kaoru and Y. K. Esfarjani. Computational materials science. *Springer, p. 52*, (1999).

[28] L. Vitos. Computational quantum mechanics for materials engineers: The emto method and applications,. *Springer-Verlag, p. 7*, (2007).

[29] Conyers Herring. A new method for calculating wave functions in crystals. *Phys. Rev.*, 57:1169–1177, Jun 1940.

[30] A.L. Fetter and J.D. Walecka. Quantum theory of many-particle systems. *(Dover, New York)*, (1927).

[31] J. Hubbard and Brian Hilton Flowers. Electron correlations in narrow energy bands. *Proceedings of the Royal Society of London. Series A. Mathematical and Physical Sciences*, 276(1365):238–257, 1963.

[32] Erik Koch. lecture on exchange mechanisms.

[33] Daniel I Khomskii. *Basic aspects of the quantum theory of solids: order and elementary excitations*. Cambridge university press, 2010.

[34] Daniel I Khomskii. *Transition metal compounds*. Cambridge University Press, 2014.

[35] Yosuke Nagaoka. Ferromagnetism in a narrow, almost half-filled s band. *Phys. Rev.*, 147:392–405, Jul 1966.

[36] Yosuke Nagaoka. Ground state of correlated electrons in a narrow almost half-filled s band. *Solid State Communications*, 3(12):409–412, 1965.

[37] D. I. Khomskii. Phys. of metal and metallography 29, 31. *Sov. Phys*, 1970.

[38] T. Osumi, S. Souma, T. Aoyama, K. Yamauchi, A. Honma, K. Nakayama, T. Takahashi, K. Ohgushi, and T. Sato. Observation of a giant band splitting in altermagnetic mnte. *Phys. Rev. B*, 109:115102, Mar 2024.

[39] A. Hariki, A. Dal Din, O. J. Amin, T. Yamaguchi, A. Badura, D. Kriegner, K. W. Edmonds, R. P. Campion, P. Wadley, D. Backes, L. S. I. Veiga, S. S. Dhesi, G. Springholz, L. Šmejkal, K. Výborný, T. Jungwirth, and J. Kuneš. X-ray magnetic circular dichroism in altermagnetic α-mnte. *Phys. Rev. Lett.*, 132:176701, Apr 2024.

[40] Zexin Feng, Xiaorong Zhou, Libor Šmejkal, Lei Wu, Zengwei Zhu, Huixin Guo, Rafael González-Hernández, Xiaoning Wang, Han Yan, Peixin Qin, Xin Zhang, Haojiang Wu, Hongyu Chen, Ziang Meng, Li Liu, Zhengcai Xia, Jairo Sinova, Tomáš Jungwirth, and Zhiqi Liu. An anomalous hall effect in altermagnetic ruthenium dioxide. *Nature Electronics*, 5(11):735–743, Nov 2022.

[41] Arnab Bose, Nathaniel J. Schreiber, Rakshit Jain, Ding-Fu Shao, Hari P. Nair, Jiaxin Sun, Xiyue S. Zhang, David A. Muller, Evgeny Y. Tsymbal, Darrell G. Schlom, and Daniel C. Ralph. Tilted spin current generated by the collinear antiferromagnet ruthenium dioxide. *Nature Electronics*, 5(5):267–274, May 2022.

[42] Libor Šmejkal, Jairo Sinova, and Tomas Jungwirth. Beyond conventional ferromagnetism and antiferromagnetism: A phase with nonrelativistic spin and crystal rotation symmetry. *Phys. Rev. X*, 12:031042, Sep 2022.

[43] Conyers Herring. Accidental degeneracy in the energy bands of crystals. *Phys. Rev.*, 52:365–373, Aug 1937.

[44] Shuichi Murakami. Phase transition between the quantum spin hall and insulator phases in 3d: emergence of a topological gapless phase. *New J. Phys. 9 356*, 2007.

[45] A. A. Burkov and Leon Balents. Weyl semimetal in a Topological Insulator Multilayer. *Phys. Rev. Lett.*, 107:127205, Sep 2011.

[46] Su-Yang Xu, Ilya Belopolski, Nasser Alidoust, Madhab Neupane, Guang Bian, Chenglong Zhang, Raman Sankar, Guoqing Chang, Zhujun Yuan, Chi-Cheng Lee, Shin-Ming Huang, Hao Zheng, Jie Ma, Daniel S. Sanchez, BaoKai Wang, Arun Bansil, Fangcheng Chou, Pavel P. Shibayev, Hsin Lin, Shuang Jia, and M. Zahid

Hasan. Discovery of a weyl fermion semimetal and topological fermi arcs. *Science*, 349(6248):613–617, 2015.

[47] Xiangang Wan, Ari M. Turner, Ashvin Vishwanath, and Sergey Y. Savrasov. Topological semimetal and fermi-arc surface states in the electronic structure of pyrochlore iridates. *Phys. Rev. B*, 83:205101, May 2011.

[48] Ashvin Vishwanath. Where the weyl things are. *Physics 8, 84*, 2015.

[49] Shin-Ming Huang, Su-Yang Xu, Ilya Belopolski, Chi-Cheng Lee, Guoqing Chang, BaoKai Wang, Nasser Alidoust, Guang Bian, Madhab Neupane, Chenglong Zhang, Shuang Jia, Arun Bansil, Hsin Lin, and M. Zahid Hasan. A Weyl Fermion semimetal with surface Fermi arcs in the transition metal monopnictide TaAs class. *Nature Communications*, 6(1):7373, Jun 2015.

[50] Yoshihiko Okamoto, Atsushi Nishio, and Zenji Hiroi. Discontinuous lifshitz transition achieved by band-filling control in na_xcoo_2. *Phys. Rev. B*, 81:121102, Mar 2010.

[51] VI Makarov and VG Bar'Yakhtar. Anomalies in the superconducting transition temperature under pressure. *Sov. Phys. JETP*, 21:1151, 1965.

[52] C. W. Chu, T. F. Smith, and W. E. Gardner. Study of fermi-surface topology changes in rhenium and dilute re solid solutions from T_c measurements at high pressure. *Phys. Rev. B*, 1:214–221, Jan 1970.

[53] B. K. Godwal, A. Jayaraman, S. Meenakshi, R. S. Rao, S. K. Sikka, and V. Vijayakumar. Electronic topological and structural transition in $AuIn_2$ under pressure. *Phys. Rev. B*, 57:773–776, Jan 1998.

[54] K. G. Sandeman, G. G. Lonzarich, and A. J. Schofield. Ferromagnetic superconductivity driven by changing fermi surface topology. *Phys. Rev. Lett.*, 90:167005, Apr 2003.

[55] Youhei Yamaji, Takahiro Misawa, and Masatoshi Imada. Quantum metamagnetic transitions induced by changes in fermi-surface topology: Applications to a weak itinerant-electron ferromagnet zrzn2. *journal of the physical society of japan*, 76(6):063702, 2007.

[56] IM Lifshitz et al. Anomalies of electron characteristics of a metal in the high pressure region. *Sov. Phys. JETP*, 11(5):1130–1135, 1960.

[57] Melvin Cutler and N. F. Mott. Observation of anderson localization in an electron gas. *Phys. Rev.*, 181:1336–1340, May 1969.

[58] T. J. Scheidemantel, C. Ambrosch-Draxl, T. Thonhauser, J. V. Badding, and J. O. Sofo. Transport coefficients from first-principles calculations. *Phys. Rev. B*, 68:125210, Sep 2003.

[59] Yi Wang, Yong-Jie Hu, Brandon Bocklund, Shun-Li Shang, Bi-Cheng Zhou, Zi-Kui Liu, and Long-Qing Chen. First-principles thermodynamic theory of seebeck coefficients. *Phys. Rev. B*, 98:224101, Dec 2018.

[60] U. Sivan and Y. Imry. Multichannel landauer formula for thermoelectric transport with application to thermopower near the mobility edge. *Phys. Rev. B*, 33:551–558, Jan 1986.

[61] Bin He, Yaxian Wang, Maxx Q. Arguilla, Nicholas D. Cultrara, Michael R. Scudder, Joshua E. Goldberger, Wolfgang Windl, and Joseph P. Heremans. The fermi surface geometrical origin of axis-dependent conduction polarity in layered materials. *Nature Materials*, 18(6):568–572, Jun 2019.

[62] Yaxian Wang, Karl G. Koster, Andrew M. Ochs, Michael R. Scudder, Joseph P. Heremans, Wolfgang Windl, and Joshua E. Goldberger. The chemical design principles for axis-dependent conduction polarity. *Journal of the American Chemical Society*, 142(6):2812–2822, Feb 2020.

Chapter 2

Theoretical Framework

The atom, is the basic building block that we need to consider to understand the various properties in materials. Atomic interactions within a solid govern the resulting electronic structure of the material. The Hamiltonian involved is given by using Time-invariant and the non-relativistic Schrödinger equation: $H\psi = E\psi$, where H represents the many-body Hamiltonian, ψ denotes the set of energy eigenstates, and E corresponds to the set of energy eigenvalues.

$$\hat{H} = -\sum_{A} \frac{\hbar^2}{2M_A}\nabla_A^2 - \sum_{k} \frac{\hbar^2}{2m_e}\nabla_k^2 + \frac{1}{2}\sum_{A\neq B} \frac{Z_A Z_B e^2}{|\mathbf{R}_A - \mathbf{R}_B|} + \frac{1}{2}\sum_{k\neq l} \frac{e^2}{|\mathbf{r}_k - \mathbf{r}_l|} - \sum_{A,k} \frac{Z_A e^2}{|\mathbf{R}_A - \mathbf{r}_k|} \tag{2.1}$$

In the given Hamiltonian, M_A and R_A represent the mass and position of the A-th nucleus, while r_k denotes the position of the k-th electron. The quantities e and m_e correspond to the elementary charge and electron mass, respectively. The nuclear charge is written as $Z_A e$, where Z_A is the atomic number of nucleus A. The operators ∇_A^2 and ∇_k^2 are Laplacians with respect to the nuclear and electronic coordinates, indicating second-order spatial derivatives. The constant $\hbar$ represents the reduced Planck constant.

The Hamiltonian consists of the following contributions:

- Kinetic energy of the nuclei,
- Kinetic energy of the electrons,
- Coulomb repulsion between nuclei,
- Coulomb repulsion between electrons,
- Attractive Coulomb interaction between electrons and nuclei.

Altogether, the full many-body Hamiltonian is compactly written as:

$$\hat{H} = \hat{T}_{\text{nuc}} + \hat{T}_{\text{el}} + \hat{V}_{\text{nuc-nuc}} + \hat{V}_{\text{el-el}} + \hat{V}_{\text{el-nuc}}.$$

The material properties can be determined by solving the many-body Schrödinger equation. However, solving this equation fully in a quantum-mechanical framework is challenging due to the complexity of coupled coordinates. Complete analytical solutions

are rare, and numerical solutions are limited to small systems. To address this, two main approaches are used:
a) Applying reasonable approximations, such as the Born-Oppenheimer approximation and the independent electron approximation, which decouple the many-body wave function. Methods such as Hartree, Hartree-Fock, and Density Functional Theory (DFT) are employed to solve the equation within computational limitations.
b) Replacing the electronic component of the many-body Hamiltonian with a model Hamiltonian that focuses on dominant interactions and key single-particle orbitals. This includes models such as the Tight Binding Model, Hubbard Model, and Configuration Interaction (CI) methods, which are solved using numerical techniques like exact diagonalization (ED).

In the next sections, we will discuss the Born-Oppenheimer approximation and the various methods employed in this thesis for the solution of the many-body Schrödinger equation.

2.1 Born-Oppenheimer Approximation

The Born–Oppenheimer approximation, proposed by Max Born and J. Robert Oppenheimer, is based on the large mass difference between nuclei and electrons. Since nuclei are approximately 1800 times heavier, they move much more slowly than electrons. This justifies treating nuclei as stationary with respect to electronic motion, enabling the decoupling of nuclear and electronic degrees of freedom. So the full many-body Hamiltonian can be rewritten as: :

$$H = H_{\text{nuclear}} + H_{\text{electronic}} = \left[\hat{T}_{\text{nuc}} + \hat{V}_{\text{nuc-nuc}}\right] + \left[\hat{T}_{\text{el}} + \hat{V}_{\text{el-el}} + \hat{V}_{\text{el-nuc}}\right] \tag{2.2}$$

Within the scope of this adiabatic approximation, the kinetic energy term of the nuclei is ignored as the nuclei are considered to be nearly stationary compared to the electron motion. Additionally, the potential energy due to nuclear-nuclear interactions is treated as a constant, known as the Madelung energy , which can be computed classically. Consequently, the Hamiltonian simplifies to the electronic part alone:

$$H_{\text{ele}}^{\text{BOA}} = \hat{T}_{\text{el}} + \hat{V}_{\text{el-el}} + \hat{V}_{\text{el-nuc}} \tag{2.3}$$

Solving the electronic component of the many-body Schrödinger equation yields the energy eigenstates of the electrons, which explicitly depend on the electron coordinates, with the nuclear coordinates appearing as mere parameters.

2.2 Independent Electron Approximation

While the Born-Oppenheimer approximation separates the electronic part of the many-body Hamiltonian from the nuclear part, simplifying the problem, the Hamiltonian remains a many-electron system. The electron-electron interaction term V_{ee} still couples the electronic degrees of freedom, making the solution challenging. To address this, the independent electron approximation is employed, where the electron-electron interactions are approximated by an effective periodic potential $V(r)$. In this approach, the complex interacting electron system is transformed into a system of independent electrons moving under an effective potential due to the other electrons. Two primary approaches are used: (i) Wave function-based methods, including Hartree and Hartree-Fock methods and (ii) Density Functional Theory (DFT).

Wave function-based methods, although accurate, become computationally expensive for large systems. In contrast, DFT is more computationally feasible, even for complex and extended systems. The next section will elaborate on Density Functional Theory, as it is extensively used in the thesis, implemented through the Vienna ab-initio simulation package (VASP) [1, 2] to study the electronic structures of materials.

2.3 Density Functional Theory (DFT)

Density Functional Theory (DFT) is a theoretical scheme for calculating the electronic structure based on electron density, initially proposed by Thomas and Fermi in 1927, known as the Thomas-Fermi (TF) theory [3]. However, this theory had significant limitations due to approximations in the kinetic energy of electrons and inaccuracies in the exchange energy, making it insufficient for supporting bound states. In 1964, Hohenberg and Kohn introduced a more robust formalism based on electron density, effectively addressing the N-electron Hamiltonian to accurately describe the ground-state properties of systems. This formalism is now known as DFT [4]. DFT simplifies the problem by using electron density, reducing the degrees of freedom and complexity. The electron density describes the probability of locating an electron at a particular point in space around an atom or molecule. It can be experimentally determined using techniques such as X-ray

diffraction [5]. The core idea is to replace the N-electron wave function $\Psi(r_1, \ldots, r_N)$, which depends on $3N$ variables, with the electron density $\rho(r)$, which depends only on three spatial variables. For an N-electron system, the non-spin single-particle density, derived from the normalized N-electron wave function, is given by:

$$\rho(r_i) = N \int \Psi^*(r_1, \cdots, r_i, \cdots, r_N)\Psi(r_1, \cdots, r_i, \cdots, r_N)\, dr_1\, dr_2 \cdots dr_{i-1}\, dr_{i+1} \cdots dr_N \tag{2.4}$$

This density function depends on three spatial variables and integrates to the total number of electrons in the system:

$$\int \rho(r_i)\, dr_i = N \tag{2.5}$$

Similarly, the two-particle density is defined as:

$$\rho(r_i, r_j) = N(N-1) \int \Psi^*(r_1, \ldots, r_i, \ldots, r_j, \ldots, r_N)\, \Psi(r_1, \ldots, r_i, \ldots, r_j, \ldots, r_N) \times dr_1\, dr_2 \ldots dr_{i-1}\, dr_{i+1} \ldots dr_{j-1}\, dr_{j+1} \ldots dr_N \tag{2.6}$$

This function gives the probability of finding an electron at position r_i when another electron is at r_j. If the electrons are uncorrelated, $\rho(r_i, r_j)$ can be approximated as:

$$\rho(r_i, r_j) = \rho(r_i)\rho(r_j) \tag{2.7}$$

However, in real physical systems, electrons are correlated, and the two-particle density is expressed as:

$$\rho(r_i, r_j) = \rho(r_i)\rho(r_j)\Delta\rho(r_i, r_j) \tag{2.8}$$

Here, $\Delta\rho(r_i, r_j)$ represents the correlation term, which is crucial in DFT. Electron densities contain significant information about the system, allowing all lowest energy state properties of the many-electron system to be expressed as a functional of the ground state electron density distribution. The foundation of DFT rests on two key pillars: (i) two mathematical theorems proposed by Hohenberg and Kohn [4], and (ii) A set of equations derived by Kohn and Sham [6].

2.4 The Hohenberg-Kohn Theorems

Theorem1:
For any system of interacting or non-interacting electrons subjected to an external potential $V_{\text{ext}}(\text{r})$, the ground state electron density $\rho(\mathbf{r})$ uniquely determines the external potential $V_{\text{ext}}(\mathbf{r})$ [4, 7].

Proof: The Hohenberg-Kohn theorem claims that there exists a direct equivalence between the external potential $V_{\text{ext}}(\mathbf{r})$ and the ground-state electron density $\rho(\mathbf{r})$ of a many-electron system. Using Equation. (2.3), the electronic Hamiltonian can be written as:

$$H_{\text{ele}} = K_e + V_{ee} + V_{\text{ext}},$$

where K_e denotes the kinetic energy operator and V_{ee} represents the electron-electron interaction term.

Now, consider two distinct external potentials, $V_A(\mathbf{r})$ and $V_B(\mathbf{r})$, which differ by more than a constant. Let H_A and H_B be the corresponding Hamiltonians, and Ψ_A and Ψ_B be their respective ground state wavefunctions. The time-independent Schrödinger equations for the two cases are:

$$H_A\Psi_A = E_A\Psi_A \quad \text{and} \quad H_B\Psi_B = E_B\Psi_B,$$

where E_A and E_B are the ground state energies corresponding to the Hamiltonians H_A and H_B, respectively.

Now, let us assume that two different external potentials $V_A(r)$ and $V_B(r)$ give rise to the same ground state electron density $\rho(r)$. The corresponding ground state energies are given by:

$$E_A = \langle\Psi_A|H_A|\Psi_A\rangle \tag{2.9}$$

$$E_B = \langle\Psi_B|H_B|\Psi_B\rangle \tag{2.10}$$

We can also write:

$$\langle\Psi_B|H_A|\Psi_B\rangle = \langle\Psi_B|H_B|\Psi_B\rangle + \langle\Psi_B|(H_A - H_B)|\Psi_B\rangle \tag{2.11}$$

Now, since the wave function Ψ_B does not belong to the ground state of H_A, we can write:

$$E_A < \langle \Psi_B | H_A | \Psi_B \rangle \tag{2.12}$$

$$\text{i.e.} \quad E_A < E_B + \langle \Psi_B | (H_A - H_B) | \Psi_B \rangle \tag{2.13}$$

$$\text{i.e.} \quad E_A < E_B + \langle \Psi_B | (V_A(r) - V_B(r)) | \Psi_B \rangle \tag{2.14}$$

In a similar way, we can get an expression for E_B:

$$E_B < E_A + \langle \Psi_A | (V_B(r) - V_A(r)) | \Psi_A \rangle \tag{2.15}$$

Adding equations (2.14) and (2.15), we get:

$$E_A + E_B < E_B + E_A + \langle \Psi_B | (V_A(r) - V_B(r)) | \Psi_B \rangle + \langle \Psi_A | (V_B(r) - V_A(r)) | \Psi_A \rangle \tag{2.16}$$

i.e.,

$$E_A + E_B < E_B + E_A + \langle \Psi_B | (V_A(r) - V_B(r)) | \Psi_B \rangle - \langle \Psi_A | (V_A(r) - V_B(r)) | \Psi_A \rangle \tag{2.17}$$

Since $V_A(r)$ and $V_B(r)$ both lead to the same ground state electron density $\rho(r)$, we can write:

$$E_A + E_B < E_B + E_A + \int \rho(r)[V_A(r) - V_B(r)]\, d^3r - \int \rho(r)[V_A(r) - V_B(r)]\, d^3r \tag{2.18}$$

which leads to:

$$E_A + E_B < E_B + E_A \tag{2.19}$$

This contradiction proves that our initial assumption,that two different external potentials can give rise to the similar ground state density, is wrong. This implies that the ground state density uniquely determines the external potential (except for an additive constant).

Theorem II: The energy of a many-electron system can be written as a universal functional of the charge density, $E[\rho(r)]$. The ground state energy of the system is the global minimum of this functional, obtained via the variational principle. The charge density that corresponds to this minimum energy is called the ground state charge density.

For an N-electron system specified by the Hamiltonian $\hat{H} = \hat{T}_e + \hat{V}_{ee} + \hat{V}_{\text{ext}}$, the total energy functional can be written in terms of the electron density $\rho(r)$ as:

$$E[\rho(r)] = \langle \Psi | \hat{H} | \Psi \rangle \tag{2.22}$$

$$E[\rho(r)] = \int \rho(r) \left[\hat{T}_e + \hat{V}_{ee} + \hat{V}_{\text{ext}} \right] (r)\, d^3r \tag{2.23}$$

$$E[\rho(r)] = T[\rho(r)] + E_{ee}[\rho(r)] + \int \rho(r) V_{\text{ext}}(r)\, d^3r \tag{2.20}$$

Here, $T[\rho(r)]$ is the kinetic energy functional and $E_{ee}[\rho(r)]$ represents the electron-electron interaction energy. These two terms together define the Hohenberg-Kohn functional:

$$F[\rho(r)] = T[\rho(r)] + E_{ee}[\rho(r)] \tag{2.21}$$

The ground state energy $E_0[\rho(r)]$ of the many-electron system can be uniquely determined by minimizing the total energy functional $E[\rho(r)]$ for a given external potential $V_{\text{ext}}(r)$. The electron density corresponding to this minimum is called the ground state charge density, denoted by $\rho_0(r)$. Therefore, for any other trial density $\rho'(r)$, the following inequality holds:

$$E[\rho'(r)] \geq E[\rho_0(r)] \tag{2.22}$$

2.5 Kohn-Sham Formulation

Computing the optimized state energy of an interacting system with N electrons is challenging because the exact form of the Hohenberg-Kohn functional is unknown. In 1965, Kohn and Sham introduced a formalism [6] that offers an approximate but accurate representation of the Hohenberg-Kohn functional $F[\rho(r)]$. The electron-electron interaction energy can be written as

$$E_{ee}[\rho(r)] = \frac{1}{2} e^2 \int \int d\mathbf{r}_i d\mathbf{r}_j \frac{\rho(\mathbf{r}_i, \mathbf{r}_j)}{|\mathbf{r}_i - \mathbf{r}_j|}, \tag{2.23}$$

where $\rho(\mathbf{r}_i, \mathbf{r}_j)$ represents the two-particle density. For an interacting electron system, this density can be factorized as

$$\rho(\mathbf{r}_i, \mathbf{r}_j) = \rho(\mathbf{r}_i)\rho(\mathbf{r}_j)\Delta\rho(\mathbf{r}_i, \mathbf{r}_j). \tag{2.24}$$

Introducing the correlation function $f(\mathbf{r}_i, \mathbf{r}_j)$, one can rewrite this as

$$\rho(\mathbf{r}_i, \mathbf{r}_j) = \rho(\mathbf{r}_i)\rho(\mathbf{r}_j)\left[1 - f(\mathbf{r}_i, \mathbf{r}_j)\right], \tag{2.25}$$

with

$$\Delta\rho(\mathbf{r}_i, \mathbf{r}_j) = 1 - f(\mathbf{r}_i, \mathbf{r}_j). \tag{2.26}$$

Substituting this back into the expression for E_{ee}, we obtain

$$E_{ee}[\rho(\mathbf{r})] = \frac{1}{2}e^2 \int\int d\mathbf{r}_i d\mathbf{r}_j \frac{\rho(\mathbf{r}_i)\rho(\mathbf{r}_j)}{|\mathbf{r}_i - \mathbf{r}_j|} + \frac{1}{2}e^2 \int\int d\mathbf{r}_i d\mathbf{r}_j \frac{\rho(\mathbf{r}_i)\rho(\mathbf{r}_j)}{|\mathbf{r}_i - \mathbf{r}_j|} f(\mathbf{r}_i, \mathbf{r}_j). \tag{2.27}$$

This can be expressed compactly as

$$E_{ee}[\rho(\mathbf{r})] = E_H[\rho(\mathbf{r})] + \Delta E_{ee}, \tag{2.28}$$

where the Hartree energy

$$E_H[\rho(\mathbf{r})] = \frac{1}{2}e^2 \int\int d\mathbf{r}_i d\mathbf{r}_j \frac{\rho(\mathbf{r}_i)\rho(\mathbf{r}_j)}{|\mathbf{r}_i - \mathbf{r}_j|} \tag{2.29}$$

represents the classical Coulomb interaction between electrons, and

$$\Delta E_{ee} = \frac{1}{2}e^2 \int\int d\mathbf{r}_i d\mathbf{r}_j \frac{\rho(\mathbf{r}_i)\rho(\mathbf{r}_j)}{|\mathbf{r}_i - \mathbf{r}_j|} f(\mathbf{r}_i, \mathbf{r}_j) \tag{2.30}$$

accounts for electron-electron correlations.

Handling the kinetic energy term $T[\rho(r)]$ is complicated because it involves derivatives. To simplify, the interacting system's charge density is approximated by that of a non-interacting system described by

$$\rho(r) = 2\sum_{i=1}^{N} \phi_i^*(r)\phi_i(r), \tag{2.31}$$

where ϕ_i are the Kohn-Sham orbitals, and the factor of 2 includes spin degeneracy. The kinetic energy of this fictitious system is

$$T_0[\rho(r)] = \sum_{i=1}^{N} \langle \phi_i | -\frac{\hbar^2}{2m_e}\nabla^2 | \phi_i \rangle. \tag{2.32}$$

These orbitals are not physically real but mathematical constructs. Hence, the actual kinetic energy is decomposed as

$$T[\rho(r)] = T_0[\rho(r)] + \Delta T_{ee}, \tag{2.33}$$

where ΔT_{ee} captures the kinetic energy corrections due to interactions. Incorporating this into the energy functional yields

$$F[\rho(r)] = T_0[\rho(r)] + \Delta T_{ee} + E_H[\rho(r)] + \Delta E_{ee}. \tag{2.34}$$

The correlation contributions ΔT_{ee} and ΔE_{ee} are combined into the exchange-correlation energy

$$E_{XC}[\rho(r)] = \Delta T_{ee} + \Delta E_{ee}, \tag{2.35}$$

so the functional takes the form

$$F[\rho(r)] = T_0[\rho(r)] + E_H[\rho(r)] + E_{XC}[\rho(r)]. \tag{2.36}$$

The ground state energy is found by minimizing the total energy functional $E[\rho(r)]$, subject to the constraint that the number of electrons N remains fixed:

$$\int \rho(r)\, dr = N. \tag{2.37}$$

Applying the variational principle with a Lagrange multiplier μ_L to enforce this constraint results in

$$\frac{\delta}{\delta\rho(r)}\left[F[\rho(r)] + \int \rho(r)V_{\text{ext}}(r)\,d^3r - \mu_L\left(\int \rho(r)\,d^3r - N\right)\right] = 0, \tag{2.38}$$

which simplifies to

$$\mu_L = \frac{\delta F[\rho(r)]}{\delta\rho(r)} + V_{\text{ext}}(r). \tag{2.39}$$

Substituting the explicit form of $F[\rho(r)]$ yields

$$\mu_L = \frac{\delta T_0[\rho(r)]}{\delta\rho(r)} + \frac{\delta E_H[\rho(r)]}{\delta\rho(r)} + \frac{\delta E_{XC}[\rho(r)]}{\delta\rho(r)} + V_{\text{ext}}(r). \tag{2.40}$$

Defining

$$V_H(r) = \frac{\delta E_H[\rho(r)]}{\delta\rho(r)}, \quad V_{XC}(r) = \frac{\delta E_{XC}[\rho(r)]}{\delta\rho(r)}, \tag{2.41}$$

we rewrite

$$\mu_L = \frac{\delta T_0[\rho(r)]}{\delta\rho(r)} + V_H(r) + V_{XC}(r) + V_{\text{ext}}(r). \tag{2.42}$$

This equation leads to the Kohn-Sham equations obtained by minimizing the energy functional:

$$\left[-\frac{\hbar^2}{2m}\nabla^2 + V_H(r) + V_{XC}(r) + V_{\text{ext}}(r)\right]\phi_i(r) = \epsilon_i\phi_i(r). \tag{2.43}$$

The exact form of $V_{XC}(r)$ is unknown, and the sum of potentials

$$V_{KS}(r) = V_H(r) + V_{XC}(r) + V_{\text{ext}}(r) \tag{2.44}$$

defines the Kohn-Sham potential. Thus, the equation can be compactly written as

$$\left[-\frac{\hbar^2}{2m}\nabla^2 + V_{KS}(r)\right]\phi_i(r) = \epsilon_i\phi_i(r). \tag{2.45}$$

It is important to note that the orbitals $\phi_i(r)$ and eigenvalues ϵ_i serve as mathematical tools without direct physical meaning; only the electron density resulting from these orbitals corresponds to the physical ground state. Since the Kohn-Sham potential depends

on the electron density, which itself depends on the orbitals, the equations are solved iteratively as follows [8]:

1. Start with an initial guess for the electron density $\rho(r)$.
2. Compute $V_{KS}[\rho(r)]$ and solve the Kohn-Sham equations to obtain $\phi_i(r)$.
3. Use these orbitals to calculate a new density:

$$\rho_{KS}(r) = 2\sum_i \phi_i^*(r)\phi_i(r). \tag{2.46}$$

4. Check if $\rho_{KS}(r)$ agrees with the previous $\rho(r)$ within a tolerance. If so, accept $\rho_{KS}(r)$ as the solution; otherwise, update $\rho(r)$ and repeat from step 2.

2.6 The Exchange-Correlation Functional Approximation

2.6.1 The Local Density Approximation (LDA)

The Local Density Approximation (LDA) was given by Hohenberg and Kohn in 1965, [4] and assumes that the exchange-correlation energy density relies only on the local electron density. At each point, the exchange-correlation energy is approximated by that of a homogeneous electron gas (HEG) at the corresponding density:

$$E_{LDA}^{XC}[\rho(r)] = \int \rho(r)\epsilon_{HEG}^{XC}[\rho(r)]\, d^3r, \tag{2.47}$$

where $\epsilon_{HEG}^{XC}[\rho(r)]$ can be divided into exchange and correlation parts:

$$\epsilon_{HEG}^{XC}[\rho(r)] = \epsilon_{HEG}^{X}[\rho(r)] + \epsilon_{HEG}^{C}[\rho(r)]. \tag{2.48}$$

The exchange energy per electron, derived analytically by Dirac [9], is

$$\epsilon_{HEG}^{X}[\rho(r)] = -\frac{3}{4}e^2\left(\frac{3\rho(r)}{\pi}\right)^{1/3}. \tag{2.49}$$

The correlation energy per electron, $\epsilon_{HEG}^{C}[\rho(r)]$, is known exactly only in the limiting cases of low [10, 11] and high electron density:

$$\epsilon_{low}^{C}[\rho(r)] = \frac{1}{2}\left(a_1 r_s + a_2 r_s^{3/2} + \cdots\right), \tag{2.50}$$

$$\epsilon_{high}^{C}[\rho(r)] = A_1 + A_2 r_s + (A_3 + A_4 r_s)\ln(r_s), \tag{2.51}$$

where the Wigner-Seitz radius r_s is related to the electron density by

$$\frac{4}{3}\pi r_s^3 = \frac{1}{\rho(r)}. \tag{2.52}$$

For intermediate densities, Quantum Monte Carlo calculations provide numerical values. Various parameterizations such as Vosko-Wilk-Nusair (VWN) [12], Perdew-Zunger (PZ81) [13], Cole-Perdew (CP) [14], and Perdew-Wang (PW92) [15] are commonly used. The LDA gives best performs where electron density vary slowly but it undersestimates the lattice constants and band gaps while overestimating binding energies.

2.6.2 Generalized Gradient Approximation (GGA)

The Local Density Approximation (LDA) often falls short in accurately describing systems where the electron density is strongly non-uniform, such as in the formation of spatially directed chemical bonds. To account for this inhomogeneity, the Generalized Gradient Approximation (GGA) was developed. Unlike LDA, GGA includes not only the local electron density but also its gradient in the exchange-correlation energy functional. The exchange-correlation energy in GGA can be expressed as:

$$E_{GGA}^{XC}[\rho(\mathbf{r})] = \int \rho(\mathbf{r})\, \epsilon_{HEG}^{XC}[\rho(\mathbf{r}), |\nabla\rho(\mathbf{r})|]\, d^3r \tag{2.53}$$

Different choices for the functional form of ϵ_{HEG}^{XC} have led to various GGA functionals, including those by Perdew and Wang [15], Becke-Lee-Yang-Parr (BLYP) [16], and Perdew-Burke-Ernzerhof (PBE) [17]. While GGA typically improves predictions of atomization energies, total energies, and structural energy differences relative to LDA, it can sometimes overcorrect LDA results. Generally, GGA performs better than LDA for systems with strong electron correlation.

2.6.3 Hybrid Functionals

Hybrid functionals represent a prevalent class of exchange-correlation approximations that add a fraction of exact Hartree-Fock (HF) exchange with exchange-correlation from conventional functionals such as LDA or GGA. Prominent examples include B3LYP [18], PBE0 [17] , and the Heyd-Scuseria-Ernzerhof (HSE) functional [1].

The HSE functional, widely used in solid-state calculations, incorporates a screened Coulomb potential for the exchange part. Its exchange-correlation energy takes the form:

$$E_{XC}^{HSE} = \alpha E_X^{HF,SR} + (1-\alpha)E_X^{PBE,SR} + E_X^{PBE,LR} + E_C^{PBE} \tag{2.54}$$

Here, α is the mixing parameter; $E_X^{HF,SR}$ denotes short-range Hartree-Fock exchange; $E_X^{PBE,SR}$ and $E_X^{PBE,LR}$ are the short- and long-range PBE exchange contributions, respectively; and E_C^{PBE} is the PBE correlation energy. Since the HF exchange term E_X^{HF} is inherently non-local, its evaluation requires knowledge of the Kohn-Sham orbitals ϕ_i over all space, making hybrid functionals computationally demanding. Nevertheless, their improved accuracy, especially for strongly correlated systems, often justifies the higher cost.

2.7 Numerical Approximations for DFT Calculations

The Kohn-Sham equations are solved iteratively to obtain the ground-state electron density. Due to the unknown exact exchange-correlation functional, numerical approximations are necessary, such as finite grid integrations and truncated infinite sums. These approximations introduce small errors, so the final converged solution is an approximation close to the exact one.

2.7.1 Plane Wave Basis and Cut-off Energy

For crystalline solids, where electrons move in a periodic potential, the single-electron Kohn-Sham orbitals $\phi_i(\mathbf{r})$ can be expressed following the Bloch's theorem:

$$\phi_i(\mathbf{r}) = e^{i\mathbf{k}\cdot\mathbf{r}} u_i(\mathbf{r}) \tag{2.55}$$

with $u_i(\mathbf{r}+\mathbf{T}) = u_i(\mathbf{r})$, $\mathbf{T}$ being a lattice translation vector. Due to periodicity, $u_i(\mathbf{r})$ can be expanded as a Fourier series of plane waves:

$$u_i(\mathbf{r}) = \sum_G C_G e^{iG\cdot\mathbf{r}} \tag{2.56}$$

where G represents the reciprocal lattice vector. Thus,

$$\phi_i(\mathbf{r}) = \sum_G C_{G+k} e^{i(G+k)\cdot\mathbf{r}} \tag{2.57}$$

This infinite series of plane waves, each with kinetic energy $E = \frac{\hbar^2}{2m}|k+G|^2$, is truncated by imposing a cutoff energy E_{cut}:

$$E_{\text{cut}} = \frac{\hbar^2}{2m} G_{\text{cut}}^2 \tag{2.58}$$

Only plane waves with kinetic energies below E_{cut} are included. Increasing E_{cut} reduces truncation error until convergence is achieved.

2.7.2 K-Space Integrations

In density functional theory (DFT), a considerable amount of computational effort is dedicated to evaluating integrals over the Brillouin zone (BZ) in k space. These integrals typically take the form

$$f = \frac{V}{(2\pi)^3} \int_{\text{BZ}} f(\text{k})\, d\text{k} \tag{2.59}$$

where v denotes volume of the unit cell and $f(\text{k})$ is a function defined over momentum space within the Brillouin zone. Because evaluating this integral analytically is often impractical, it is usually approximated by a weighted summation over a discrete set of k points. The precision of this approximation improves as the number of sampled k points increases. With a sufficiently dense mesh, the numerical estimate can closely match the exact result. Therefore, it is crucial to select an appropriate k-point mesh to ensure both computational efficiency and accuracy. Among the standard approaches for generating k-point grids are the Γ-centered mesh and the Monkhorst-Pack scheme. In the Monkhorst-Pack method, the Brillouin zone is divided into a uniform grid of points. When N points are chosen along each of the three reciprocal lattice directions, the resulting mesh is described as an $N \times N \times N$ k grid. To verify that the computed quantities, such as the total energy, are well-converged for k point sampling, one incrementally increases N and

monitors the changes. Once the total energy stabilizes with increasing N, the mesh is considered sufficiently dense for reliable results.

2.7.3 Pseudopotential and Frozen Core Approximation

The electronic states in an atom are typically divided into two categories: (i)Core electron states, which are localized and tightly bound to the nucleus, (ii)Valence electron states, which are delocalized and significantly influence the electronic properties of a material. Core electrons, due to their strong binding, exhibit rapidly oscillating wavefunctions over short length scales and possess substantially higher kinetic energy compared to valence electrons. Accurately describing these states within a plane-wave basis requires a very high energy cutoff, thereby increasing the computational burden.

To reduce this computational demand, approximations are introduced in the treatment of core electrons. This leads to the development of pseudopotential theory, where the pseudopotential is constructed to accurately replicate the behavior of valence electrons while omitting the explicit treatment of core states. This method ensures that the essential electronic and physical properties of the system remain unchanged and is widely known as the frozen-core approximation.Let the wavefunctions corresponding to core and valence electrons be denoted by $|\psi_c\rangle$ and $|\psi_v\rangle$, respectively. These satisfy the single-electron Schrödinger equations:

$$H|\psi_c\rangle = \varepsilon_c|\psi_c\rangle \tag{2.60}$$

$$H|\psi_v\rangle = \varepsilon_v|\psi_v\rangle \tag{2.61}$$

where H is the single-particle Hamiltonian, and ε_c and ε_v are the eigenvalues associated with the core and valence states, respectively.

In the pseudopotential approximation, the electron density associated with the core states is replaced by a smooth function. To implement this, a modified valence wavefunction $|\phi_v\rangle$ is constructed as

$$|\phi_v\rangle = |\psi_v\rangle + \sum_c \alpha_c|\psi_c\rangle \tag{2.62}$$

The coefficients α_c are determined from the orthogonality condition $\langle\psi_c|\psi_v\rangle = 0$, which leads to $\alpha_c = \langle\psi_c|\phi_v\rangle$. Substituting this into the above equation, we obtain

$$|\phi_v\rangle = |\psi_v\rangle + \sum_c |\psi_c\rangle\langle\psi_c|\phi_v\rangle \tag{2.63}$$

Solving for $|\psi_v\rangle$, we get

$$|\psi_v\rangle = |\phi_v\rangle - \sum_c |\psi_c\rangle\langle\psi_c|\phi_v\rangle \tag{2.64}$$

Substituting this expression for $|\psi_v\rangle$ into the earlier equation yields

$$H\left(|\phi_v\rangle - \sum_c |\psi_c\rangle\langle\psi_c|\phi_v\rangle\right) = \varepsilon_v\left(|\phi_v\rangle - \sum_c |\psi_c\rangle\langle\psi_c|\phi_v\rangle\right) \tag{2.65}$$

This can be rearranged into the following form:

$$\left[H + \sum_c (\varepsilon_v - \varepsilon_c)|\psi_c\rangle\langle\psi_c|\right]|\phi_v\rangle = \varepsilon_v|\phi_v\rangle \tag{2.66}$$

The new valence electron states $|\phi_v\rangle$ satisfy the single-particle equation with a modified potential that reproduces the same eigenvalues ε_v as those of the original valence states $|\psi_v\rangle$. The modified Hamiltonian is referred to as the pseudo-Hamiltonian, defined as

$$H_{\mathrm{PH}} = H + \sum_c (\varepsilon_v - \varepsilon_c)|\psi_c\rangle\langle\psi_c| \tag{2.67}$$

Correspondingly, the modified nuclear potential is called the pseudopotential, given by

$$V_{\mathrm{PS}} = V + \sum_c (\varepsilon_v - \varepsilon_c)|\psi_c\rangle\langle\psi_c| \tag{2.68}$$

where V is the attractive nuclear potential in the original Hamiltonian H, and the second term acts as a correction. This correction is strictly repulsive because $\varepsilon_v > \varepsilon_c$, which results in pushing the valence states $|\phi_v\rangle$ away from the core region. Due to the presence of this repulsive correction, the valence electrons experience a nuclear potential that is effectively screened near the nucleus within the core region. Consequently, the effective pseudopotential becomes much smoother and does not exhibit the $1/r$ singularity characteristic of the bare nuclear potential at the center. This smoothing causes the corresponding valence wavefunctions to be much less oscillatory in the core region. Fig. 2.1 schematically illustrates the pseudopotential approach. As shown, there exists a cutoff radius r_c beyond which the pseudopotential and the pseudo wavefunctions coincide exactly with the original potential and the original electron wavefunctions, respectively. Inside the core region, that is for $r < r_c$, the valence states experience a weaker potential. A variety of formalisms have been developed to generate smoother yet accurate pseudopotentials. One widely used approach is the norm-conserving pseudopotential method, first introduced by Hamann, Schlüter, and Chiang [20]. In this method, within the core radius

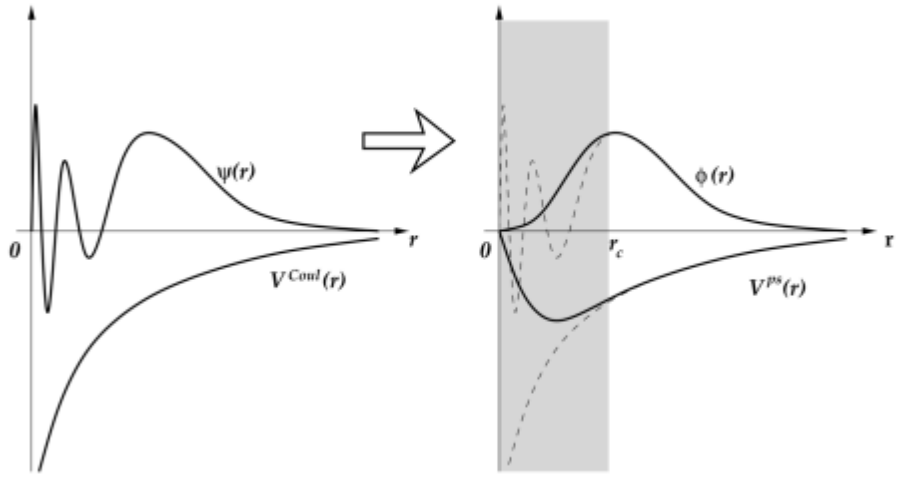

Figure 2.1: The left panel illustrates a schematic of the valence electron wave function $\psi(r)$ alongside the Coulomb potential $V_{\text{coul}}(r)$. The right panel presents a schematic representation of the pseudopotential $V_{\text{PS}}(r)$ [19].

r_c, the all-electron wavefunction is replaced by an effective pseudo-wavefunction, with the crucial constraint that both wavefunctions have the same norm within r_c. Beyond this radius, the pseudo and all-electron wavefunctions coincide exactly.

To ensure good transferability,that is, reliable performance of the pseudopotential in different chemical environments,the core radius r_c is typically chosen near the outer radial maximum of the all-electron wavefunction. This choice guarantees that the pseudo-wavefunction accurately reproduces the charge distribution and multipole moments of the all-electron wavefunction. However, for elements with the orbitals which are strongly localized such as $3d$ transition metals and rare-earth elements, the plane-wave basis set should be large to describe the pseudopotential adequately. If the core radius is taken beyond the outermost maximum, the transferability of the pseudopotential tends to degrade. Furthermore, difficulties arise for first-row elements in the periodic table, which lack core electrons. To address these limitations, Vanderbilt proposed the ultrasoft pseudopotential (USPP) method in 1990, which relaxes the norm-conserving constraint. This relaxation allows a reduction in the required basis set size, thereby improving computational efficiency. One drawback of pseudopotential approaches is the loss of detailed wavefunction information near the nuclei, which can affect the prediction of material properties that depend critically on core electrons. To resolve this, the Projector Augmented Wave (PAW) method was developed, which retains all-electron wavefunction information while maintaining computational efficiency.

2.7.4 Projector Augmented-Wave(PAW) Method

The Projector Augmented Wave (PAW) method, originally proposed by Blöchl in 1994 [21], was subsequently modified by Kresse and Joubert for use in plane-wave-based calculations [22]. This approach constructs the all-electron wavefunction as composed of smooth functions that extend over space and localized contributions from muffin-tin orbitals [23].

In the PAW formalism, the all-electron valence wavefunction $\psi_j^v(\mathbf{r})$ is expressed in terms of a smooth pseudo valence wavefunction $\tilde{\psi}_j^v(\mathbf{r})$ and a linear transformation that restores the nodal structure near atomic cores:

$$\psi_j^v(\mathbf{r}) = \tilde{\psi}_j^v(\mathbf{r}) + \sum_i \left(|\phi_i\rangle - |\tilde{\phi}_i\rangle \right) \langle \tilde{p}_i | \tilde{\psi}_j^v \rangle \tag{2.69}$$

Here, the index i runs over atomic sites $\mathbf{R}$ and partial waves, $|\phi_i\rangle$ and $|\tilde{\phi}_i\rangle$ are the all-electron and pseudo partial waves respectively, while $\langle \tilde{p}_i|$ are projector functions associated with the pseudo partial waves. These projectors satisfy the orthogonality condition:

$$\langle \tilde{p}_i | \tilde{\phi}_j \rangle = \delta_{ij} \tag{2.70}$$

This construction allows the computation of all physical integrals using smooth functions, combined with localized corrections, thereby preserving the accuracy of all-electron calculations while maintaining computational efficiency. The total all-electron charge density can be expressed as the sum of the smooth pseudo-charge density and the difference between the onsite all-electron and pseudo-charge densities:

$$\rho(\mathrm{r}) = \tilde{\rho}(\mathrm{r}) + \rho^1(\mathrm{r}) - \tilde{\rho}^1(\mathrm{r}), \tag{2.71}$$

where

$$\tilde{\rho}(\mathrm{r}) = \sum_i f_i \, |\tilde{\psi}_i(\mathrm{r})|^2, \tag{2.72}$$

$$\rho^1(\mathrm{r}) = \sum_i f_i \sum_{j,k} \langle \tilde{\psi}_i | \tilde{p}_j \rangle \phi_j(\mathrm{r}) \phi_k(\mathrm{r}) \langle \tilde{p}_k | \tilde{\psi}_i \rangle, \tag{2.73}$$

$$\tilde{\rho}^1(\mathrm{r}) = \sum_i f_i \sum_{j,k} \langle \tilde{\psi}_i | \tilde{p}_j \rangle \tilde{\phi}_j(\mathrm{r}) \tilde{\phi}_k(\mathrm{r}) \langle \tilde{p}_k | \tilde{\psi}_i \rangle. \tag{2.74}$$

In the equations above, f_i represents the occupancy of each eigenstate $\tilde{\psi}_i$. The pseudo-charge density $\tilde{\rho}(\mathrm{r})$ is derived from the pseudo-wavefunctions expressed in a plane wave basis. Meanwhile, $\rho^1(\mathrm{r})$ and $\tilde{\rho}^1(\mathrm{r})$ correspond to onsite charge densities confined within

the augmentation spheres surrounding each atom. When evaluating the total energy of the system, contributions from these three charge densities are accounted for separately, reflecting their distinct spatial localizations.

2.7.5 Tight Binding Approximation

The Tight Binding Approximation is a semi-empirical technique used to calculate the electronic structure of crystals and molecules. It builds upon the Linear Combination of Atomic Orbitals (LCAO) approach, originally introduced by Bloch in 1928 [24]. Later, in 1954, Slater and Koster [25] developed a method to parameterize the tight binding model for several lattice types, including simple cubic, body-centered cubic, face-centered cubic, and diamond structures . In this framework, the electronic wavefunction of a periodic crystal is expressed as a Bloch sum of atomic orbitals, which are assumed to be strongly localized at their respective atomic sites. Consider a set of atomic wavefunctions $\phi_l(\mathbf{r} - \mathbf{t}_m)$, where $\mathbf{t}_m$ denotes the position of the m-th atom within the unit cell, and l represents the angular momentum quantum number characterizing the orbital type (such as s, p, d, etc.). Based on Bloch's theorem, a basis set for a periodic lattice can be formed by using these atomic wavefunctions as building blocks:

$$\Phi_{k,l,m}(\mathrm{r}) = \frac{1}{\sqrt{N}} \sum_{\mathrm{R}} e^{i\mathrm{k}\cdot\mathrm{R}}\, \phi_l(\mathrm{r} - \mathrm{t}_m - \mathrm{R}) \tag{2.75}$$

Here, N denotes the total number of unit cells in the crystal, and R refers to the lattice translation vector. Using the Bloch-like basis functions defined earlier, the single-particle wavefunctions can be expressed as a linear combination:

$$\psi_{\mathrm{k}i}(\mathrm{r}) = \sum_{l,m} c_{\mathrm{k},l,m}\, \Phi_{\mathrm{k},l,m}(\mathrm{r}) \tag{2.76}$$

The coefficients $c_{\mathrm{k},l,m}$ are determined by requiring that $\psi_{\mathrm{k}i}(\mathrm{r})$ satisfies the single-particle Schrödinger equation:

$$\hat{H}_{\mathrm{SP}}\, \psi_{\mathrm{k}i}(\mathrm{r}) = \varepsilon_{\mathrm{k}}\, \psi_{\mathrm{k}i}(\mathrm{r}) \tag{2.77}$$

Substituting the expansion of $\psi_{\mathrm{k}i}(\mathrm{r})$ into the above yields:

$$\sum_{l,m} c_{\mathrm{k},l,m}\, \hat{H}_{\mathrm{SP}} \Phi_{\mathrm{k},l,m}(\mathrm{r}) = \varepsilon_{\mathrm{k}} \sum_{l,m} c_{\mathrm{k},l,m}\, \Phi_{\mathrm{k},l,m}(\mathrm{r}) \tag{2.78}$$

Projecting onto the conjugate basis function $\Phi_{\mathrm{k},j,n}$, we obtain the secular equation:

$$\sum_{l,m} \left[\langle \Phi_{\mathrm{k},j,n} | \hat{H}_{\mathrm{SP}} | \Phi_{\mathrm{k},l,m} \rangle - \varepsilon_{\mathrm{k}} \langle \Phi_{\mathrm{k},j,n} | \Phi_{\mathrm{k},l,m} \rangle \right] c_{\mathrm{k},l,m} = 0 \tag{2.79}$$

The wavefunctions obey the orthonormality condition:

$$\langle \psi_{\mathrm{k}i} | \psi_{\mathrm{k}'i'} \rangle = \delta(\mathrm{k} - \mathrm{k}') \tag{2.80}$$

with both k and k′ confined within the first Brillouin zone. The overlap between basis functions is evaluated as:

$$\langle \Phi_{\mathrm{k},j,n} | \Phi_{\mathrm{k},l,m} \rangle = \frac{1}{N} \sum_{\mathrm{R},\mathrm{R}'} e^{i\mathrm{k}\cdot(\mathrm{R}'-\mathrm{R})} \langle \phi_j(\mathrm{r} - \mathrm{t}_n - \mathrm{R}') | \phi_l(\mathrm{r} - \mathrm{t}_m - \mathrm{R}) \rangle \tag{2.81}$$

$$= \sum_{\mathrm{R}} e^{i\mathrm{k}\cdot\mathrm{R}} \langle \phi_j(\mathrm{r} - \mathrm{t}_n) | \phi_l(\mathrm{r} - \mathrm{t}_m - \mathrm{R}) \rangle \tag{2.82}$$

The quantity $\langle \phi_j(\mathrm{r} - \mathrm{t}_n) | \phi_l(\mathrm{r} - \mathrm{t}_m - \mathrm{R}) \rangle$ is called the overlap integral, representing the degree of orbital overlap between atoms on different sites. Similarly, the Hamiltonian matrix elements in this basis are given by:

$$\langle \Phi_{\mathrm{k},j,n} | \hat{H} | \Phi_{\mathrm{k},l,m} \rangle = \sum_{\mathrm{R}} e^{i\mathrm{k}\cdot\mathrm{R}} \langle \phi_j(\mathrm{r} - \mathrm{t}_n) | \hat{H} | \phi_l(\mathrm{r} - \mathrm{t}_m - \mathrm{R}) \rangle \tag{2.83}$$

At this stage, a simplification is introduced: for atomic orbitals located on the same atom, the overlap matrix element is assumed to be non-zero only when both orbitals are of the same type and centered on the same atom. This condition is mathematically expressed as:

$$\langle \phi_j(\mathrm{r} - \mathrm{t}_n) | \phi_l(\mathrm{r} - \mathrm{t}_m - \mathrm{R}) \rangle = \delta_{j,l}\, \delta_{m,n}\, \delta(\mathrm{R}) \tag{2.84}$$

Similarly, for the same atom, the Hamiltonian matrix element is non-zero only when both orbitals are identical:

$$\langle \phi_j(\mathrm{r} - \mathrm{t}_n) | \hat{H} | \phi_l(\mathrm{r} - \mathrm{t}_m - \mathrm{R}) \rangle = \delta_{j,l}\, \delta_{m,n}\, \delta(\mathrm{R})\, \varepsilon_l \tag{2.85}$$

Here, ε_l is known as the onsite energy of orbital l.

For orbitals residing on different atoms, the Hamiltonian matrix elements are generally non-zero and take the form:

$$\langle \phi_j(\mathrm{r} - \mathrm{t}_n)|\hat{H}|\phi_l(\mathrm{r} - \mathrm{t}_m - \mathrm{R})\rangle = \delta(\mathrm{t}_n - \mathrm{t}_m - \mathrm{R})\, V_{jl,nm} \tag{2.86}$$

where $V_{jl,nm}$ represents the hopping matrix element between orbitals j and l on atoms n and m, respectively.

Initial estimates for the onsite energies and Slater-Koster hopping parameters were used to construct the tight-binding model.

2.7.6 Maximally localised Wannier Functions

In 1937, Gregory Wannier introduced a novel set of basis functions, now known as Wannier functions [26]. These functions are constructed as linear combinations of Bloch orbitals through unitary transformations. Although they share some similarities with atomic orbitals in being localized in real space, Wannier functions are fundamentally distinct. Their localization depends on the system—particularly on the bandwidth. In systems with broad bands, the resulting Wannier functions may exhibit significant delocalization.

Wannier functions are not uniquely defined. This non-uniqueness arises from the phase ambiguity inherent in Bloch wavefunctions. Mathematically, Wannier functions $\psi_R^n(\mathrm{r})$ are obtained via a Fourier transform of the Bloch functions $\Phi_{n\mathrm{k}}(\mathrm{r})$, thereby providing a real-space representation of the electronic states in a periodic crystal.The most general form of the Wannier function can be written as:

$$\psi_j^R(\mathbf{r}) = \frac{V}{(2\pi)^3} \int_{\mathrm{BZ}} \left[\sum_i U_{ij}^{(\mathbf{k})}\, \Phi_{i\mathbf{k}}(\mathbf{r}) \right] e^{-i\mathbf{k}\cdot\mathbf{R}}\, d\mathbf{k} \tag{2.87}$$

The function $\psi^R(\mathbf{r})$ represents the Wannier orbital localized at lattice site $\mathbf{R}$. Here, n and m refer to band indices and $\mathbf{k}$ is the wavevector in the Brillouin zone. The unitary matrix $U(\mathbf{k})$ performs a transformation among the Bloch functions at each $\mathbf{k}$-point. Since $U(\mathbf{k})$ lacks a unique definition, different choices of it yield different sets of Wannier functions, each characterized by varying degrees of spatial localization. The degree of localization is quantified by the so-called Wannier spread, defined as:

$$\Omega = \sum_j \left[\langle \psi_j^{(0)}(\mathbf{r})|\mathbf{r}^2|\psi_j^{(0)}(\mathbf{r})\rangle - |\langle \psi_j^{(0)}(\mathbf{r})|\mathbf{r}|\psi_j^{(0)}(\mathbf{r})\rangle|^2 \right] \tag{2.88}$$

In most practical cases, $U(\mathbf{k})$ is chosen such that the total spread Ω is minimized, yielding the so-called *maximally localized Wannier functions (MLWFs)*. This method to systematically fix the gauge freedom in $U(\mathbf{k})$ was first proposed by Marzari and Vanderbilt [27].

The total Wannier spread can be separated into two components: a gauge-idependent part Ω_{I}, and a gauge-dependent part $\widetilde{\Omega}$. The gauge-dependent can further be decomposed into diagonal (Ω_{D}) and off-diagonal (Ω_{OD}) contributions:

$$\Omega = \Omega_{\mathrm{I}} + \widetilde{\Omega} = \Omega_{\mathrm{I}} + \Omega_{\mathrm{D}} + \Omega_{\mathrm{OD}} \tag{2.89}$$

These components are given by:

$$\Omega_{\mathrm{I}} = \sum_{j} \left[\langle \psi_j^{(0)}(\mathbf{r}) | \mathbf{r}^2 | \psi_j^{(0)}(\mathbf{r}) \rangle - \sum_{\mathbf{R},i} |\langle \psi_i^{(\mathbf{R})}(\mathbf{r}) | \mathbf{r} | \psi_j^{(0)}(\mathbf{r}) \rangle|^2 \right] \tag{2.90}$$

$$\Omega_{\mathrm{D}} = \sum_{j} \sum_{\mathbf{R}\neq 0} |\langle \psi_j^{(\mathbf{R})}(\mathbf{r}) | \mathbf{r} | \psi_j^{(0)}(\mathbf{r}) \rangle|^2 \tag{2.91}$$

$$\Omega_{\mathrm{OD}} = \sum_{i\neq j} \sum_{\mathbf{R}} |\langle \psi_i^{(\mathbf{R})}(\mathbf{r}) | \mathbf{r} | \psi_j^{(0)}(\mathbf{r}) \rangle|^2 \tag{2.92}$$

While this approach works well for isolated groups of bands, dealing with entangled bands, especially near $\mathbf{k}$-points where bands overlap or hybridize, is more challenging. To address this, a disentanglement algorithm [28] is employed to extract well-localized Wannier functions even from entangled bands.

2.8 Hubbard Model

We previously introduced the fundamental concepts of the Hubbard model in Chapter 1. In this section, we describe the specific form of the Hubbard model employed in our calculations. In the case of transition metal compounds, the key features of the electronic structure near the Fermi level predominantly stem from the hybridization between transition metal and ligand atom states. Therefore, an appropriate choice of basis for modeling such systems includes the transition metal d-orbitals along with the ligand s-

and p-orbitals. Using this basis, the multiband Hubbard Hamiltonian can be written as:

$$\begin{aligned} H = & \sum_{i,l,\sigma} \epsilon_d \, d^{\dagger}_{il\sigma} d_{il\sigma} + \sum_{i,l,\sigma} \epsilon_p \, p^{\dagger}_{il\sigma} p_{il\sigma} + \sum_{i,l,\sigma} \epsilon_s \, s^{\dagger}_{il\sigma} s_{il\sigma} \\ & - \sum_{i,j,l_1,l_2,\sigma} \left(t^{l_1 l_2}_{ij,pd} \, d^{\dagger}_{il_1\sigma} p_{jl_2\sigma} + \text{H.c.} \right) \\ & - \sum_{i,j,l_1,l_2,\sigma} \left(t^{l_1 l_2}_{ij,pp} \, p^{\dagger}_{il_1\sigma} p_{jl_2\sigma} + \text{H.c.} \right) \\ & - \sum_{i,j,l_1,l_2,\sigma} \left(t^{l_1 l_2}_{ij,sd} \, d^{\dagger}_{il_1\sigma} s_{jl_2\sigma} + \text{H.c.} \right) \\ & + \sum_{\alpha,\beta,\gamma,\delta;\, \sigma_1,\sigma_2,\sigma_3,\sigma_4} U^{dd}_{\alpha\beta\gamma\delta} \, d^{\dagger}_{\alpha\sigma_1} d^{\dagger}_{\beta\sigma_2} d_{\gamma\sigma_3} d_{\delta\sigma_4} \end{aligned} \tag{2.93}$$

Here, ϵ_d, ϵ_p, and ϵ_s are the onsite energies for the d-, p-, and s-orbitals respectively. The $t^{l_1 l_2}_{ij,\mu\nu}$ terms denote the hopping integrals between orbitals μ and ν, and the last term indicates the local Coulomb interactions between d-electrons on the transition metal sites. Here, $d^{\dagger}_{il\sigma}$ ($d_{il\sigma}$) denotes the creation (annihilation) operator for an electron with spin σ in the l-th d-orbital on the transition metal atom in the i-th unit cell. Similarly, $p^{\dagger}_{il\sigma}$ ($p_{il\sigma}$) and $s^{\dagger}_{il\sigma}$ ($s_{il\sigma}$) are the creation (annihilation) operators for electrons in the l-th p- or s-orbital, respectively, at the corresponding ligand site. The operator $p^{\dagger}_{il\sigma}$ ($p_{il\sigma}$) or $s^{\dagger}_{il\sigma}$ ($s_{il\sigma}$) represents the creation (annihilation) of an electron with spin σ in the l-th p- or s-orbital, respectively, of an oxygen atom located in the i-th unit cell. The oxygen s-orbitals are included in the model to effectively mimic the impact of crystal field splitting on the transition metal d-orbitals. These s-states are assumed to lie deep within the valence band and are held fixed at approximate energy levels based on prior studies.The hopping terms and onsite energy terms in the Hamiltonian are obtained directly in the matrix form by mapping the DFT electronic structure onto the nonmagnetic tight-binding model considering the Wannier functions. The model is constructed with a basis comprising transition metal d- and ligand p-orbitals.

Here matrix elements considering Columb interactions related to the transition metal d orbitals are expressed in the form of Slater integrals F^0, F^2, and F^4 [29], each having dimensions of energy. This parameterization preserves the rotational invariance of the Coulomb interaction decoupling it from the magnetic quantum number m_l and captures the essential multi orbital effects. The values of these integrals were determined using atomistic Hartree-Fock (HF) calculations. Among them, F^0 is known to be significantly screened due to solid-state effects inherent in real materials. On the other hand, F^2 and F^4 were computed based on the ionic configuration of the transition metal atoms in the oxide phase, and these were also scaled down from their atomic values to reflect screening.

In our formalism, F^0 primarily determines the multiplet-averaged Coulomb interaction strength, denoted by U, while F^2 and F^4 are adjusted to reproduce the expected intra-atomic exchange interaction in transition metal oxides. The relation between F^0 and U is given by:

$$F^0 = U + \frac{2\eta}{63}(F^2 + F^4), \tag{2.94}$$

The factor η is connected to to the Hund's exchange interaction strength J through the following relation:

$$J = \eta\frac{F^2 + F^4}{14}. \tag{2.95}$$

The parameter η is introduced to account for the screening of the intra-atomic exchange interaction strength. Its value depends on the degree of electron localization, which varies across the transition metal series. For instance, in the case of $3d$ transition metals, η typically takes a value around 0.8 eV, whereas for $4d$ and $5d$ systems, where the electrons are more delocalized, η is considerably smaller—approximately 0.3–0.4 eV for $4d$ and around 0.1 eV for $5d$ elements. In such cases, it is essential to keep the charge transfer energy (Δ) fixed while varying the Coulomb interaction parameter U. To ensure this, one must identify the most energetically favorable charge fluctuation between the oxygen p orbitals and the transition metal d orbitals. The charge transfer energy Δ is then defined as:

$$\Delta = E_f - E_i = E(d^{n+1}\underline{L}) - E(d^n), \tag{2.96}$$

where $E(d^n)$ and $E(d^{n+1}\underline{L})$ denote the total energies of the system in the d^n and d^{n+1} ligand-hole configurations, respectively.

$$\Delta = E_f - E_i = E(d^{n+1}\underline{L}) - E(d^n), \tag{2.97}$$

The above expression can be expanded including the onsite energies of the d-orbitals the transition metal, the p-orbitals of ligand, and the Coulomb interaction parameter U. The solution of the multiband Hubbard Hamiltonian given in Eq. (2.93) exactly is a difficult due to the complexity arising from the four-fermion interaction terms. Therefore, an approximate approach is required. In our work, we employ the Hartree-Fock approximation to decouple terms of the form $d^\dagger_{i\uparrow}d_{i\uparrow}d^\dagger_{i\downarrow}d_{i\downarrow}$ as follows:

$$\begin{aligned} d^\dagger_{i\uparrow}d_{i\uparrow}d^\dagger_{i\downarrow}d_{i\downarrow} = {} & \langle d^\dagger_{i\uparrow}d_{i\uparrow}\rangle d^\dagger_{i\downarrow}d_{i\downarrow} + d^\dagger_{i\uparrow}d_{i\uparrow}\langle d^\dagger_{i\downarrow}d_{i\downarrow}\rangle \\ & - \langle d^\dagger_{i\uparrow}d_{i\downarrow}\rangle d^\dagger_{i\downarrow}d_{i\uparrow} - d^\dagger_{i\uparrow}d_{i\downarrow}\langle d^\dagger_{i\downarrow}d_{i\uparrow}\rangle \\ & - \langle d^\dagger_{i\uparrow}d_{i\uparrow}\rangle\langle d^\dagger_{i\downarrow}d_{i\downarrow}\rangle + \langle d^\dagger_{i\uparrow}d_{i\downarrow}\rangle\langle d^\dagger_{i\downarrow}d_{i\uparrow}\rangle. \end{aligned} \tag{2.98}$$

Using the following ansatz for expectation values in the mean-field approximation, the order parameters (denoted by angular brackets $\langle \cdots \rangle$) are assumed to form a spiral spin density wave characterized by the wave vector q:

$$A_{il} e^{i\mathrm{q}\cdot \mathrm{R}_i} = \langle d^\dagger_{il\uparrow} d_{il\downarrow} \rangle, \tag{2.99}$$

$$A_{il_1 l_2} e^{i\mathrm{q}\cdot \mathrm{R}_i} = \langle d^\dagger_{il_1\uparrow} d_{il_2\downarrow} \rangle = \langle d^\dagger_{il_2\uparrow} d_{il_1\downarrow} \rangle, \tag{2.100}$$

and the spin-resolved occupations satisfy

$$\langle d^\dagger_{il\uparrow} d_{il\uparrow} \rangle = \langle d^\dagger_{il\downarrow} d_{il\downarrow} \rangle = \frac{n_{dl}}{2}. \tag{2.101}$$

In momentum (k) space, the creation and annihilation operators are defined via Fourier transforms as: The creation operator in momentum space can be defined as the Fourier transform of the real-space operator:

$$d^\dagger_{l\mathrm{k}\sigma} = \sum_i d^\dagger_{il\sigma} e^{i\mathrm{k}\cdot \mathrm{R}_i}. \tag{2.102}$$

Using these definitions, the mean-field Hamiltonian (H_{MF}) in momentum space can be expressed as [30]

$$H_{\mathrm{MF}} = \sum_{\mathrm{k}} \begin{bmatrix} \Phi^\dagger_{\mathrm{k}\uparrow} & \Phi^\dagger_{\mathrm{k}+\mathbf{q}\downarrow} \end{bmatrix} \begin{bmatrix} M_{\mathrm{k}} & A_{\mathrm{k}} \\ A^\dagger_{\mathrm{k}} & M_{\mathrm{k}+\mathrm{q}} \end{bmatrix} \begin{bmatrix} \Phi_{\mathrm{k}\uparrow} \\ \Phi_{\mathrm{k}+\mathrm{q}\downarrow} \end{bmatrix} - (\text{constant terms from decoupling}), \tag{2.103}$$

where $\Phi_{\mathrm{k}\uparrow}$ is a row vector containing operators $d^\dagger_{l\mathrm{k}\uparrow}$ for all l, running over the five d orbitals of transition metal. The dimension of this vector depends on size of the system.

Here, M_{k} and $M_{\mathrm{k}+\mathrm{q}}$ are matrices representing the Hamiltonian components for spin-up and spin-down states, respectively, while A_{k} arises from coupling between spin-up and spin-down states due to the spiral spin density wave ordering. The dimensions of M_{k} and A_{k} depend on the number of orbitals and system size. The constant terms come from the mean-field decoupling, for example, from terms like $\langle d^\dagger_{il\uparrow} d_{il\uparrow} \rangle \langle d^\dagger_{il\downarrow} d_{il\downarrow} \rangle$.

To obtain self-consistent solutions, standard numerical diagonalization methods are employed. The lowest energy state is determined by optimizing the expectation value of this Hamiltonian concerning the total energy, which is obtained by adding the eigenvalues up to the occupied level.

2.9 The Calculation of the Seebeck and Hall coefficient

Boltzmann transport theory [31,32] provides a robust theoretical framework for analyzing the transport properties of materials. Upon the application of an electric field, magnetic field, and temperature gradient, the electric current density j_i can be expressed using conductivity tensors as [32]:

$$j_i = \sigma_{ij} E_j + \sigma_{ijk} E_j B_k + \nu_{ij} \nabla_j T + \cdots \tag{2.104}$$

The group velocity of an electron in band i at wavevector $\mathbf{k}$ is defined as:

$$v_\alpha(i, \mathbf{k}) = \frac{1}{\hbar} \frac{\partial \varepsilon_{i,\mathbf{k}}}{\partial k_\alpha} \tag{2.105}$$

The inverse effective mass tensor is given by the second derivative of the band energy:

$$M^{-1}_{\beta u}(i, \mathbf{k}) = \frac{1}{\hbar^2} \frac{\partial^2 \varepsilon_{i,\mathbf{k}}}{\partial k_\beta \partial k_u} \tag{2.106}$$

Using these definitions, the second-order (electric) conductivity tensor is:

$$\sigma_{\alpha\beta}(i, \mathbf{k}) = e^2 \tau_{i,\mathbf{k}} v_\alpha(i, \mathbf{k}) v_\beta(i, \mathbf{k}) \tag{2.107}$$

The third-order conductivity tensor is expressed using the Levi-Civita symbol $\epsilon_{\gamma uv}$ as:

$$\sigma_{\alpha\beta\gamma}(i, \mathbf{k}) = e^3 \tau^2_{i,\mathbf{k}} \, \epsilon_{\gamma uv} \, v_\alpha(i, \mathbf{k}) v_v(i, \mathbf{k}) M^{-1}_{\beta u}(i, \mathbf{k}) \tag{2.108}$$

These expressions inherently reflect the symmetry properties of the material. For example, in a system with orthorhombic symmetry, $\sigma_{\alpha\beta}$ is a diagonal tensor with three independent components. The tensor $\sigma_{\alpha\beta\gamma}$ is antisymmetric and vanishes unless all indices α, β, and γ are distinct, yielding only three independent components.

Detailed investigations have shown that the directional dependence of τ is often weak [33]. Even in highly anisotropic materials, such as the superconducting cuprates (which exhibit strong variation in conductivity along different crystallographic axes), τ is found to be nearly isotropic [34]. Therefore, in our work, we adopt the commonly used approximation of treating τ as a constant.

In analogy to the density of states,conductivity tensors which depends on energy can be defined from the **k**-dependent conductivity tensors given in Equations. (2.107) and (2.108) is written as:

$$\sigma_{\alpha\beta}(\varepsilon) = \frac{1}{N}\sum_{i,\mathbf{k}} \sigma_{\alpha\beta}(i,\mathbf{k})\,\delta(\varepsilon - \varepsilon_{i,\mathbf{k}}) \tag{2.109}$$

where N denotes the total number of sampled **k**-points. A similar expression holds for the third-order tensor $\sigma_{\alpha\beta\gamma}(\varepsilon)$.

The temperature- and chemical potential-dependent transport tensors can then be calculated from the energy dependent conductivity distributions using the following integrals:

$$\sigma_{\alpha\beta}(T,\mu) = \frac{1}{\Omega}\int \sigma_{\alpha\beta}(\varepsilon)\left(-\frac{\partial f_\mu(T,\varepsilon)}{\partial\varepsilon}\right)d\varepsilon \tag{2.110}$$

$$\nu_{\alpha\beta}(T,\mu) = \frac{1}{eT\Omega}\int \sigma_{\alpha\beta}(\varepsilon)(\varepsilon-\mu)\left(-\frac{\partial f_\mu(T,\varepsilon)}{\partial\varepsilon}\right)d\varepsilon \tag{2.111}$$

$$\kappa^{(0)}_{\alpha\beta}(T,\mu) = \frac{1}{e^2T\Omega}\int \sigma_{\alpha\beta}(\varepsilon)(\varepsilon-\mu)^2\left(-\frac{\partial f_\mu(T,\varepsilon)}{\partial\varepsilon}\right)d\varepsilon \tag{2.112}$$

$$\sigma_{\alpha\beta\gamma}(T,\mu) = \frac{1}{\Omega}\int \sigma_{\alpha\beta\gamma}(\varepsilon)\left(-\frac{\partial f_\mu(T,\varepsilon)}{\partial\varepsilon}\right)d\varepsilon \tag{2.113}$$

Here, μ denotes the chemical potential ,Ω denotes the volume of unit cell, T is the temperature, and $f_\mu(T,\varepsilon)$ is the Fermi-Dirac distribution. where $\kappa^{(0)}$ is the electronic contribution to the thermal conductivity. The Seebeck and Hall coefficients can then be conveniently computed as follows:

The Seebeck coefficient:

$$S_{ij} = \left(\sigma^{-1}\right)_{\alpha i}\,\nu_{\alpha j} \tag{2.114}$$

The Hall coefficient:

$$R_{ijk} = \left(\sigma^{-1}\right)_{\alpha j}\,\sigma_{\alpha\beta k}\,\left(\sigma^{-1}\right)_{i\beta} \tag{2.115}$$

In this study, the relaxation time τ is considered isotropic, which leads to the Seebeck and Hall coefficients being unaffected by the specific value of τ.

Bibliography

[1] G. Kresse and J. Furthmüller. Efficient iterative schemes for ab initio total-energy calculations using a plane-wave basis set. *Phys. Rev. B*, 54:11169–11186, Oct 1996.

[2] G. Kresse and J. Furthmüller. Efficiency of ab-initio total energy calculations for metals and semiconductors using a plane-wave basis set. *Computational Materials Science*, 6(1):15–50, 1996.

[3] Llewellyn H Thomas. The calculation of atomic fields. In *Mathematical proceedings of the Cambridge philosophical society*, volume 23 5, pages 542–548. Cambridge University Press, 1927.

[4] P. Hohenberg and W. Kohn. Inhomogeneous electron gas. *Phys. Rev.*, 136:B864–B871, Nov 1964.

[5] Wolfram Koch and Max C Holthausen. *A chemist's guide to density functional theory.* John Wiley & Sons, 2015.

[6] W. Kohn and L. J. Sham. Self-consistent equations including exchange and correlation effects. *Phys. Rev.*, 140:A1133–A1138, Nov 1965.

[7] W. Kohn. Nobel lecture: Electronic structure of matter—wave functions and density functionals. *Rev. Mod. Phys.*, 71:1253–1266, Oct 1999.

[8] David S Sholl and Janice A Steckel. *Density functional theory: a practical introduction.* John Wiley & Sons, 2022.

[9] Paul AM Dirac. Note on exchange phenomena in the thomas atom. In *Mathematical proceedings of the Cambridge philosophical society*, volume 26, pages 376–385. Cambridge University Press, 1930.

[10] E. Wigner. On the interaction of electrons in metals. *Phys. Rev.*, 46:1002–1011, Dec 1934.

[11] Murray Gell-Mann and Keith A. Brueckner. Correlation energy of an electron gas at high density. *Phys. Rev.*, 106:364–368, Apr 1957.

[12] Seymour H Vosko, Leslie Wilk, and Marwan Nusair. Accurate spin-dependent electron liquid correlation energies for local spin density calculations: a critical analysis. *Canadian Journal of physics*, 58(8):1200–1211, 1980.

[13] J. P. Perdew and Alex Zunger. Self-interaction correction to density-functional approximations for many-electron systems. *Phys. Rev. B*, 23:5048–5079, May 1981.

[14] Lee A. Cole and J. P. Perdew. Calculated electron affinities of the elements. *Phys. Rev. A*, 25:1265–1271, Mar 1982.

[15] John P. Perdew and Yue Wang. Accurate and simple analytic representation of the electron-gas correlation energy. *Phys. Rev. B*, 45:13244–13249, Jun 1992.

[16] Axel D Becke. Density-functional thermochemistry. i. the effect of the exchange-only gradient correction. *The Journal of chemical physics*, 96(3):2155–2160, 1992.

[17] John P. Perdew, Kieron Burke, and Matthias Ernzerhof. Generalized gradient approximation made simple. *Phys. Rev. Lett.*, 77:3865–3868, Oct 1996.

[18] Ks Kim and KD Jordan. Comparison of density functional and mp2 calculations on the water monomer and dimer. *The Journal of Physical Chemistry*, 98(40):10089–10094, 1994.

[19] Efthimios Kaxiras. *Atomic and electronic structure of solids*. 2003.

[20] D. R. Hamann, M. Schlüter, and C. Chiang. Norm-conserving pseudopotentials. *Phys. Rev. Lett.*, 43:1494–1497, Nov 1979.

[21] P. E. Blöchl. Projector augmented-wave method. *Phys. Rev. B*, 50:17953–17979, Dec 1994.

[22] G. Kresse and D. Joubert. From ultrasoft pseudopotentials to the projector augmented-wave method. *Phys. Rev. B*, 59:1758–1775, Jan 1999.

[23] O. K. Andersen and R. V. Kasowski. Electronic states as linear combinations of muffin-tin orbitals. *Phys. Rev. B*, 4:1064–1069, Aug 1971.

[24] F. Bl¨och. *Z. Physik 52, 555*, 1928.

[25] J. C. Slater and G. F. Koster. Simplified lcao method for the periodic potential problem. *Phys. Rev.*, 94:1498–1524, Jun 1954.

[26] Gregory H. Wannier. The structure of electronic excitation levels in insulating crystals. *Phys. Rev.*, 52:191–197, Aug 1937.

[27] Nicola Marzari and David Vanderbilt. Maximally localized generalized wannier functions for composite energy bands. *Phys. Rev. B*, 56:12847–12865, Nov 1997.

[28] Ivo Souza, Nicola Marzari, and David Vanderbilt. Maximally localized wannier functions for entangled energy bands. *Phys. Rev. B*, 65:035109, Dec 2001.

[29] John Stanley Griffith. *The theory of transition-metal ions*. Cambridge university press, 1961.

[30] Sishir Kumar Pandey. Microscopic model for spin, orbital and charge ordering in transition metal compounds. *Thesis*, 2017.

[31] P Allen. Boltzmann theory and resistivity of metals. *Kluwer International Series In Engineering And Computer Science*, pages 219–250, 1996.

[32] Georg K.H. Madsen and David J. Singh. Boltztrap. a code for calculating band-structure dependent quantities. *Computer Physics Communications*, 175(1):67–71, 2006.

[33] Werner W. Schulz, Philip B. Allen, and Nandini Trivedi. Hall coefficient of cubic metals. *Phys. Rev. B*, 45:10886–10890, May 1992.

[34] Philip B. Allen, Warren E. Pickett, and Henry Krakauer. Anisotropic normal-state transport properties predicted and analyzed for high-T_c oxide superconductors. *Phys. Rev. B*, 37:7482–7490, May 1988.

Chapter 3

Perturbing the Bond Disproportionated State in $NdNiO_3$

3.1 Introduction

Transition-metal oxide perovskites (ABO_3), in which the transition metal occupies the B site of the perovskite structure, exhibit a diverse range of physical properties, including ferroelectricity, magnetism, octahedral rotations, and superconductivity. Among these materials, rare-earth nickelates(RE = Nd,Sm,Pr .. Lu, etc.) [1–3] have gained significant interest due to their intriguing metal-insulator transition (MIT). While the metal-insulator transition in transition metal compounds has been extensively studied, its fundamental mechanism remains a topic of debate. Despite numerous theoretical explanations, a comprehensive understanding has yet to be established. Early transition metal oxides are typically insulating due to strong electronic correlations (U) [4] at the transition metal site, the band gap scales proportionally with the strength of the on-site Coulomb interaction U. In contrast, late transition metal compounds exhibit a metal-insulator transition primarily influenced by charge transfer energy. When p-bands of oxygen atom overlap with d-bands of the metal, the charge transfer energy becomes negative, leading to metallic behavior. This phenomenon is well explained by the Zaanen-Sawatzky-Allen (ZSA) phase diagram [4]. However, in certain cases, robust hybridization between the transition metal d and ligand oxygen p orbitals leads to the formation of bonding and antibonding states, thereby opening a band gap. This effect was later integrated into an extended version of the ZSA phase diagram [5]. Rare-earth nickelates fall within the negative charge-transfer energy regime [5, 6] and exhibit a temperature-dependent metal-insulator transition [2]. However their insulating state is different from what has been discussed in the ZSA phase diagram [4]. Here, the transition to an insulating state in these materials is accompanied by structural distortions of the Ni–O octahedra, specifically the "breathing mode distortion" [4, 7–10]. This distortion results in the alternating lengths of long and short Ni-O bonds, creating two distinct octahedral environments for Ni atoms. In this configuration, one site, characterized by longer Ni–O bonds, adopts a Ni^{2+} (d^8, $S = 1$) state, while the other, with shorter Ni–O bonds, corresponds to Ni^{4+} (d^8L^2, $S = 0$), where L represents a ligand hole. This phenomenon, referred to as bond disproportionation (BD), differs

from conventional charge disproportionation (CD) because there is no substantial charge imbalance between the two Ni site [7, 8].

Although substantial research has been conducted on undoped nickelates, various strategies can be employed to perturb the bond-disproportionated (BD) state and thereby modulate the metal-insulator transition (MIT). One such method is carrier doping. Unlike conventional semiconductors, transition metal oxides retain their insulating behavior even at relatively high doping concentrations of 10-20% [11, 12]. In some cases, the doped holes become localized, leading to polaronic distortions or charge ordering. For nickelate superlattices, such localized states have also been observed.

Experimental studies on hole and electron doping in both bulk and thin films of $NdNiO_3$ and $SmNiO_3$ have already been conducted. These observations revealed a reduction in the metal to insulator transition temperature for doping levels as low as 10% [13, 14], and the emergence of a metallic state at doping levels around 30% [15]. However, no single mechanism can be definitively attributed to the preservation of the insulating state despite hole or electron doping. In this work,[1] we consider hole and electron-doped nickelates that possess a bond-disproportionated state in the Intrinsic limit and examine the effect of carrier doping by performing DFT+U calculations across different doping levels. Unlike conventional semiconductors, where doping typically induces metallicity, the added holes or electrons in nickelates localize on a few Ni atoms, which are randomly distributed, while the rest of the lattice maintains the bond-disproportionated state. So in that case, a hole or an electron is uniformly distributed all over the lattice, introducing a very small change in the charge transfer energy Δ, which is not giving enough driving force to annihilate the bond-disproportionated state. Consequently, the majority of the lattice continues to exhibit the bond-disproportionated state.

While we have theoretically analyzed the localization of holes and electrons, the experimental realization of this phenomenon remains unexplored. Although Murray-Ara et al. [17] proposed using synchrotron X-ray diffraction to detect the alternating pattern of Mn atoms for an ordered charge-ordered manganite via their anomalous dispersion, based on anisotropic tensor susceptibility (ATS) reflection measurements near the Mn K-absorption edge. In the case of carrier doping, holes or electrons may be randomly distributed and so the ATS reflection measurements will not work. In such cases, the distribution can be detected through the 1s to 4p transition at the transition metal K-edges using X-ray absorption spectroscopy. Theoretically, this phenomenon can be simulated by observing a strong energy dependence resulting from the splitting in the density of states (DOS) of the transition metal 4p orbitals at distinct sites. We propose that this

[1] chapter 3 is based on publication [16]

experiment can validate that the bond-disproportionated state is not destroyed for small doping, and the doped electron or hole is localized on the Ni site.

3.2 Methodology

First-principles calculations were done by the density functional theory (DFT) formalism using the Vienna *Ab-initio* Simulation Package (VASP). The orthorhombic perovskite structure of $NdNiO_3$, with space group *Pbnm*, was adopted based on experimental data [18]. To incorporate magnetic effects, a non-collinear E'-type antiferromagnetic (E'-AFM) ordering was imposed on the Ni sublattice, consistent with previous studies [19]. As illustrated in Fig. 3.1, this configuration features neighboring spins of equal magnitude arranged orthogonally (i.e., with 90° relative orientation). Hole doping was modeled by substituting Nd^{3+} with Ca^{2+} in a 160-atom supercell of size $2\sqrt{2} \times 2\sqrt{2} \times 2$, corresponding to Ca concentrations of 3.125%, 6.25%, and 9.375%. Each Ca substitution introduces one hole. Electron doping was similarly simulated by replacing Nd^{3+} with Ce^{4+}, thereby adding extra electrons. The electronic structure was obtained by the projector augmented-wave (PAW) method [20] applied in VASP [21, 22], with the exchange-correlation effects under the the generalized gradient approximation (GGA) [23]. On-site Coulomb interactions for Ni d electrons were included using the GGA+U approach within the Dudarev formalism [24], employing a U value of 4 eV. While the lattice constants were held fixed at values obtained by experiments. Atomic positions were relaxed until forces were smaller than 10^{-3} eV/Å. Integration over Brillouin zone was performed using a $2 \times 2 \times 1$ Monkhorst-Pack k-point grid [25], and the plane-wave basis was truncated at an energy cutoff of 400 eV. Magnetic moments and the density of states (DOS) were evaluated by integrating within spheres of 1 Å radius centered on each atom, approximately half the Ni-O bond length. Doping-induced changes in the electrostatic potential, denoted as Δ, were obtained by monitoring the site-resolved potentials at Ni and O sites.

3.3 Result and Discussion

We began our analysis with DFT+U calculations for undoped $NdNiO_3$. In our optimized E'-AFM structure, we observed two distinct Ni-O octahedral environments, consistent with previous studies. The Ni atom with a longer Ni-O bond length (approximately 2 Å) is mimicked as Ni^{2+}, while the Ni atom with a shorter Ni-O bond length (around 1.9 Å) is mimicked as Ni^{4+}. Although there is no significant charge difference between the

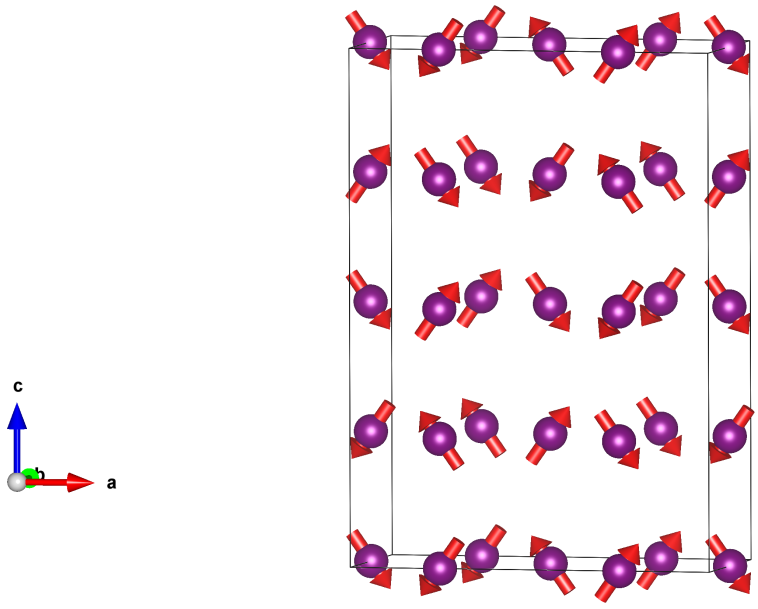

Figure 3.1: Experimental E'-type antiferromagnetic (AFM) structure, where neighboring spins are aligned perpendicular to each other.

two Ni atoms, the electronic structure suggests distinct behaviors for them. The spin-resolved density of states, calculated using DFT+U for undoped $NdNiO_3$, is shown in Fig. 3.2. Here, Fig. 3.2 a and Fig. 3.2 b present the density of states for Ni^{2+} and Ni^{4+}, respectively. This analysis clearly illustrates the effective electronic configurations of the two types of Ni atoms. For Ni^{2+}, the t_{2g} states are fully occupied in both the majority and minority spin projections, while the e_g states are occupied only in the majority spin projection. In contrast, for Ni^{4+}, the t_{2g} states remain occupied in both spin channels, whereas the e_g states are completely unoccupied. These two different Ni sites can also be distinguished by their magnetic moments. Ni^{2+} has a magnetic moment of nearly 1.5 μ_B, while the magnetic moment of Ni^{4+} is 0 μ_B.

We have examined the robustness of the bond-ordered state under carrier doping. We first examined the case of hole doping. To introduce hole doping, we substituted Ca atoms in place of Nd atoms. We performed DFT+U calculations taking into account the E'-AFM configuration for doping concentrations of 0%, 3.125%, 6.25%, and 9.375%. The doped system exhibited insulating behavior in all cases. Since DFT calculations do not accurately capture the relative stability of different magnetic configurations in the undoped limit, we did not attempt to determine the crossover point from the insulating to the metallic state in our study. Whether the bond disproportionation state survives upon hole doping can be inferred by examining the structural changes of the system. The trends in these structural changes are well captured and form the foundation of our examination

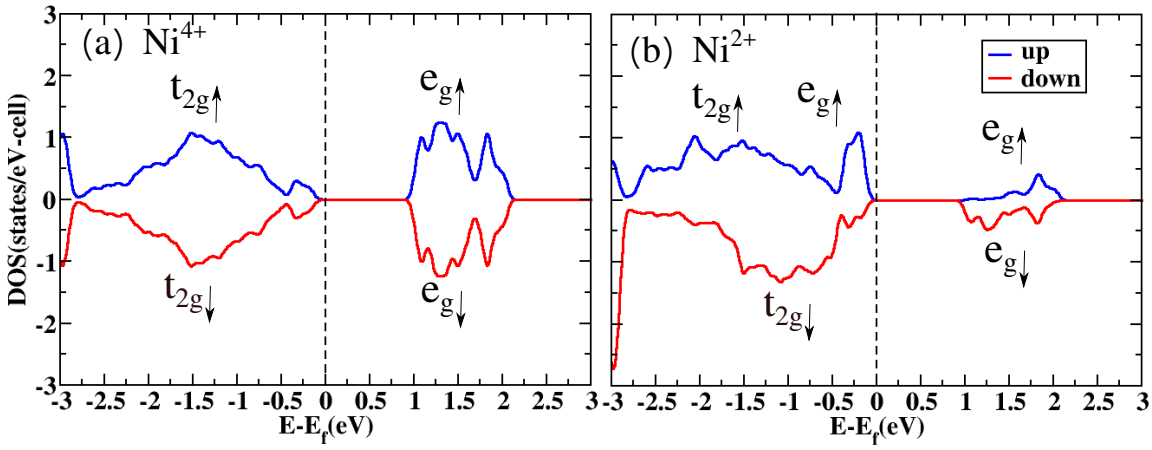

Figure 3.2: Spin resolved density of states of (a) Ni^{4+} (b) Ni^{2+} d orbital for the undoped case.

of the structural and electronic properties. At a concentration of 3.125% doping, we observed that structural distortions (as shown in Fig.3.3 a) around different Ni atoms lead to the formation of three inequivalent Ni sites. These sites are distinguished by the Ni-O bond lengths of the NiO_6 octahedra. Ni^{2+} sites have six long Ni-O bonds, with bond lengths close to 2.0 Å, whereas Ni^{4+} sites exhibit six short Ni-O bonds, approximately 1.9 Å in length.

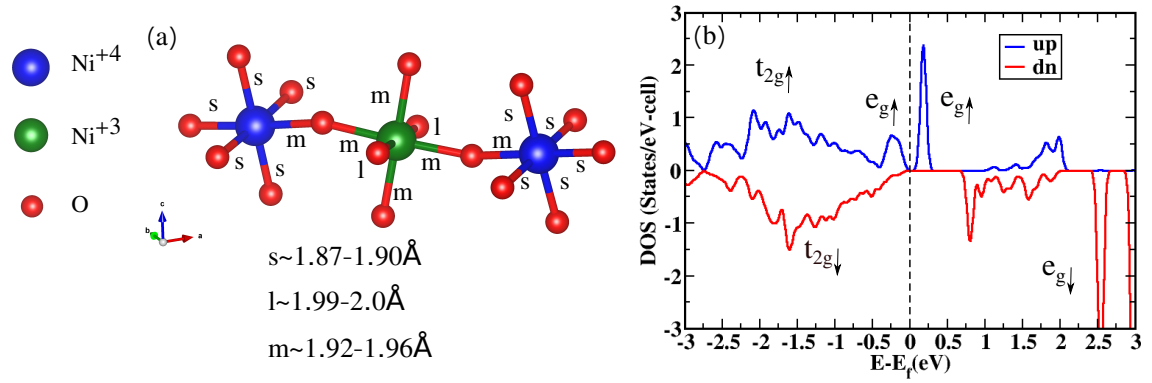

Figure 3.3: Structural and electronic changes due to hole doping. (a) Structural changes around the Ni^{2+} atom induced by hole doping. (b) Spin-resolved density of states of the Ni^{3+} atom

.

Additionally, a second type of Ni site, identified as Ni^{3+}, is characterized by Ni–O bond lengths that exhibit a mixture of short and long bonds. The different Ni atoms were distinguished based on the average bond length within the NiO_6 octahedra. The average Ni–O bond lengths within each octahedron are summarized in Table 3.1, showing that the Ni^{3+}–O octahedra have an intermediate bond length compared to the other two types. A closer inspection reveals that some of the Ni^{2+} sites near the Ca dopants

transform into Ni^{3+} sites, accompanied by a separation of the majority spin of e_g states. This electronic change is associated with an additional structural distortion, where four of the Ni–O bonds in the Ni^{3+} octahedra become shorter compared to those in the Ni^{2+} sites (see Fig. 3.3 a). The neighboring Ni^{4+} sites also exhibit corresponding changes in their bond lengths to accommodate these distortions. Due to the oxygen displacements around the Ni^{3+} sites, the original degeneracy of majority spin e_g orbitals are lifted, with the $d_{x^2-y^2}$ orbital shifting to a higher energy than the $d_{3z^2-r^2}$ orbital. As a result, a split-off state arises just above the Fermi energy, maintaining the insulating character of the system (see Fig. 3.3 b). Similar to the undoped case, the sites designated as Ni^{2+}, Ni^{3+}, and Ni^{4+} possess identical formal charges and are primarily distinguished by their magnetic moments (1.5 μ_B for Ni^{2+}, 0.98 μ_B for Ni^{3+}, and 0 μ_B for Ni^{4+}).

Table 3.1: Average Ni–O bond lengths (Å) in a given Ni–O octahedron for different Ni oxidation states under hole and electron doping.

Type of Ni-O octahedra	**Bond length (Å)**	
	Hole doping	**Electron Doping**
Ni^{2+}–O	2.0	2.0
Ni^{3+}–O	1.96	1.93
Ni^{4+}–O	1.9	1.9

A key question is why the bond disproportionated state is not destroyed under doping. To address this, we consider the charge transfer energy, which has been identified as a parameter that demarcates the bond-disproportionated state in the undoped limit. Hole localization alters the effective valency of Ni^{2+} atoms, effectively raising it to +3. This increase in valency is driven by changes in the bond length with neighboring oxygen atoms, which in turn modifies the hybridization between the ligand hole and the valence electrons of the Ni atom. As the effective valency increases, the Ni^{3+} ion experiences a stronger attraction between its valence electrons and the core, pushing the bare energy levels of the *d*-electrons to deeper (lower) energies. Consequently, the charge transfer energy is expected to decrease in this system. As the dominant contribution to the change in onsite energy at the Ni^{3+} is from the additional hole, we quantify this effect by examining the electrostatic potential variations. This is calculated by placing a unit charge within a sphere of 1 Å on each Ni site. The variations in electrostatic potential at Ni^{3+} sites relative to Ni^{2+} ones and Ni^{4+} ones are presented in Table 3.2. The bond-disproportionated state exists within a specific range of charge transfer energy, as shown in Ref. [26]. To destabilize the bond disproportionated state, the charge transfer energy must shift out of this regime. Under doping, the change in electrostatic potential at the

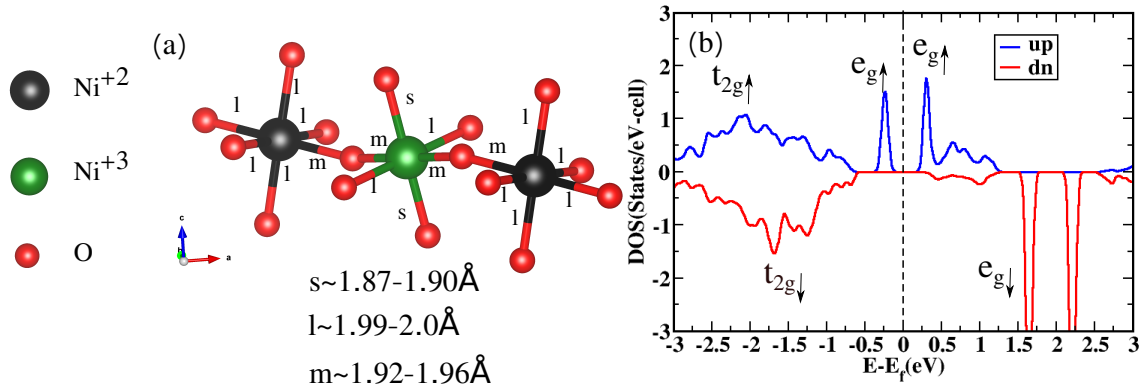

Figure 3.4: Structural and electronic changes due to electron doping. (a) Structural changes around the Ni^{2+} atom induced by electron doping. (b) Spin-resolved density of states of the Ni^{3+} atom

specific Ni atom is found to be positive relative to the Ni^{4+} site and negative relative to the Ni^{2+} site. This indicates that the Δ value at the Ni^{3+} site lies between those of Ni^{2+} and Ni^{4+}. Therefore, the effective change Δ remains within the negative regime where the bond disproportionated state persists. We also performed a similar analysis for electron doping by substituting Nd atoms with Ce atoms at the same doping levels. This also results in an insulating state for all cases. Similar to the hole-doping case, we did not attempt to identify the crossover point from metallic to insulating behavior for electron doping. In this case, the additional electron is localized at the Ni^{4+} site.

Table 3.2: Change in electrostatic potential of the Ni atom where the hole or electron is localized.

Change in Electrostatic Potential	**Hole doping**	**Electron doping**
$E_{Ni^{+3}} - E_{Ni^{+2}}$(eV)	-0.37	-0.39
$E_{Ni^{+3}} - E_{Ni^{+4}}$(eV)	0.34	0.36

This localization can be observed through changes in both the structural and electronic properties of a specific Ni atom, which we denote as Ni^{3+}. For a Ni^{4+} atom, the t_{2g} states are fully occupied, and both spin channels of the e_g orbital are unoccupied, resulting in a zero magnetic moment. The additional electron localizes in the unoccupied up-spin channel of the e_g orbital. This localization is accompanied by further distortion of the Ni–O bond lengths at the Ni^{4+} site. The corresponding changes in bond lengths are shown in Fig. 3.4 a. The out-of-plane bond lengths remain nearly unchanged at approximately 1.9 Å, whereas the in-plane bond lengths exhibit a mixed character. As a result, the e_g orbitals split, and the additional electron now occupies the majority spin channel of the e_g state just below the Fermi energy, as shown in the spin-resolved density of states in Fig. 3.4 b.

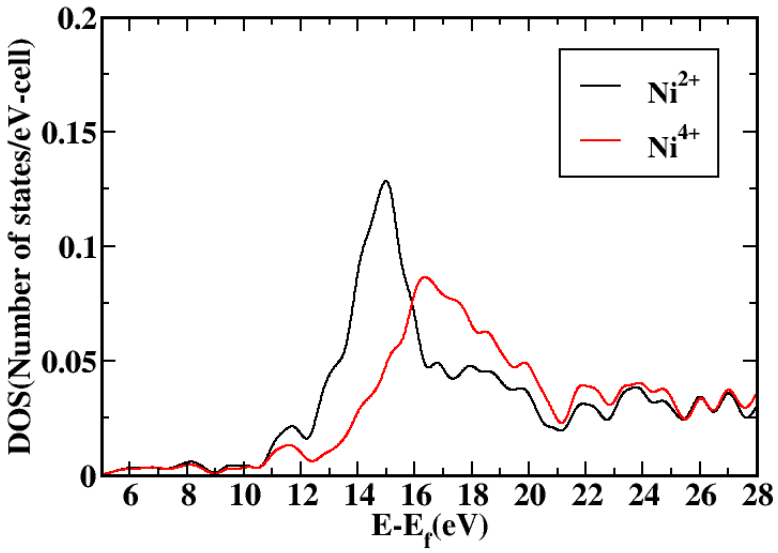

Figure 3.5: Comparison of the density of states for the unoccupied 4p orbital of (a) Ni^{4+} and (b) Ni^{2+} atoms.

Due to the exchange splitting, the spin channels are no longer degenerate, leading to a finite magnetic moment of nearly 1.0 μ_B. To analyze the change in charge transfer energy, we follow the same procedure as in the hole-doping case. By examining the change in electrostatic potential at the Ni^{3+} site relative to the Ni^{2+} and Ni^{4+} sites, we find that it exhibits characteristics intermediate between the two Ni sites. This supports the conclusion that the system remains within the negative Δ regime of the bond-disproportionated state. Furthermore, we are investigating experimental methods to probe the three types of Ni atoms. In Fig. 3.5, the density of states (DOS) for the undoped Ni^{2+} and Ni^{4+} $4p$ orbitals are presented. The $4p$ states of Ni^{2+} appear at lower energies compared to those of Ni^{4+}, with a separation of approximately 1.32 eV. Therefore, when Ni^{2+} and Ni^{4+} are arranged in an ordered manner, one can distinguish different bond ordered states by their shift in Ni 4p states. This shift can be easily detected using synchrotron X-ray diffraction based on anisotropic tensor susceptibility (ATS) reflection measurements near the Ni K-absorption edge. However, in the case of carrier doping, holes and electrons are randomly distributed throughout the lattice, making this method ineffective. In such cases, the doped holes or electrons further modify the electronic structure of the Ni atoms. To identify the hole or electron localized Ni^{3+} atoms, we compared the energy shifts of the Ni^{3+} $4p$ states relative to Ni^{2+} under hole doping and to Ni^{4+} under electron doping. In the case of hole doping, the Ni^{3+} $4p$ states shift to higher energy (rightward) relative to the Ni^{2+} states by approximately 0.34 eV, resulting in a distinct feature within the

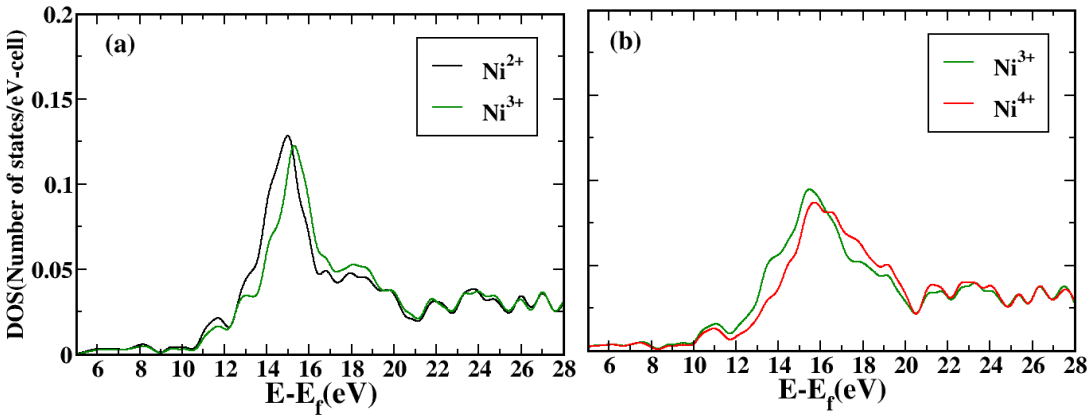

Figure 3.6: Comparison of the density of states (DOS) of the carrier-localized Ni^{3+} orbital with that of (a) unperturbed Ni^{2+} under hole doping and (b) Ni^{4+} under electron doping.

Ni^{2+} $4p$ states (see Fig. 3.6 a). Conversely, under electron doping, the Ni^{3+} $4p$ states shift to lower energy (leftward) relative to Ni^{4+} by about 0.26 eV (see Fig. 3.6 b). Therefore, we propose that the localization of holes or electrons can be detected by identifying this additional feature at the Ni K edge using X-ray absorption spectroscopy.

3.4 Conclusion

We have explored the electronic and structural properties of $NdNiO_3$ under Ca and Ce doping using DFT calculations at varying concentrations. Our results show that substituting Nd with Ca or Ce introduces holes or electrons into the system, respectively. These carriers are not uniformly distributed across the lattice. Rather, they localize on specific Ni atoms, altering their electronic configuration and inducing additional bond-length distortions. Additionally, this carrier doping modifies the parameter Δ, which characterizes the bond disproportionation tendency. Since the bond disproportionation phase emerges within a certain range of negative Δ values, both increasing and decreasing Δ can destabilize the bond disproportionated state. Remarkably, our DFT results reveal that the variation of Δ relative to the undoped system is site-dependent among the Ni atoms. Under the localization of holes or electrons on a specific Ni atom, the change in Δ for that atom remains within the specific range where bond disproportionation occurs. As a result, rather than fully suppressing the bond disproportionated state at low doping levels, certain Ni^{2+} and Ni^{4+} sites transition into Ni^{3+}. This behavior may be attributed to the high strain energy cost required to break the bond disproportionated state, as well as the significant exchange splitting at the Ni^{+2} sites. Furthermore, examining the

unoccupied Ni $4p$ state serves as a useful probe for identifying not only the Ni^{2+} and Ni^{4+} states, but also the Ni^{3+} state induced by hole or electron doping.

Bibliography

[1] S. Middey, J. Chakhalian, P. Mahadevan, J.W. Freeland, A.J. Millis, and D.D. Sarma. Physics of ultrathin films and heterostructures of rare-earth nickelates. *Annual Review of Materials Research*, 46(Volume 46, 2016):305–334, 2016.

[2] G. Catalan. Progress in perovskite nickelate research. *Phase Transitions*, 81(7-8):729–749, Jul 2008.

[3] María Luisa Medarde. Structural, magnetic and electronic properties of $RNiO_3$ perovskites (R = rare earth). *Journal of Physics: Condensed Matter*, 9(8):1679, Feb 1997.

[4] J. Zaanen, G. A. Sawatzky, and J. W. Allen. Band gaps and electronic structure of transition-metal compounds. *Phys. Rev. Lett.*, 55:418–421, Jul 1985.

[5] S. R. Barman, A. Chainani, and D. D. Sarma. Covalency-driven unusual metal-insulator transition in nickelates. *Phys. Rev. B*, 49:8475–8478, Mar 1994.

[6] Valentina Bisogni, Sara Catalano, Robert J. Green, Marta Gibert, Raoul Scherwitzl, Yaobo Huang, Vladimir N. Strocov, Pavlo Zubko, Shadi Balandeh, Jean-Marc Triscone, George Sawatzky, and Thorsten Schmitt. Ground-state oxygen holes and the metal–insulator transition in the negative charge-transfer rare-earth nickelates. *Nature Communications*, 7(1):13017, Oct 2016.

[7] T. Mizokawa, D. I. Khomskii, and G. A. Sawatzky. Spin and charge ordering in self-doped mott insulators. *Phys. Rev. B*, 61:11263–11266, May 2000.

[8] Hyowon Park, Andrew J. Millis, and Chris A. Marianetti. Site-selective mott transition in rare-earth-element nickelates. *Phys. Rev. Lett.*, 109:156402, Oct 2012.

[9] Steve Johnston, Anamitra Mukherjee, Ilya Elfimov, Mona Berciu, and George A. Sawatzky. Charge disproportionation without charge transfer in the rare-earth-element nickelates as a possible mechanism for the metal-insulator transition. *Phys. Rev. Lett.*, 112:106404, Mar 2014.

[10] R. J. Green, M. W. Haverkort, and G. A. Sawatzky. Bond disproportionation and dynamical charge fluctuations in the perovskite rare-earth nickelates. *Phys. Rev. B*, 94:195127, Nov 2016.

[11] A. Chainani, M. Mathew, and D. D. Sarma. Electron-spectroscopy study of the semiconductor-metal transition in $la_{1-x}sr_xcoo_3$. *Phys. Rev. B*, 46:9976–9983, Oct 1992.

[12] T. Katsufuji, Y. Taguchi, and Y. Tokura. Transport and magnetic properties of a mott-hubbard system whose bandwidth and band filling are both controllable: $R_{1-x}Ca_xTiO_{3+y/2}$. *Phys. Rev. B*, 56:10145–10153, Oct 1997.

[13] J. L. García-Muñoz, M. Suaaidi, M. J. Martínez-Lope, and J. A. Alonso. Influence of carrier injection on the metal-insulator transition in electron- and hole-doped $R_{1-x}A_xNiO_3$ perovskites. *Phys. Rev. B*, 52:13563–13569, Nov 1995.

[14] I. Vobornik, L. Perfetti, M. Zacchigna, M. Grioni, G. Margaritondo, J. Mesot, M. Medarde, and P. Lacorre. Electronic-structure evolution through the metal-insulator transition in $RNiO_3$. *Phys. Rev. B*, 60:R8426–R8429, Sep 1999.

[15] Shengwei Zeng, Chi Sin Tang, Xinmao Yin, Changjian Li, Mengsha Li, Zhen Huang, Junxiong Hu, Wei Liu, Ganesh Ji Omar, Hariom Jani, Zhi Shiuh Lim, Kun Han, Dongyang Wan, Ping Yang, Stephen John Pennycook, Andrew T. S. Wee, and Ariando Ariando. Phase diagram and superconducting dome of infinite-layer $Nd_{1-x}Sr_xNiO_2$ thin films. *Phys. Rev. Lett.*, 125:147003, Oct 2020.

[16] Ranjan Kumar Patel, Krishnendu Patra, Shashank Kumar Ojha, Siddharth Kumar, Sagar Sarkar, Akash Saha, Nandana Bhattacharya, John W. Freeland, Jong-Woo Kim, Philip J. Ryan, Priya Mahadevan, and Srimanta Middey. Hole doping in a negative charge transfer insulator. *Communications Physics*, 5(1):216, Aug 2022.

[17] Y. Murakami, H. Kawada, H. Kawata, M. Tanaka, T. Arima, Y. Moritomo, and Y. Tokura. Direct observation of charge and orbital ordering in $La_{0.5}Sr_{1.5}MnO_4$. *Phys. Rev. Lett.*, 80:1932–1935, Mar 1998.

[18] J. L. García-Muñoz, M. A. G. Aranda, J. A. Alonso, and M. J. Martínez-Lope. Structure and charge order in the antiferromagnetic band-insulating phase of $NdNiO_3$. *Phys. Rev. B*, 79:134432, Apr 2009.

[19] V. Scagnoli, U. Staub, A. M. Mulders, M. Janousch, G. I. Meijer, G. Hammerl, J. M. Tonnerre, and N. Stojic. Role of magnetic and orbital ordering at the metal-insulator transition in $NdNiO_3$. *Phys. Rev. B*, 73:100409, Mar 2006.

[20] P. E. Blöchl. Projector augmented-wave method. *Phys. Rev. B*, 50:17953–17979, Dec 1994.

[21] G. Kresse and J. Hafner. Ab initio molecular dynamics for liquid metals. *Phys. Rev. B*, 47:558–561, Jan 1993.

[22] G. Kresse and J. Furthmüller. Efficient iterative schemes for ab initio total-energy calculations using a plane-wave basis set. *Phys. Rev. B*, 54:11169–11186, Oct 1996.

[23] John P. Perdew, Kieron Burke, and Matthias Ernzerhof. Generalized gradient approximation made simple. *Phys. Rev. Lett.*, 77:3865–3868, Oct 1996.

[24] S. L. Dudarev, G. A. Botton, S. Y. Savrasov, C. J. Humphreys, and A. P. Sutton. Electron-energy-loss spectra and the structural stability of nickel oxide: An lsda+u study. *Phys. Rev. B*, 57:1505–1509, Jan 1998.

[25] Hendrik J. Monkhorst and James D. Pack. Special points for brillouin-zone integrations. *Phys. Rev. B*, 13:5188–5192, Jun 1976.

[26] Basudeb Mandal, Sagar Sarkar, Shishir Kumar Pandey, Priya Mahadevan, Cesare Franchini, A. J. Millis, and D. D. Sarma. The driving force for charge ordering in rare earth nickelates, 2017.

Chapter 4

Disorder controlled ↑↑↓↓ magnetic ordering stability in the Ising chain magnet Ca_3CoMnO_6

4.1 Introduction

Type-II multiferroics, in which ferroelectricity is induced by magnetic ordering, have drawn considerable attention in recent years due to their pronounced magnetoelectric coupling [1, 2]. Typically, the local inversion symmetry required for long-range ferroelectricity is broken by non-collinear magnetic structures, often arising from strong spin-orbit coupling or inverse Dzyaloshinskii-Moriya (DM) interactions [3,4]. However, ferroelectricity driven by collinear magnetism is rare. One such example is the Ising chain magnet $Ca_3Co_{2-x}Mn_xO_6$, where ferroelectricity emerges below the magnetic ordering temperature (around 13 K) due to exchange striction from a collinear up-up-down-down (↑↑↓↓) spin arrangement among adjacent transition metal ions [5–7]. In the case of Ca_3CoMnO_6 ($x = 1$),the structure features alternating chains of face-sharing $Co^{2+}O_6$ trigonal prisms and $Mn^{4+}O_6$ octahedra aligned along the c-axis. Interestingly, the collinear ↑↑↓↓ magnetic ordering is stabilized not at $x = 1$, but at slightly off-stoichiometric compositions ($x = 0.95$ or 1.05). Such a phenomenon has been referred to as 'order-by-static-disorder,' [8] where magnetic ordering is stabilized due to cationic disorder, specifically, Co occupying octahedral sites ($x < 1$) or Mn occupying trigonal prismatic sites ($x > 1$) (that is, away from perfectly ordered compounds), indicating the importance of Co or Mn excess for stabilizing this spin arrangement. It is also interesting to note that recent studies have shown that Mn deficiency (i.e., $Ca_3CoMn_{1-x}O_6$) can enhance the ferroelectric transition temperature up to ∼30 K in such Ising chain magnets [9]. Similar behavior has been observed for $x \approx 0.26$ and $x \approx 0.72$ in $Ca_3Co_{2-x}Mn_xO_6$, which was attributed to purely structural effects, specifically local Jahn-Teller distortion of Co^{2+} ($3d^7$) ions in the trigonal prismatic environment [10]. Surprisingly, such enhancements were absent in the stoichiometric $x \approx 1$ single-crystal compound, despite a significant presence of Co^{2+} in the trigonal prismatic sites [11]. It is well known that the first-order Jahn-Teller effects tend to destabilize ferroelectricity. These observations suggest that not only magnetic ordering but also ferroelectricity is strongly influenced by cationic Co-Mn disorder. However,

the specific role of such cationic disorder in the $x \approx 1$ (Ca_3CoMnO_6) compound remains unexplored in the literature. Investigating this could help unravel the unusual magnetic and ferroelectric behavior observed in different x members of this family of Ising chain magnets. It was argued that the strong magnetic frustration arising from various competing nearest and next-nearest intra and inter chain interactions [8] at $x \approx 1$ was primarily responsible for the significant suppression of the characteristic ↑↑↓↓ magnetic ordering. However, this ordering was recovered in $Ca_3Co_{2-x}Mn_xO_6$ compounds with reduced magnetic frustration, either in Co-rich ($x = 0.95$) or Co-poor ($x = 1.05$) compositions [8]. From a theoretical standpoint, density functional theory (DFT) calculations have yielded predictions regarding the magnetic ground state of the $x = 1$ composition with the choice of exchange correlation functional finding either the ↑↓↑↓ or ↑↑↓↓ configuration to be energetically favorable [6, 12]. In this chapter [1] we have systematically shown that we can stabilize the up-up-down-down magnetic configuration of Ca_3CoMnO_6 even near $x \approx 1$ with varying levels of cation (Co/Mn) positional disorder. Our results indicate that in a perfectly ordered structure, the ↑↓↑↓ configuration is energetically more stable than the ↑↑↓↓ one. However, introducing a small amount of positional disorder (∼7%)where Co and Mn partially occupy each other's preferred lattice sites leads to Co atoms having another Co atom as its nearest neighbor, and similarly, Mn atoms could have another Mn atom as their nearest neighbor. This favors the stabilization of the ↑↑↓↓ spin order. Furthermore, as the level of disorder increases (up to ∼15%), the energy difference between the two magnetic configurations diminishes to within the margin of computational error, suggesting that the ↑↑↓↓ state becomes realizable even in stoichiometric Ca_3CoMnO_6 with a small amount of antisite disorder. However, a higher degree of disorder eventually destabilizes this collinear magnetic configuration again.

4.2 Methodology

We carried out electronic structure computations based on density functional theory (DFT) using the projector augmented-wave (PAW) method, as implemented in the Vienna *ab-initio* Simulation Package (VASP) [13–16]. The exchange-correlation functional was considered within the framework of the generalized gradient approximation (GGA) [17]. Electron-electron interaction effects were incorporated for the d-orbitals of both Mn and Co atoms using the GGA+U method proposed by Dudarev [18], with $U = 3$ eV for Mn and $U = 6$ eV for Co [6].

[1] chapter 4 is based on publication number 4 in the publication list

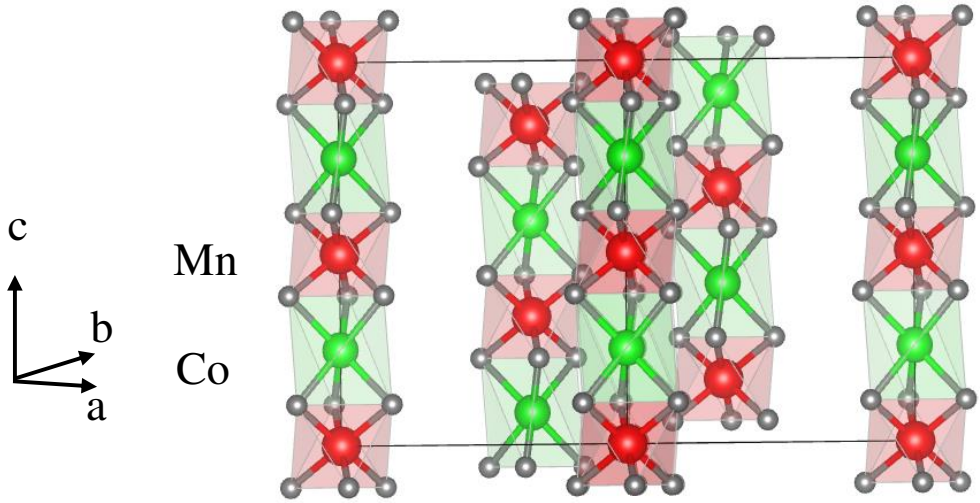

Figure 4.1: Rhombohedral crystal structure in its hexagonal setting.

We adopted the experimentally determined rhombohedral crystal structure [19](space group $R\bar{3}c$) in its hexagonal setting as shown in Fig 1. For computational convenience, we extracted the trigonal primitive cell, which contains a single Co-Mn chain. For the ordered structure, a plane-wave cutoff energy of 600 eV was used, along with a Monkhorst-Pack $6 \times 6 \times 6$ k-point grid for Brillouin zone integration. [20] To model disorder, supercells of size $1 \times 1 \times 2$, $1 \times 1 \times 3$, $1 \times 1 \times 5$, and $2 \times 2 \times 2$ were constructed by interchanging Co and Mn atomic positions to represent various degrees of site disorder. For each case, atomic positions were optimized for both $\uparrow\downarrow\uparrow\downarrow$ and $\uparrow\uparrow\downarrow\downarrow$ magnetic configurations using the same U values. To investigate the exchange pathways, we employed maximally localized Wannier functions via the Wannier90-VASP [21] interface. This yielded a good fit, allowing us to extract both on-site energies and hopping interaction strengths from the complete Hamiltonian. The energy gain from each hopping pathway was then determined by computing the total energy by integrating the occupied eigen values within the tight-binding model, both with and without the relevant Hamiltonian matrix elements corresponding to the hopping pathway.

4.3 Results and discussions

We attempted to understand the source of stabilization for the up-up-down-down ($\uparrow\uparrow\downarrow\downarrow$) magnetic ground state in the presence of disorder through GGA+U calculations. To investigate the stability of the up-up-down-down structure, it is necessary to understand the true ground state in the ordered limit.

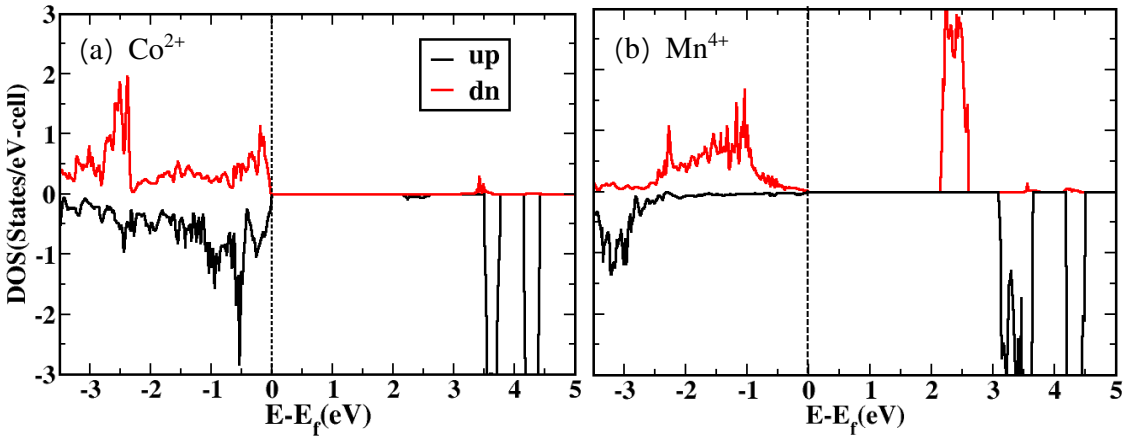

Figure 4.2: The density of states (DOS) of the d orbitals with spin-projection for (a) Co^{2+} and (b) Mn^{4+}. Here, E_F denotes the Fermi energy.

For this purpose, we have taken four possible collinear magnetic orders (↑↓↑↓, ↑↑↓↓, ↑↓↓↓, and ↑↑↑↑) in the Co-Mn-Co-Mn chains for the ordered structure. We have optimized the atomic positions of four magnetic structures with our GGA+U calculations and the total energy of each configuration revealed that the ↑↓↑↓ and ↑↑↓↓ states are two competing ground states, with ↑↓↑↓ having 5 meV/f.u. less energy than ↑↑↓↓. In both converged structures obtained from our DFT calculations, all Mn-O bond lengths are the same (nearly 1.92 Å), whereas the Co-O bond lengths vary from 2.11 Å to 2.17 Å. The Co-Mn bond distances for the ↑↓↑↓ configuration are nearly 2.64 Å, while for the ↑↑↓↓ configuration, the Co-Mn bond distance is approximately 2.63 Å between sites with the same spin and nearly 2.66 Å between sites with opposite spin. Fig. 4.2 shows the density of states of Mn d orbitals and Co d orbitals with the spin-projection, for ↑↓↑↓ which coincides with what we found for ↑↑↓↓ configuration. $Mn^{4+}O_6$ has an octahedral coordination. In the prsence of crystal field, the Mn d orbitals split into t_{2g} and e_g orbitals. The t_{2g} orbitals consist of d_{xy}, d_{yz}, and d_{xz} orbitals, while the e_g orbitals consist of d_{z^2} and $d_{x^2-y^2}$. The spin-projected density of states (Fig. 4.2 b) clearly shows the electronic configuration of the Mn d orbitals. All majority spin states of t_{2g} orbitals are filled, while both the majority and minority spin channels of e_g symmetry and the minority spin channel of t_{2g} are unoccupied. Due to exchange splitting, the sharp peaks in the conduction band for the majority spin channel correspond to e_g symmetry, while the two peaks in the minority spin channel correspond to t_{2g} and e_g symmetries, respectively. This confirms d^3 electronic configuration and indicates that Mn^{4+} is in a high-spin state with a magnetic moment of approximately 3.0 μ_B. On the other hand, Co is situated in a trigonal prismatic environment, where the d-orbitals typically split as follows: (d_{z^2}), ($d_{x^2-y^2}$, d_{xy}), and (d_{xz}, d_{yz}), with degenerate states indicated in parentheses.

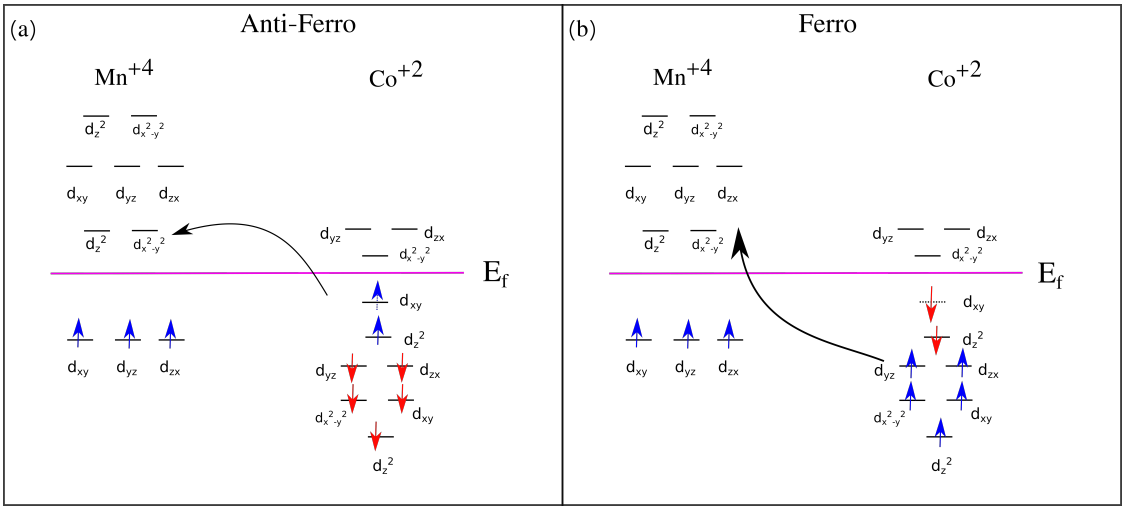

Figure 4.3: Schematic diagram of the electron configurations for Mn^{4+} and Co^{2+} atoms and the possible exchange interactions. (a) Co and Mn atoms are arranged in the antiferromagnetic configuration. (b) Co and Mn atoms are arranged in the ferromagnetic configuration. The up arrow signifies the majority spin, and the down arrow signifies the minority spin.

In the density of states of the Co^{2+} atom (Fig. 4.2 a), the first peak in the conduction band corresponds to the minority spin channel of the $d_{x^2-y^2}$ orbital. The second peak corresponds to the minority spin channel of the d_{yz} and d_{xz} orbitals. This indicates that the majority spin channel of all the orbitals is fully occupied, while the minority spin channels of the $d_{x^2-y^2}$, d_{yz}, and d_{xz} orbitals remain unoccupied. This configuration confirms that Co^{2+} is in a high-spin state with a d^7 electronic configuration, resulting in a magnetic moment of approximately 2.7 μ_B. Although the $d_{x^2-y^2}$ and d_{xy} orbitals are degenerate in a trigonal prismatic environment, the correlation effect U lifts this degeneracy in the minority spin channel (see Fig. 4.3),leading to the occupation of the d_{xy} orbital. We now analyze the possibility of magnetic exchange, either ferromagnetic or antiferromagnetic, between Co and Mn atoms based on their electronic configurations. In the antiferromagnetic configuration, electrons in the higher-energy minority spin channels of the d_{xy} orbital of the Co atom can readily hop to the same character on the Mn site. In contrast, in the ferromagnetic configuration, such hopping would require electrons to move from the deeper energy levels of the d_{xz} and d_{yz} orbitals. Therefore, the antiferromagnetic configuration results in a greater energy gain relative to the ferromagnetic configuration. That is why the nearest-neighbor exchange favors the stability of the $\uparrow\downarrow\uparrow\downarrow$ magnetic ground state.

To investigate the dominant magnetic interactions, we mapped the GGA+U magnetic band structure onto a tight-binding model using Wannier functions for the ground-state

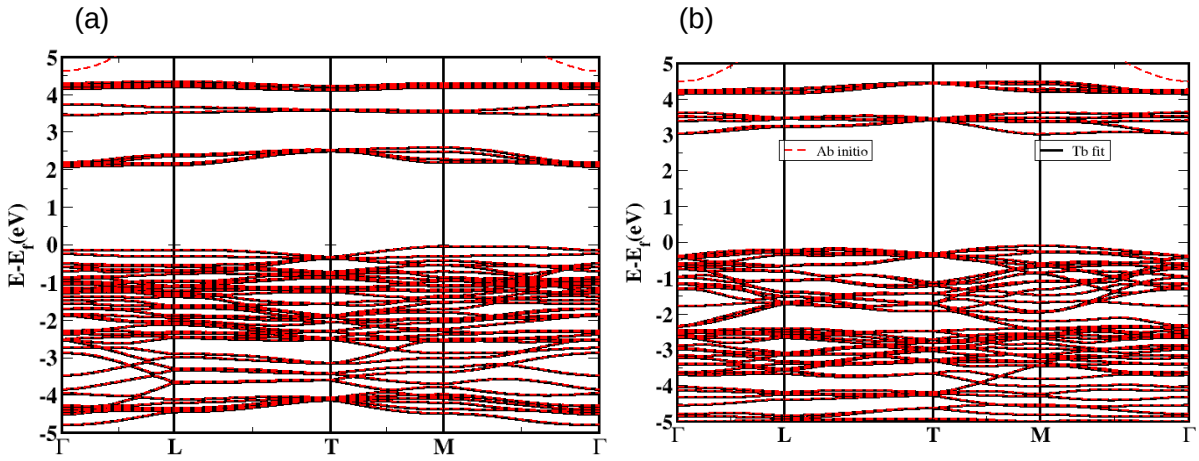

Figure 4.4: Comparison between the the tight-binding model and *ab initio* spin-polarized band structure for the ↑↓↑↓ magnetic configuration, shown separately for (a) the majority (spin-up) channel and (b) the minority (spin-down) channel.

↑↓↑↓ magnetic configuration. We used Co d, Mn d, and O p orbitals as the basis. The resulting tight-binding band structure (as shown in Fig. 4.4) shows good agreement with the spin-polarized *ab initio* band structure in both spin channels, validating the model Hamiltonian for further analysis. We then went on to determine the energy for hopping pathways. We computed the total energy by summing all eigenvalues up to the Fermi level. The hopping strength along relevant exchange pathways was quantified by calculating the change in energy upon selectively switching off specific hopping terms, as illustrated schematically in Fig. 4.5. We found the gain of direct hopping between two cations is very small, which is approximately 0.01 eV, suggesting that the coupling between the Co and Mn atoms takes place via the oxygen atoms. For this purpose, we have switched off all Mn–O–Co pathways between Co^{2+}–Mn^{4+} pairs, and the energy from this pathway is found to be 5.56 eV. Based on these findings, we can infer that there is no direct overlap between Co and Mn atoms. The exchange pathway is by virtual hopping through oxygen atoms. There are also finite interactions between next-nearest-neighbor Co–Co or Mn–Mn atoms through Mn–O–O–Mn or Co–O–O–Co pathways. These interaction strengths can be quantified through oxygen-to-oxygen hopping. The energy of this hopping is nearly 0.44 eV for Co–O-O-Co and 0.08 eV for Mn–O–O–Mn, which are much smaller than the closest-neighbor superexchange interaction. There is also a chance of O–O hopping

between inter-chain atoms, but the overall energy gain is very small, which suggests that there is weak coupling between the chains. Therefore, the dominant contribution comes from nearest neighbour Co-Mn super exchange interaction hopping via oxygen atoms. This analysis supports the use of a nearest-neighbor Heisenberg model.

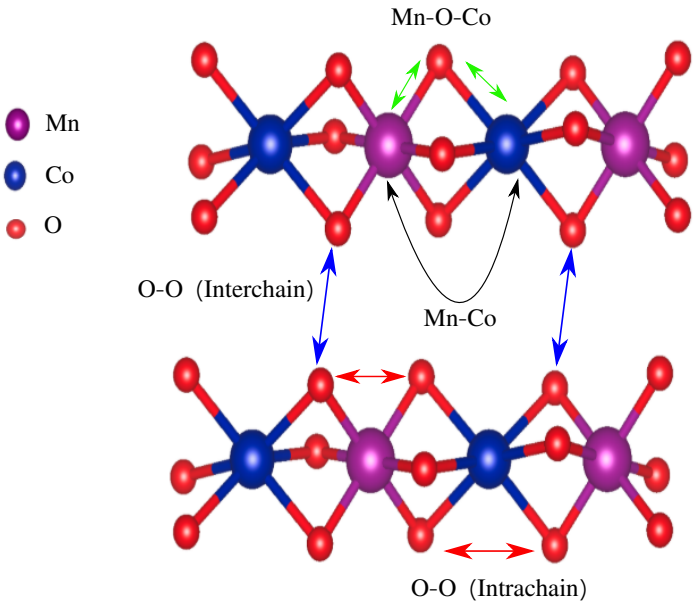

Figure 4.5: A schematic diagram illustrating the hopping pathways, represented by the arrows, in the Ising chain composed of Co and Mn atoms.

As interchain hopping components are not giving much energy gain, we considered only intrachain interactions and mapped the Heisenberg Hamiltonian onto our DFT model to extract different exchange interaction parameters. In this case, we have taken the ground state structure optimized in the ↑↓↑↓ magnetic configuration and determined the total energy using DFT calculations for various spin configurations. The total energy (per formula unit) can be expressed as:

$$E_{\uparrow\downarrow\uparrow\downarrow} = E_0 + 2J_{\text{Co-Mn}} - J'_{\text{Mn-Mn}} - J'_{\text{Co-Co}}$$

$$E_{\uparrow\uparrow\downarrow\downarrow} = E_0 + J'_{\text{Mn-Mn}} + J'_{\text{Co-Co}}$$

$$E_{\uparrow\downarrow\downarrow\downarrow} = E_0 + J'_{\text{Mn-Mn}} - J'_{\text{Co-Co}}$$

$$E_{\uparrow\uparrow\uparrow\uparrow} = E_0 - 2J_{\text{Co-Mn}} - J'_{\text{Mn-Mn}} - J'_{\text{Co-Co}}$$

Here values of magnetic moments are absorbed in the exchange interaction parameters. J is the spin-exchange constants and E_0 is the spin independent constant of total energy. From these equations, we obtained the exchange parameters listed in Table 4.1. Interestingly, all these J s are anti-ferromagnetic and $J_{\text{Co-Mn}}$ plays the dominant role in stabilizing

the ↑↓↑↓ configuration. For ↑↑↓↓ configuration, there are no net Co-Mn exchange interactions. Thus, it is unlikely to be the ground state for x=1.0 in $Ca_3Co_{2-x}Mn_xO_6$, unless the contribution from Co-Mn interactions becomes small. Alternately, exchange striction in the ↑↑↓↓ configuration could lead to a non-vanishing contribution to the energy from nearest neighbour Mn-Co interactions, though this would be small.

Table 4.1: Spin exchange interactions parameters obtained from GGA+U calculations

Magnetic configuration	$J_{Co\text{-}Mn}$(meV)	$J'_{Mn\text{-}Mn}$(meV)	$J'_{Co\text{-}Co}$ (meV)
↑↓↑↓	-5	-1	-1

Next, we have introduced anti-site disorder in Ca_3CoMnO_6, considering different supercells and interchanging the positions of Co and Mn atoms depending on the percentages of disorder. Since ↑↑↓↓ and ↑↓↑↓ magnetic orderings are the two competing states in the ordered system, the relative energy differences between them serve as the basis for examining the stability of the ↑↑↓↓ configuration in case of disorder in the system. We have performed ab-initio calculations for 6.25 %, 10 %, 16.67 % and 25 % disorder imposing ↑↑↓↓ and ↑↓↑↓ magnetic ordering.

Disorder (eV)	$E_{↑↑↓↓}$-$E_{↑↓↑↓}$ (meV/f.u)
0.0 %	5
6.25 %	3
10 %	2
16.67%	-1
25 %	5

Table 4.2: Total energy differences between the ↑↑↓↓ and ↑↓↑↓ magnetic configurations as a function of positional cationic disorder percentage.

The energy differences between these structures, as listed in Table 4.2 and plotted schematically in Fig. 4.6 c (for visual guidance), clearly indicate that the stability of the ↑↑↓↓ magnetic configuration increases with cationic disorder. However, this trend is not monotonic. Beyond a certain degree of disorder, the stability again decreases. Therefore, cationic disorder can indeed stabilize the ↑↑↓↓ magnetic configuration, but only within a specific range. To understand the origin of this stabilization, we analyze the structural and magnetic changes in both magnetic configurations. The structural modifications for both configurations are shown schematically in Fig. 4.6 a and 4.6 b, corresponding to 16.67% disorder. In this case, the Co^{2+}–O and Mn^{4+}–O bond lengths remain similar to those in the ordered structure, whereas some Mn^{3+}–O bonds exhibit noticeable distortions, with bond lengths ranging from approximately 2.33 Åto 2.42 Å.

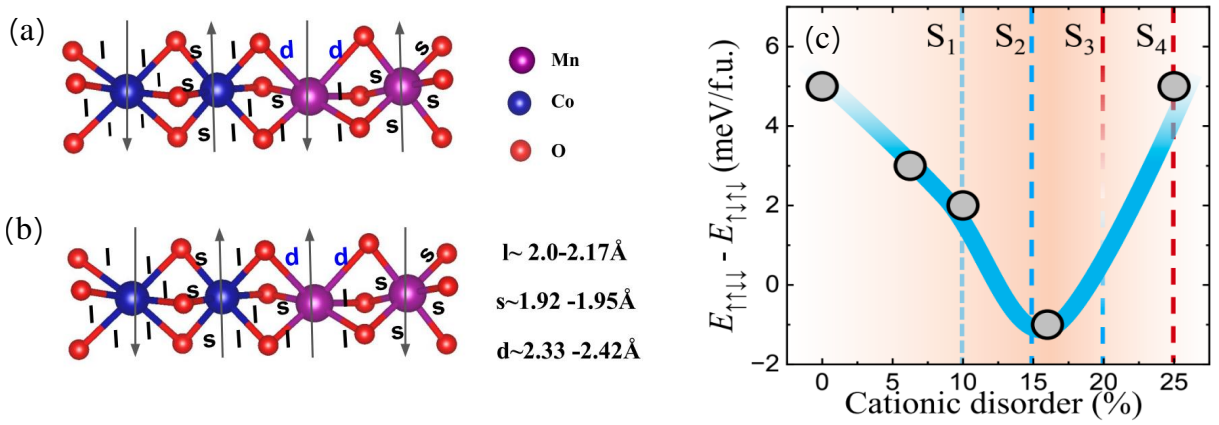

Figure 4.6: Co-Mn chains for optimized structure with 16.67 % disorder for (a) ↓↑↓↑ magnetic ordering and (b) ↓↑↑↓ magnetic ordering. (c) The energy differences between ↑↑↓↓ and ↑↓↑↓ states in Ca_3CoMnO_6 with different percentages of disorder.

As established from the analysis of hopping pathways, the exchange mechanism occurs via oxygen atoms. In the disordered system, certain Mn-O bonds are elongated compared to the average Mn-O bond lengths, thereby reducing the effective hopping strength along those pathways,as illustrated in Fig. 4.6 a and b. This implies that the nearest-neighbor exchange interactions are weakened in both the ↑↑↓↓ and ↑↓↑↓ configurations in the presence of disorder. Interestingly,in the ordered ↑↑↓↓ configuration, there is no net contribution from the nearest-neighbor exchange term ($J_{\text{Co-Mn}}$) in the spin exchange energy.

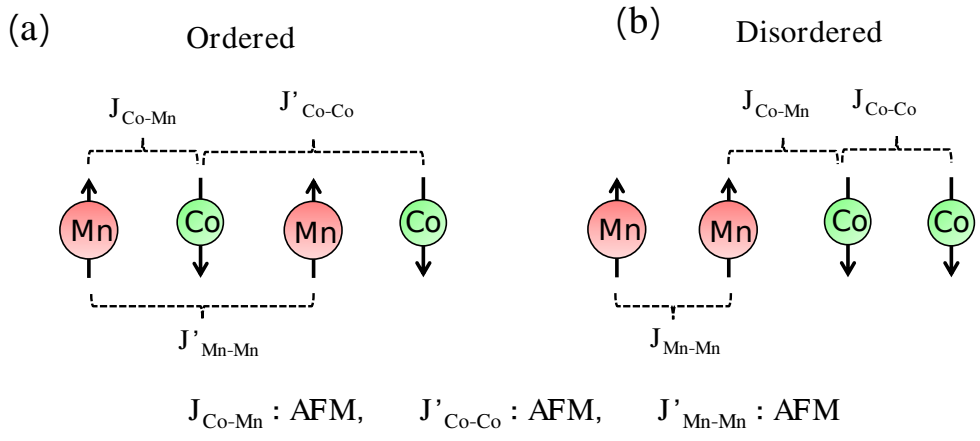

Figure 4.7: Schematic representation of the exchange interactions in the ground state magnetic configuration of (a) the ordered system and (b) the 16.67% cation-disordered system.

However, in the disordered system, local environments arise in which Co-Co, Mn-Mn, and Co-Mn pairs become nearest neighbors, thereby introducing additional nearest-neighbor exchange contributions due to nearest-neighbor Co-Co and Mn-Mn interactions,

as schematically shown in Fig. 4.7 b. As a result, the ↑↑↓↓ configuration can gain stability through these interactions and emerge as the ground state under moderate disorder. In summary, the key mechanism underlying this stabilization is the reduction in effective nearest-neighbor exchange interactions due to structural distortions induced by cationic disorder.

4.4 Summary

In summary, our first-principles DFT-based calculations reveal that the ↑↑↓↓ collinear magnetic ordering, which is responsible for inducing ferroelectricity, can be engineered in stoichiometric Ca_3CoMnO_6 by introducing an optimal degree of cationic positional disorder. The stabilization of the ↑↑↓↓ magnetic configuration over the competing ↑↓↑↓ ordering becomes possible due to the emergence of nearest-neighbor Co-Co and Mn-Mn exchange interactions in the positionally disordered compound. However, when the level of cationic disorder becomes relatively high, it leads to multiple magnetic ground states ultimately destabilizing the ↑↑↓↓ configuration in Ca_3CoMnO_6. Gaining insight into the factors governing the stability of this magnetic ordering is essential for improving control over the material's type-II multiferroic behavior.

Bibliography

[1] N. A. Spaldin and R. Ramesh. Advances in magnetoelectric multiferroics. *Nature Materials*, 18(3):203–212, Mar 2019.

[2] T. Kimura, T. Goto, H. Shintani, K. Ishizaka, T. Arima, and Y. Tokura. Magnetic control of ferroelectric polarization. *Nature*, 426(6962):55–58, Nov 2003.

[3] Huili Liu, Jiong Yang, Xun Shi, Sergey A. Danilkin, Dehong Yu, Chao Wang, Wenqing Zhang, and Lidong Chen. Reduction of thermal conductivity by low energy multi-einstein optic modes. *Journal of Materiomics*, 2(2):187–195, Jun 2016.

[4] Manfred Fiebig, Thomas Lottermoser, Dennis Meier, and Morgan Trassin. The evolution of multiferroics. *Nature Reviews Materials*, 1(8):16046, Jul 2016.

[5] Y. J. Choi, H. T. Yi, S. Lee, Q. Huang, V. Kiryukhin, and S.-W. Cheong. Ferroelectricity in an ising chain magnet. *Phys. Rev. Lett.*, 100:047601, Jan 2008.

[6] Hua Wu, T. Burnus, Z. Hu, C. Martin, A. Maignan, J. C. Cezar, A. Tanaka, N. B. Brookes, D. I. Khomskii, and L. H. Tjeng. Ising magnetism and ferroelectricity in ca_3comno_6. *Phys. Rev. Lett.*, 102:026404, Jan 2009.

[7] P. Ding, L. Li, Y. J. Guo, Q. Y. He, X. S. Gao, and J.-M. Liu. Influence of Co:Mn ratio on multiferroicity of $Ca_3Co_{2-x}Mn_xO_6$ around x$\sim$1. *Applied Physics Letters*, 97(3):032901, Jul 2010.

[8] V. Kiryukhin, Seongsu Lee, W. Ratcliff, Q. Huang, H. T. Yi, Y. J. Choi, and S-W. Cheong. Order by static disorder in the ising chain magnet $Ca_3Co_{2-x}Mn_xO_6$. *Phys. Rev. Lett.*, 102:187202, May 2009.

[9] L. Lin, Y. J. Guo, Y. L. Xie, S. Dong, Z. B. Yan, and J.-M. Liu. Spin frustration destruction and ferroelectricity modulation in ca3comno6: Effects of mn deficiency. *Journal of Applied Physics*, 111(7):07D901, Feb 2012.

[10] J. Shi, J. D. Song, J. C. Wu, X. Rao, H. L. Che, Z. Y. Zhao, H. D. Zhou, J. Ma, R. R. Zhang, L. Zhang, X. G. Liu, X. Zhao, and X. F. Sun. Ferroelectricity of structural origin in the spin-chain compounds $Ca_3Co_{2-x}Mn_xO_6$. *Phys. Rev. B*, 96:064112, Aug 2017.

[11] James M. Rondinelli, Aaron S. Eidelson, and Nicola A. Spaldin. Non-d^0 mn-driven ferroelectricity in antiferromagnetic $BaMnO_3$. *Phys. Rev. B*, 79:205119, May 2009.

[12] Y. Zhang, H. J. Xiang, and M.-H. Whangbo. Interplay between jahn-teller instability, uniaxial magnetism, and ferroelectricity in Ca_3CoMnO_6. *Phys. Rev. B*, 79:054432, Feb 2009.

[13] P. E. Blöchl. Projector augmented-wave method. *Phys. Rev. B*, 50:17953–17979, Dec 1994.

[14] G. Kresse and J. Hafner. Ab initio molecular dynamics for liquid metals. *Phys. Rev. B*, 47:558–561, Jan 1993.

[15] G. Kresse and J. Hafner. Ab initio molecular-dynamics simulation of the liquid-metal–amorphous-semiconductor transition in germanium. *Phys. Rev. B*, 49:14251–14269, May 1994.

[16] G. Kresse and J. Furthmüller. Efficient iterative schemes for ab initio total-energy calculations using a plane-wave basis set. *Phys. Rev. B*, 54:11169–11186, Oct 1996.

[17] John P. Perdew, Kieron Burke, and Matthias Ernzerhof. Generalized gradient approximation made simple. *Phys. Rev. Lett.*, 77:3865–3868, Oct 1996.

[18] S. L. Dudarev, G. A. Botton, S. Y. Savrasov, C. J. Humphreys, and A. P. Sutton. Electron-energy-loss spectra and the structural stability of nickel oxide: An lsda+u study. *Phys. Rev. B*, 57:1505–1509, Jan 1998.

[19] VG Zubkov, GV Bazuev, AP Tyutyunnik, and IF Berger. Synthesis, crystal structure, and magnetic properties of quasi-one-dimensional oxides ca_3cumno_6 and $ca3co_{1+x}mn_{1-x}o_6$. *Journal of Solid State Chemistry*, 160(2):293–301, 2001.

[20] Hendrik J. Monkhorst and James D. Pack. Special points for brillouin-zone integrations. *Phys. Rev. B*, 13:5188–5192, Jun 1976.

[21] Arash A. Mostofi, Jonathan R. Yates, Giovanni Pizzi, Young-Su Lee, Ivo Souza, David Vanderbilt, and Nicola Marzari. An updated version of wannier90: A tool for obtaining maximally-localised wannier functions. *Computer Physics Communications*, 185(8):2309–2310, 2014.

Chapter 5

Understanding the Magnetism of 25% Fe intercalated $NbSe_2$

5.1 Introduction

Layered compounds have been extensively studied in recent decades due to their rich and diverse physical properties [1–3]. Among these, transition metal dichalcogenides (TMDs) have garnered significant interest, especially for their intriguing phenomena such as charge density wave (CDW). These materials generally follow the formula MX_2, where M is a transition metal and X is a chalcogen element such as S, Se, or Te. They exhibit a quasi-two-dimensional structure comprising X-M-X layers that form individual slabs [1], which stack via Van Der Waals interactions. Transition metal dichalcogenides exhibit polymorphism due to different stacking sequences of the MX_2 layers, while maintaining the same stoichiometry [4–7]. These polytypes differ in terms of stacking order, metal coordination, and symmetry, and are commonly labeled as 1T, 3R, 6R, 2H, 4H, 6H etc., where the numeral indicates the number of layers in the unit cell and the letter designates the crystal symmetry. Among these, the 2H-$NbSe_2$ polytype has been widely studied due to its relatively high superconducting transition temperature ($T_c \approx 7.0\,\mathrm{K}$) and a charge density wave (CDW) transition around 33 K [8]. Intercalation in layered materials can induce structural phase transitions and significantly modify their physical properties [9]. First-row transition metal intercalants are particularly interesting, as 3d ions can form ordered superlattices at specific concentrations, leading to magnetic ordering either ferromagnetic or antiferromagnetic, typically below 160 K [10]. In such systems, the trigonal prismatic coordination of Nb with surrounding chalcogen atoms is usually retained, while the intercalated 3d ions occupy octahedral sites between the layers. The nature of the structural transitions and the emergence of magnetic behavior are highly dependent on both the concentration of the intercalant and the chemical environment of the MX_2 host matrix. For example, at equivalent Cr intercalation levels, $Cr_{0.33}NbSe_2$ [11, 12] exhibits ferromagnetic order, whereas the sulfur-based analogue develops a complex helical spin configuration. Chromium-intercalated compounds, such as Cr_xNbSe_2, display a rich variety of magnetic states, such as spin-glass behavior at low concentrations ($0.05 < x < 0.25$), cluster-glass states at intermediate concentrations, and long-range magnetic order at higher doping levels [13]. Beyond magnetic effects, intercalation can also drive struc-

tural transformations. For instance, Ag intercalation converts the 2H phase of $NbSe_2$ into the 1T phase in Ag_xNbSe_2 [14]. The resulting magnetic ordering generally depends on the specific 3d element inserted into the van der Waals gap and tends to follow similar trends in both Nb and Ta-based systems, typically leading to either ferromagnetic or antiferromagnetic states. An exception is observed with Fe intercalation, where Fe_xTaX_2 (X = S, Se) displays ferromagnetism and Fe_xNbX_2 under similar conditions favors antiferromagnetic ordering for compositions such as $x = 1/4$ or $1/3$ [15]. Increasing the intercalation concentration often induces a transition between different magnetic phases. Notably, antiferromagnetic ordering has been observed at $x = 0.25$ in Fe_xNbSe_2, where the Néel temperature reaches a maximum of $T_N = 175\,\mathrm{K}$, before decreasing to $T_N = 122\,\mathrm{K}$ at $x = 1/3$. Although the magnetic ground state has been experimentally identified, a comprehensive theoretical analysis of the underlying magnetic interactions has not been well explored. In this chapter,[1] we focus on Fe intercalation at 25% concentration. Using density functional theory (DFT+U) calculations, we have systematically investigated various magnetic configurations and identified the ground state. We constructed a multiband Hubbard model by mapping the non-magnetic DFT electronic structure onto a tight-binding model, from which we extracted the hopping integrals and onsite energy parameters.This model enabled us to examine different exchange pathways. By computing the energy gain associated with each exchange mechanism, we found the microscopic origin of the stability of the antiferromagnetic structure as revealed by our DFT analysis.

5.2 Methodology

Density functional theory (DFT) calculations were performed using the projector augmented-wave (PAW) method [16],following the implementation in the Vienna *ab-initio* Simulation Package (VASP) [17]. Exchange-correlation interactions were treated considering the generalized gradient approximation (GGA) [18]. To incorporate the on-site electron correlation effects in the Fe d orbitals, the GGA+U approach proposed by Dudarev [19] was adopted, with an effective Hubbard U value of 3 eV applied to Fe sites. The calculations were performed on the experimentally determined hexagonal crystal structure (space group $P6_3/mmc$) of $NbSe_2$ [9]. To model 25% Fe intercalation, a $2 \times 2 \times 1$ supercell was constructed in which Fe atoms occupy the Van Der Waals gap between the two layers forming the magnetic unit cell. For further analysis, a $2 \times 1 \times 1$ supercell of this magnetic cell was used to explore various magnetic configurations.

[1] chapter 5 is based on publication number 5 in the publication list

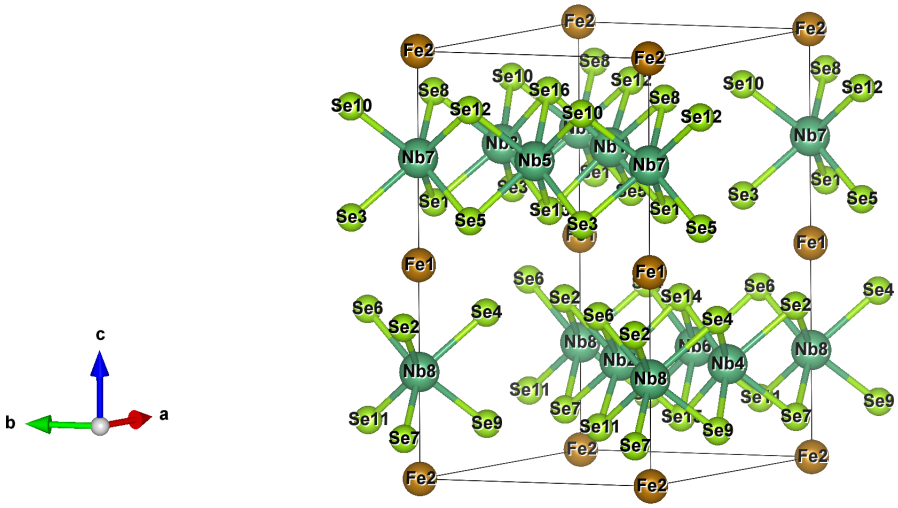

Figure 5.1: The hexagonal unit cell of 25 % Fe intercalated $NbSe_2$.

A kinetic energy cutoff for the plane wave basis is taken as 600 eV and a Monkhorst-Pack $4 \times 8 \times 4$ k point mesh were used for Brillouin zone sampling [20].To analyze the exchange pathways, we constructed a multiband Hubbard model using the optimized structure. We first fitted the non-magnetic DFT band structure to a tight-binding model, which showed good agreement, as illustrated in Fig. 5.1.

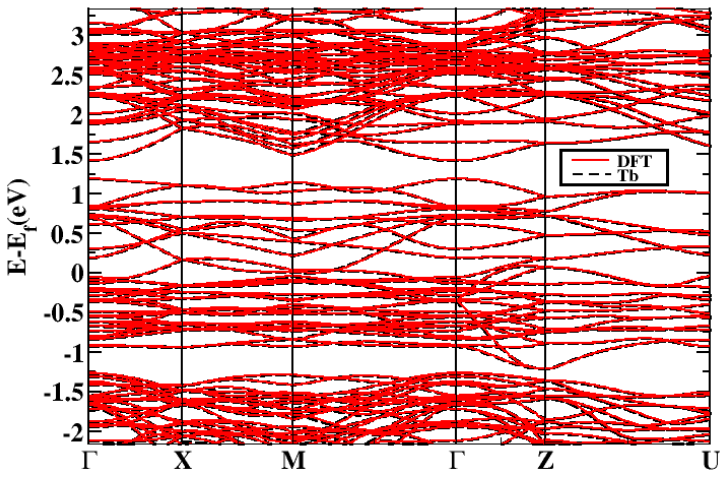

Figure 5.2: A comparison of the nonmagnetic band structures obtained from *ab initio* and tight-binding model calculations using the optimized structure of the AFM1 configuration.

The tight-binding Hamiltonian was constructed using Fe-d, Nb-d, and Se-p orbitals in the basis. The radial part of the wavefunctions was constructed using maximally local-

Spread of the Wannier functions (Å)^2		
Atomic Orbital	Largest spread	Smallest spread
Nb-d	1.8	2.2
Se-p	1.9	2.1
Fe-d	0.6	0.9

Table 5.1: The range of spreads of the Wannier functions for Nb-d,Fe-d and Se-p orbitals.

ized Wannier functions through the WANNIER90-VASP interface [21], as implemented in VASP. From the fitting, we obtained both onsite energies and hopping interaction strengths. The spread of Wannier functions of each atomic function is given in the table 5.1, which supports that they are localized on a specific atomic orbital. Next, we introduce on-site Columb interactions on the Fe d-orbitals. The total Hamiltonian is given by:

$$
\begin{aligned}
H = & \sum_{i,l,\sigma} \epsilon_p \, p^{\dagger}_{il\sigma} p_{il\sigma} + \sum_{i,l,\sigma} \epsilon_d^{Nb} \, d^{\dagger}_{il\sigma} d_{il\sigma} + \sum_{i,l,\sigma} \epsilon_d^{Fe} \, d^{\dagger}_{il\sigma} d_{il\sigma} \\
& - \sum_{i,j,l_1,l_2,\sigma} t^{pp}_{l_1 l_2}(Se_i, Se_j) \, p^{\dagger}_{il_1\sigma} p_{jl_2\sigma} + \text{H.c.} \\
& - \sum_{i,j,l_1,l_2,\sigma} t^{pd}_{l_1 l_2}(Se_i, Nb_j) \, d^{\dagger}_{il_1\sigma} p_{jl_2\sigma} + \text{H.c.} \\
& - \sum_{i,j,l_1,l_2,\sigma} t^{pd}_{l_1 l_2}(Se_i, Fe_j) \, d^{\dagger}_{il_1\sigma} p_{jl_2\sigma} + \text{H.c.} \\
& - \sum_{i,j,l_1,l_2,\sigma} t^{dd}_{l_1 l_2}(Fe_i, Nb_j) \, d^{\dagger}_{il_1\sigma} d_{jl_2\sigma} + \text{H.c.} \\
& - \sum_{i,j,l_1,l_2,\sigma} t^{dd}_{l_1 l_2}(Fe_i, Fe_j) \, d^{\dagger}_{il_1\sigma} d_{jl_2\sigma} + \text{H.c.} \\
& - \sum_{i,j,l_1,l_2,\sigma} t^{dd}_{l_1 l_2}(Nb_i, Nb_j) \, d^{\dagger}_{il_1\sigma} d_{jl_2\sigma} + \text{H.c.} \\
& + \sum_{\alpha,\beta,\gamma,\delta} \sum_{\sigma_1,\sigma_2,\sigma_3,\sigma_4} U^{dd}_{\alpha\beta\gamma\delta} \, d^{\dagger}_{\alpha\sigma_1} d^{\dagger}_{\beta\sigma_2} d_{\gamma\sigma_3} d_{\delta\sigma_4}
\end{aligned}
\tag{5.1}
$$

The first three terms in the Hamiltonian represent the onsite energies of the Se-p, Fe-d, and Nb-d orbitals. The following six terms describe the hopping interactions, derived from a non-magnetic tight-binding model constructed using Wannier functions. The final term accounts for the onsite Coulomb interaction, implemented via the Hubbard U on the Fe-d orbitals. In this formalism, $p^{\dagger}_{i\,l\,\sigma}$ and $p_{i\,l\,\sigma}$ denote the creation and annihilation operators for an electron with spin σ in the l-th p orbital on a Se atom in the i-th unit cell. Likewise, $d^{\dagger}_{i\,l\,\sigma}$ and $d_{i\,l\,\sigma}$ are the corresponding operators for the l-th d orbital on a Nb atom, and Fe atom. The term $U^{dd}_{\alpha\beta\gamma\delta}$ represents the Coulomb interaction among electrons on the Fe site

In our model, we express the Coulomb matrix elements for the Fe d-orbitals using the Slater integrals F_0, F_2, and F_4, [22] which are measured in energy units. This approach ensures that the Coulomb interaction remains rotationally invariant (i.e., not a function of the magnetic quantum number m_l) and properly accounts for multi-orbital effects. We varied the parameters to reproduce the trends observed in the DFT+U calculations. The corresponding U_{eff} and J values were computed as functions of the Slater integrals F_0, F_2, and F_4, with $U_{eff} = 3\,\text{eV}$ and $J = 0.5\,\text{eV}$. A mean-field decoupling scheme is employed for the four-fermion interaction terms, such as:

$$\begin{aligned} d^\dagger_{i\uparrow}d_{i\uparrow}d^\dagger_{i\downarrow}d_{i\downarrow} = {} & \langle d^\dagger_{i\uparrow}d_{i\uparrow}\rangle d^\dagger_{i\downarrow}d_{i\downarrow} + d^\dagger_{i\uparrow}d_{i\uparrow}\langle d^\dagger_{i\downarrow}d_{i\downarrow}\rangle \\ & - \langle d^\dagger_{i\uparrow}d_{i\downarrow}\rangle d^\dagger_{i\downarrow}d_{i\uparrow} - d^\dagger_{i\uparrow}d_{i\downarrow}\langle d^\dagger_{i\downarrow}d_{i\uparrow}\rangle \\ & - \langle d^\dagger_{i\uparrow}d_{i\uparrow}\rangle\langle d^\dagger_{i\downarrow}d_{i\downarrow}\rangle + \langle d^\dagger_{i\uparrow}d_{i\downarrow}\rangle\langle d^\dagger_{i\downarrow}d_{i\uparrow}\rangle \end{aligned} \tag{5.2}$$

The Hamiltonian expressed in real space was converted to momentum space, following which self-consistent calculations were carried out to determine the total energy corresponding to each magnetic configuration. The total energy was obtained by summing the eigenvalues of all occupied states. To quantify the band energy gain due to hopping, we selectively turned off different hopping pathways and compared the band energy with the reference system where all hopping interactions were active.

5.3 Result and Discussion

We attempted to understand the origin of magnetism in $NbSe_2$ with 25% Fe intercalation using DFT+U calculations. The unit cell of $NbSe_2$ has a hexagonal structure, consisting of two Nb atoms, each enclosed by six chalcogen atoms in a trigonal prismatic environment. To model 25% intercalation, a 2×2×1 superlattice was constructed, with Fe atoms occupying octahedral sites within the van der Waals gap, coordinated by Se atoms. To explore additional configurations, we constructed a 2×1×1 supercell containing four Fe atoms per magnetic unit cell. To compare the total energy of the ferromagnetic configuration, we considered three types of antiferromagnetic (AFM) configurations, schematically shown in Fig. 5.3 and labeled as AFMI, AFMII, and AFMIII.

In the AFMI configuration, all in-plane Fe atoms are coupled ferromagnetically, while the out-of-plane Fe atoms are coupled antiferromagnetically. In the AFMII configuration, in-plane atoms along the a-direction are coupled antiferromagnetically, whereas atoms along the b-direction are coupled ferromagnetically. The out-of-plane atoms are again coupled antiferromagnetically. In the AFMIII configuration, all out-of-plane atoms are

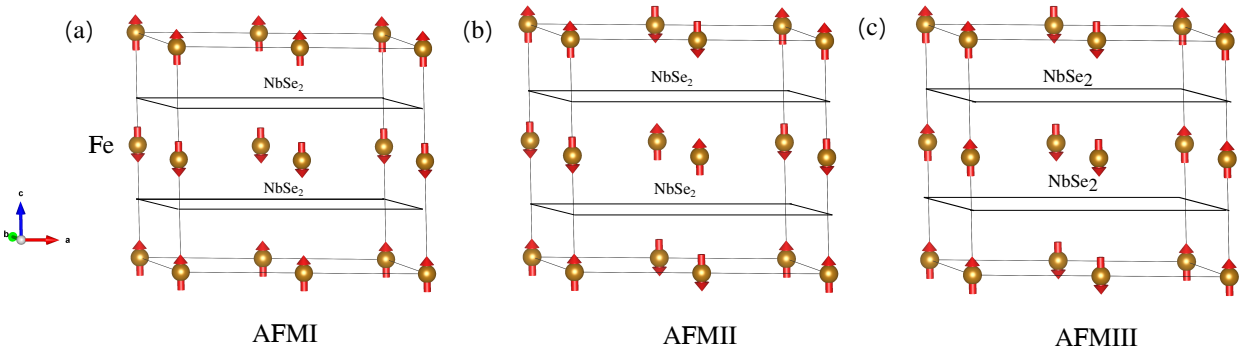

Figure 5.3: Schematic diagram showing the different magnetic configurations: (a) AFM I, (b) AFM II, and (c) AFM III. .

coupled ferromagnetically, while in-plane atoms are coupled ferromagnetically along the a-direction and antiferromagnetically along the b-direction. In our DFT+U calculations, we optimized only the internal atomic positions for each magnetic configuration and evaluated their total energies. The resulting structural differences among the configurations were found to be minimal. Among them, the AFMI configuration emerged as the lowest-energy state. In this configuration, the Fe-Se bond length is approximately 2.55 Å, the Nb-Se bond length is 2.63 Å, and the Fe-Nb distance is 3.15 Å. The out-of-plane Fe-Fe distance is 6.30 Å, while the in-plane Fe-Fe distance is 6.94 Å.

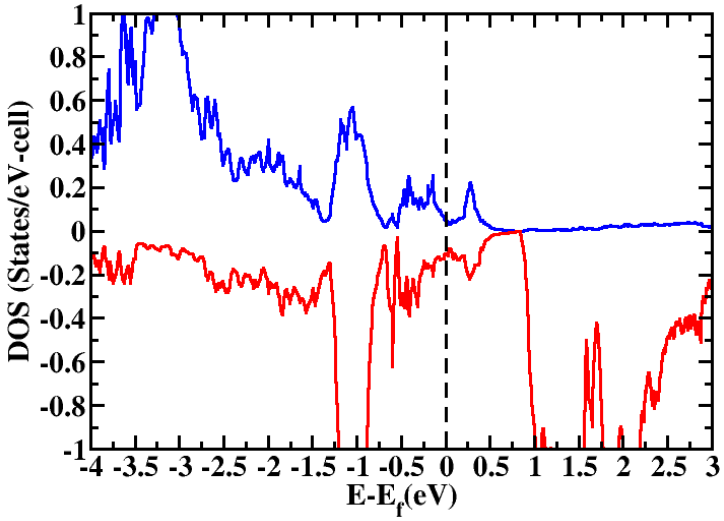

Figure 5.4: Spin resolved density of states of Fe d orbital

As Fe sits in an octahedral environment, its d-orbitals split into t_{2g} and e_g orbitals. The computed density of states (DOS), illustrated in Fig. 5.4, indicates pronounced spin polarization of the Fe 3d orbitals. In particular, the states in majority spin channel are completely filled, while the minority-spin t_{2g} states exhibit partial occupancy. This results

in a magnetic moment of approximately 3.3 μ_B per Fe atom, consistent with a high-spin Fe^{2+} (d^6) configuration.

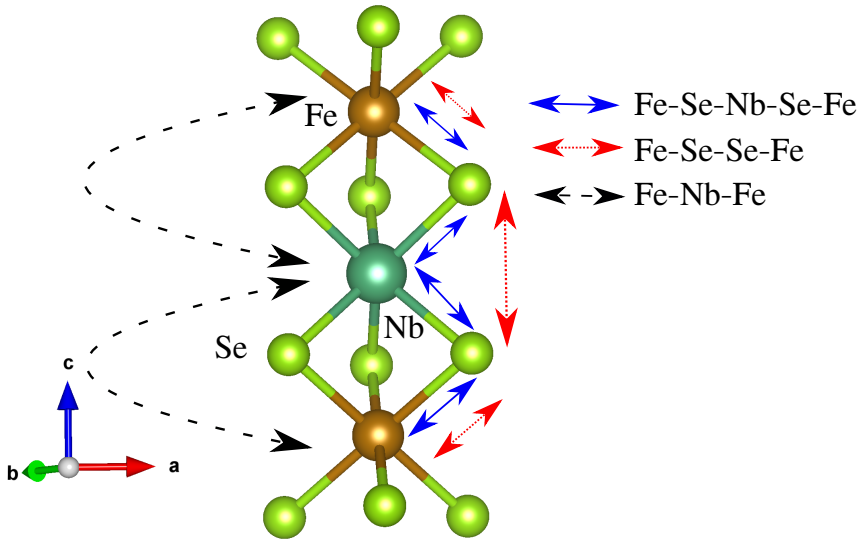

Figure 5.5: Schematic diagram presenting the possible hopping pathways .

To determine the magnitude and nature of the exchange interactions, we mapped the DFT model onto the nearest-neighbor Heisenberg Hamiltonian, as given in Equation (5.3):

$$\hat{H} = -\sum_{\langle i,j \rangle} J_{ij}\, \mathbf{S}_i \cdot \mathbf{S}_j \tag{5.3}$$

Since the magnetic moments of the Fe atoms are identical, the electrons are strongly localized around the Fe sites, justifying the use of the Heisenberg model. For the nearest-neighbor Heisenberg model, two independent interaction terms are possible: the in-plane exchange term, denoted as J_{in}, and the out-of-plane exchange term, denoted as J_{out}. To determine the exchange interaction constants, we used the optimized AFMI structure and computed the total energy using DFT calculations for various spin configurations, keeping the crystal structure fixed. As a result, the spin-independent part of the total energy remains the same for all cases. The total energy per formula unit can be expressed as:

$$\begin{aligned} \mathrm{E_{AFMI}} &= \mathrm{E_0} + \mathrm{J_{out}} - 3\mathrm{J_{in}} \\ \mathrm{E_{FM}} &= \mathrm{E_0} - \mathrm{J_{out}} - 3\mathrm{J_{in}} \\ \mathrm{E_{AFMII}} &= \mathrm{E_0} + \mathrm{J_{out}} + \mathrm{J_{in}} \end{aligned} \tag{5.4}$$

Here, the values of the magnetic moments are absorbed into the exchange interaction parameters. E_0 is the spin-independent contribution to the total energy. From these

Table 5.2: Spin exchange interactions parameters obtained from GGA+U calculations

Magnetic configuration	J_{out}(meV)	J_{in}(meV)
AFM1	-5	4

equations, we obtained the exchange parameters listed in Table 5.2. The out-of-plane exchange interaction is antiferromagnetic. In the Heisenberg model, hopping is treated as a perturbation; however, DFT is almost able to capture all interactions. To examine the exchange mechanism more precisely, we investigated the exchange pathways by quantifying the hopping strengths directly, without treating them as a perturbation. For this reason, we developed a multiband Hubbard model using the non-magnetic tight-binding part derived from DFT calculations. Details of this calculation are given in the Methodology section. This approach enabled us to identify and analyze the possible exchange pathways. The multiband Hubbard model, with parameters $U = 3.0$ eV and $J = 0.5$ eV, reproduces a trend similar to that of the DFT+U calculations.

Table 5.3: The comparison of the total energies for different magnetic configurations, performed using DFT+U calculations and model Hamiltonian methods.

Magnetic Configuration	**E-E_{AFMI}(DFT+U)(meV)**	**E-E_{AFMI}(model)(meV)**
AFM1	0	0
FM	36	49
AFM2	69	77
AFM3	100	157

In the Hubbard model, the total energy for each magnetic configuration was computed by summing all the occupied eigenvalues. A comparison of the energy differences between various magnetic configurations is presented in Table 5.3. In both the DFT+U and multiband Hubbard model calculations, the crystal structure optimized in the AFM1 magnetic configuration was used. The energy differences follow the same order in both methods, which supports the validity of our model construction.

Table 5.4: Different exchange pathways and the corresponding energy gain (EG) for each pathway with the energy differences between the two magnetic configurations.

Exchange Pathways	**EG_{AFMI}(eV)**	**EG_{FM}(eV)**	**EG_{AFMI}-EG_{FM}(meV)**
Fe-Se-Se-Fe	2.678	2.647	31
Fe-Nb-Fe	0.283	0.296	-13
Fe-Se-Nb-Se-Fe	14.902	14.892	10

Since AFM1 and FM are two competing magnetic states, both of which exhibit ferromagnetic alignment of in-plane Fe atoms, their energy difference primarily reflects the

nature of out-of-plane exchange interactions. We examined the spin-resolved charge density near the Fermi energy, as shown in Fig. 5.6. Near the Fermi level, the minority spin channel of the Fe t_{2g} orbitals plays a dominant role (Fig. 5.4). These t_{2g} orbitals form π-bonds with the Se p-orbitals. In another case, both Se atoms also engage in π-bonding. Thus, in the absence of a strong interaction pathway, the in-plane ferromagnetism mainly originates from the itinerant electrons due to the system's metallicity.

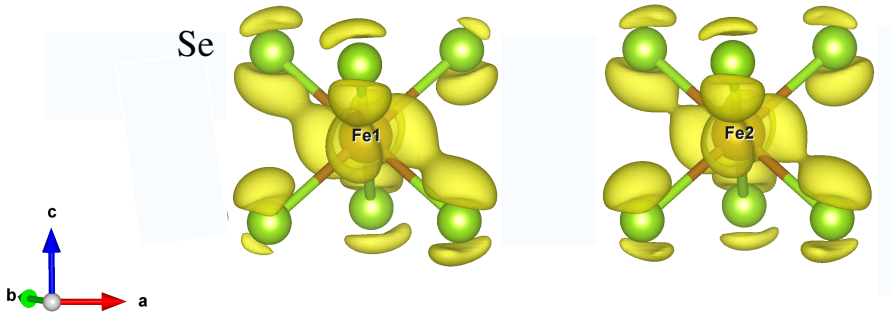

Figure 5.6: Spin resolved charge density below Fermi energy

Our primary interest lies in the interactions between the out-of-plane Fe atoms. To investigate the exchange pathways between two Fe atoms, we selectively switched off different hopping channels and calculated the corresponding total energies. The energy gain associated with each pathway was determined by evaluating the change in total energy due to the switching off of the certain hopping path. We compared these energy gains for the AFM1 and ferromagnetic configurations. Since the Fe-Fe distances are large, direct overlap is not feasible. Therefore, the dominant exchange pathways are Fe-Nb-Fe, Fe-Se-Se-Fe, and Fe-Se-Nb-Se-Fe, as illustrated in Fig. 5.5. The energy gains for these pathways are presented in Table 5.4. Our results indicate that the Fe-Se-Se-Fe and Fe-Se-Nb-Se-Fe pathways favor antiferromagnetic coupling, whereas the direct Fe-Nb-Fe path supports ferromagnetic alignment. Overall, the Fe-Se-Se-Fe pathway plays a dominant role in stabilizing the AFM1 magnetic structure.

5.4 Conclusion

In summary, our first-principles DFT-based calculations demonstrate an antiferromagnetic arrangement between the out-of-plane Fe atoms, while the in-plane Fe atoms exhibit ferromagnetic alignment. By mapping the DFT results onto the Heisenberg model, we find that the out-of-plane exchange interaction is antiferromagnetic. In contrast to the

Heisenberg picture, where hopping is treated as a perturbation, we constructed a multi-band Hubbard model that incorporates all relevant interactions with mean field treatment. This model successfully reproduces the correct magnetic ground state, consistent with both DFT calculations and experimental observations. Furthermore, our analysis identifies the dominant hopping pathways, particularly the Fe-Se-Se-Fe path, that stabilize the antiferromagnetic ground state.

Bibliography

[1] J.A. Wilson and A.D. Yoffe and. The transition metal dichalcogenides discussion and interpretation of the observed optical, electrical and structural properties. *Advances in Physics*, 18(73):193–335, 1969.

[2] Stijn Cuyvers, Bahawal Haq, Camiel Op de Beeck, Stijn Poelman, Artur Hermans, Zheng Wang, Agnieszka Gocalinska, Emanuele Pelucchi, Brian Corbett, Gunther Roelkens, Kasper Van Gasse, and Bart Kuyken. Low noise heterogeneous iii-v-on-silicon-nitride mode-locked comb laser. *Laser & Photonics Reviews*, 15(8):2000485, Aug 2021.

[3] Wonbong Choi, Nitin Choudhary, Gang Hee Han, Juhong Park, Deji Akinwande, and Young Hee Lee. Recent development of two-dimensional transition metal dichalcogenides and their applications. *Materials Today*, 20(3):116–130, 2017.

[4] D.T. Hughes, J. Evans, and I.R. Harris. The influence of lattice order on the thermal expansion and magnetic susceptibility behaviour of some palladium-cerium solid solution alloys. *Journal of the Less Common Metals*, 76(1):119–129, 1980.

[5] B. E. Brown and D. J. Beerntsen. Layer structure polytypism among niobium and tantalum selenides. *Acta Crystallographica*, 18(1):31–36, Jan 1965.

[6] F. Kadijk, R. Huisman, and F. Jellinek. The crystal structures of niobium(III) selenide and tantalum(III) selenide. *Acta Crystallographica Section B*, 24(8):1102–1106, Aug 1968.

[7] Kari Selte and Arne Kjekshus. On the structural properties of the $Nb_{1+x}Se_2$ phase. *Acta chem. scand.*, 18:697–706, 1964.

[8] P. Garoche, J. J. Veyssié, P. Manuel, and P. Molinié. Experimental investigation of superconductivity in 2H-$NbSe_2$ single crystal. *Solid State Communications*, 19(5):455–460, Jul 1976.

[9] Subham Naik, Abinash Pradhan, Aman Mishra, and Saroj L. Samal. Evolution of structural properties in fe intercalated 2H-$NbSe_2$: Phase transformation induced by strong host–guest interaction. *The Journal of Physical Chemistry C*, 126(32):13762–13773, Aug 2022.

[10] S. S. P. Parkin, , and R. H. Friend. 3d transition-metal intercalates of the niobium and tantalum dichalcogenides. ii. transport properties. *Philosophical Magazine B*, 41(1):95–112, Jan 1980.

[11] Tomonao Miyadai, Katsuya Kikuchi, Hiromitsu Kondo, Shuzo Sakka, Masatoshi Arai, and Yoshikazu Ishikawa. Magnetic properties of $Cr_{\frac{1}{3}}NbS_2$. *Journal of the Physical Society of Japan*, 52(4):1394–1401, Apr 1983.

[12] Y. Togawa, T. Koyama, K. Takayanagi, S. Mori, Y. Kousaka, J. Akimitsu, S. Nishihara, K. Inoue, A. S. Ovchinnikov, and J. Kishine. Chiral magnetic soliton lattice on a chiral helimagnet. *Phys. Rev. Lett.*, 108:107202, Mar 2012.

[13] N.M. Toporova, E.M. Sherokalova, N.V. Selezneva, V.V. Ogloblichev, and N.V. Baranov. Crystal structure, properties and griffiths-like phase in niobium diselenide intercalated with chromium. *Journal of Alloys and Compounds*, 848:156534, 2020.

[14] Kenta Mogami, Shun Ohta, and Hideaki Sakata. Appearance of unidirectional superstructure in silver intercalated 2H-$NbSe_2$. *Surface Science*, 707:121636, May 2021.

[15] H. Narita, H. Ikuta, H. Hinode, T. Uchida, T. Ohtani, and M. Wakihara. Preparation and physical properties of Fe_xTaS_2 ($0.15 \leq x \geq 0.50$) compounds. *Journal of Solid State Chemistry*, 108(1):148–151, 1994.

[16] G. Kresse and D. Joubert. From ultrasoft pseudopotentials to the projector augmented-wave method. *Phys. Rev. B*, 59:1758–1775, Jan 1999.

[17] G. Kresse and J. Furthmüller. Efficient iterative schemes for ab initio total-energy calculations using a plane-wave basis set. *Phys. Rev. B*, 54:11169–11186, Oct 1996.

[18] John P. Perdew and Yue Wang. Accurate and simple analytic representation of the electron-gas correlation energy. *Phys. Rev. B*, 45:13244–13249, Jun 1992.

[19] S. L. Dudarev, G. A. Botton, S. Y. Savrasov, C. J. Humphreys, and A. P. Sutton. Electron-energy-loss spectra and the structural stability of nickel oxide: An LSDA+U study. *Phys. Rev. B*, 57:1505–1509, Jan 1998.

[20] Hendrik J. Monkhorst and James D. Pack. Special points for brillouin-zone integrations. *Phys. Rev. B*, 13:5188–5192, Jun 1976.

[21] Arash A. Mostofi, Jonathan R. Yates, Giovanni Pizzi, Young-Su Lee, Ivo Souza, David Vanderbilt, and Nicola Marzari. An updated version of wannier90: A tool for obtaining maximally-localised wannier functions. *Computer Physics Communications*, 185(8):2309–2310, 2014.

[22] John Stanley Griffith. *The theory of transition-metal ions*. Cambridge university press, 1961.

Chapter 6

Understanding Unusual Transport Properties in an Altermagnet CrSb

6.1 Introduction

Most materials conduct electricity in the same way in all directions of the crystal. Usually, they have either electron-based (n-type) or hole-based (p-type) conduction, whether they are metals or doped semiconductors. Many electronic devices, like transistors, LEDs, solar cells, and thermoelectrics, rely on combining p-type and n-type materials to control current flow. Interestingly, some metals and semiconductors have been found to show both p-type conduction in one direction and n-type conduction in another can be called direction-dependent conduction polarity.So far, only a few materials have been discovered with this property, including Be [1], Mg [2], Zn [2], Cd [2], Re [3], $CsBi_4Te_6$ [4], $NaSn_2As_2$ [5], $Al_{13}Co_4$ [6], $Tl_2Ba_2CuO_{6-x}$ [7], and Re_4Si_7 [8]. Additionally, there are no clear design rules for creating materials with direction-dependent conduction. With the availability of databases like the Materials Project and TE DesignLab, identifying band structure patterns for direction-dependent conduction could help researchers discover more materials with this unique property. The effective mass tensor of a charge carrier moving through a crystal lattice potential is given by:

$$m_{ij}^{*} = \hbar^2 \left[\frac{\partial^2 E}{\partial k_i \partial k_j} \right]^{-1}_{E=E_F} \tag{6.1}$$

Electrons have positive m_{ij}^{*} while holes have negative m_{ij}^{*}. Since the second derivative of a function determines its curvature, the sign of m_{ij}^{*} directly depends on the curvature of the corresponding energy band crossing the Fermi energy (E_F). The Fermi surface, which provides a geometric representation of all points in reciprocal space where the band energy equals E_F, encompasses all bands crossing E_F. A single band material can exhibit DDCP if its FS has concave and convex characters along different directions (see Fig. 6.1 a). This has been observed in $NaSn_2As_2$, [5], which has a hyperboloid-shaped Fermi surface that has both positive and negative curvatures (dependent on direction). The direction-dependent conduction polarity(DDCP) arising from a single carrier mechanism is termed “goniopolarity”, and the materials exhibiting it are called “goniopolar”. Another way to achieve direction-dependent conduction is through multicarrier mechanism ,

where electrons and holes live in distinct bands and dominate conduction along different crystallographic directions [9, 10]. This can be achieved when the Fermi surface exhibits highly anisotropic electron and hole pockets, such that the overall average curvature of the total Fermi surface has opposite signs along two different crystallographic directions. Although materials exhibiting direction dependent conduction polarity have recently gained attention as novel thermoelectric materials, [11–13], only a handful of such materials have been discovered to date. Additionally, inconsistencies often arise in the experimental characterization of reported direction dependent conduction polarity materials. For example, the Hall coefficient and Seebeck coefficient, whose signs are key indicators of direction dependent conduction polarity, may exhibit conflicting signs [5] or one of them may fail to demonstrate the direction-dependent opposite signs [12], which is the defining feature of direction dependent conduction polarity. In this chapter,[1] we explore the transport behavior of CrSb, a recently proposed altermagnetic compound. Altermagnets are a novel class of collinear magnetic materials characterized by zero net magnetization but spin-split electronic bands, [15, 16] making them promising candidates for spintronic applications. Recent experimental work by Banik Rai *et al.* [14] reported direction-dependent conduction polarity (DDCP) in CrSb, based on Hall effect and thermopower measurements. These results suggest that hole conduction dominates along the crystallographic *c*-axis, while electron transport is prevalent in the *ab*-plane of the hexagonal CrSb structure. To support and understand these findings, we carried out first-principles calculations of the Hall and Seebeck coefficients using Boltzmann transport theory within the density functional theory (DFT) framework. Our theoretical results qualitatively agree with the experimental observations. The DFT-derived Fermi surface reveals two hole pockets and one electron pocket, which contribute differently to conduction depending on direction. This anisotropic contribution gives rise to the observed DDCP in CrSb. Our calculations further indicate that this behavior is restricted to a narrow energy range near the Fermi level ($\Delta E \approx 14$ meV). Experimental studies also demonstrate that DDCP can be suppressed by doping [14].

6.2 Methodology

The electronic structure calculations were carried out using the Vienna *Ab initio* Simulation Package (VASP), which employs a plane-wave basis set along with the projector augmented-wave (PAW) method. [17–20] The exchange-correlation effects were treated

[1] Chapter 6 is based on publication [14]. The experimt is supported by Dr Nitesh Kumar and Banik Rai.

within the framework of the generalized gradient approximation (GGA) [21]. Structural optimization was performed by minimizing the total energy, keeping the lattice parameters fixed at the experimental values [22] corresponding to the NiAs-type crystal structure of CrSb in the $P6_3/mmc$ space group. The cutoff of in kinetic energy is used as 500 eV for the plane-wave expansion. Brillouin zone integrations were performed using a Monkhorst-Pack k-point mesh of $10 \times 10 \times 10$ [23]. The Seebeck and Hall coefficients were computed within the framework of semiclassical Boltzmann transport theory, using the relaxation time approximation and assuming a rigid band shift. For accurate interpolation of the DFT band structures, a dense k-mesh of $35 \times 35 \times 35$ was employed, as implemented in the BoltzTraP2 code [24]. Furthermore, the inverse effective mass (IEM) tensor was evaluated using B-spline interpolation of the DFT energy bands.

6.3 Result and Discussion

CrSb crystallizes in a hexagonal NiAs-type crystal structure, belonging to the $P6_3/mmc$ space group, and displays A-type antiferromagnetic ordering with a Néel temperature around 703 K [25, 26]. In this magnetic configuration, the Cr magnetic moments align along the c-axis, exhibiting ferromagnetic coupling within the ab-plane and antiferromagnetic coupling along the c-axis, as illustrated in Fig. 6.1 (a).

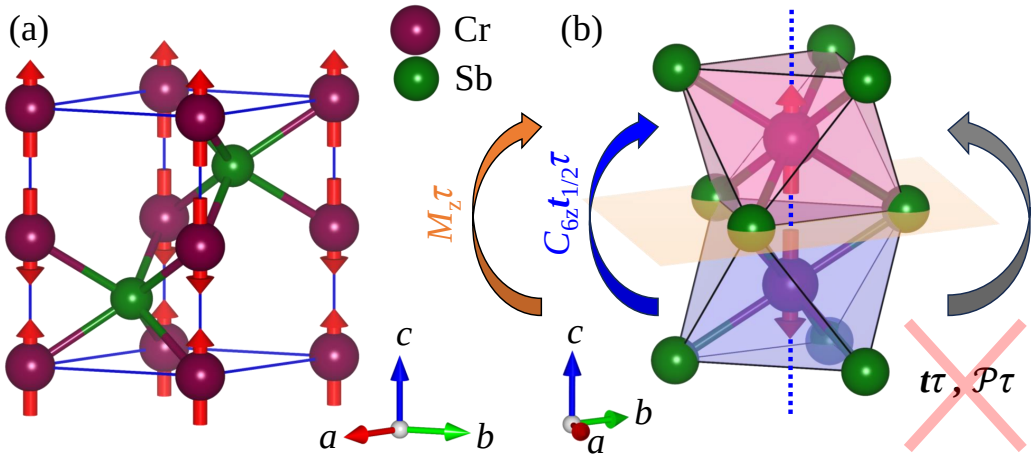

Figure 6.1: Crystal structure and sublattice transposing symmetries of CrSb. (a) Magnetic unit cell of CrSb showing A-type antiferromagnetic ordering of Cr-moments. (b) Sublattice transposing symmetries of CrSb showing that the opposite spin sublattices can not be connected throgh only lattice translation or inversion. They are instead connected by a horizontal mirror passing through Sb layer or a real space crystal rotation combined with half the lattice translation along the c-axis.

The anisotropic coordination of Sb atoms around the antiparallel Cr spins breaks the symmetry required to map one spin sublattice onto the other via a simple lattice translation or inversion operation, as shown in Fig. 6.1(b). However these sublattice can still be related by more complex symmetry operations,specifically, a six-fold rotation about the c-axis (C_{6z}) followed by a half-unit translation along the c-axis ($\boldsymbol{t}_{1/2} = (0, 0, c/2)$), or a mirror reflection through the Sb atomic layer (M_z), can map one sublattice onto the other. When combined with time-reversal symmetry (τ), these generate the true sublattice-exchanging symmetries of the crystal: $C_{6z}\boldsymbol{t}_{1/2}\tau$ and $M_z\tau$. These symmetries enforce the presence of four spin-degenerate nodal planes in the Brillouin zone (BZ), as depicted in Fig. 6.2 (a). Outside these high-symmetry planes, the energy bands exhibit pronounced non-relativistic spin splitting due to lifted spin degeneracy, shown in Fig. 6.2 (b).

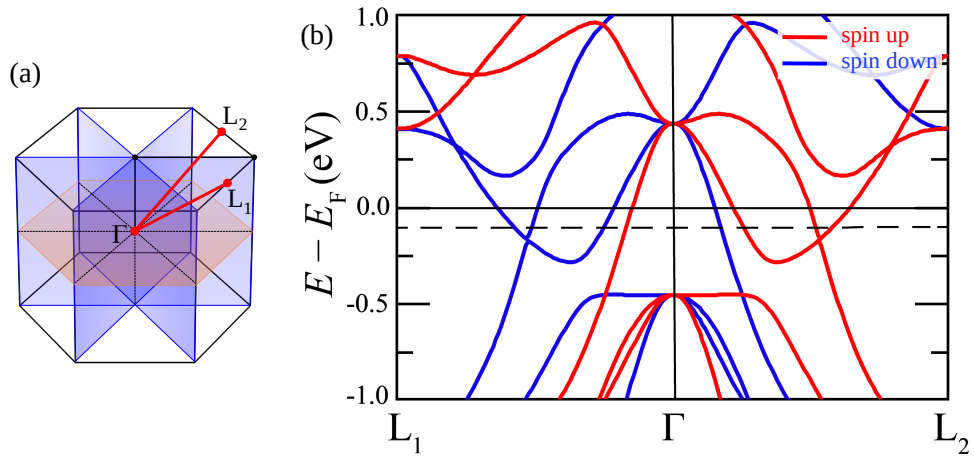

Figure 6.2: (a) Brillouin zone (BZ) of CrSb showing four spin-degenerate nodal planes. (b) Band structure of CrSb calculated without spin-orbit coupling (SOC). A significant altermagnetic splitting can be observed. The dashed horizontal line represents the experimental Fermi energy (E'_F).

Next, we investigated the transport properties of CrSb using our electronic structure calculations by computing the thermopower and the Hall coefficient tensor near the Fermi energy within the DFT framework, employing the Boltzmann transport equations and the relaxation-time approximation. Figure 6.3 (a) displays the band structure of CrSb computed along high-symmetry directions in the Brillouin zone (see inset), with spin-orbit coupling (SOC) included. These paths lie within spin-degenerate nodal planes, which are protected by the sublattice-exchanging symmetries of the CrSb crystal. Consequently, in the absence of SOC, the bands along these directions do not exhibit the spin splitting characteristic of altermagnets. Near the Fermi level, three bands labeled #1, #2, and #3 primarily govern the transport properties.

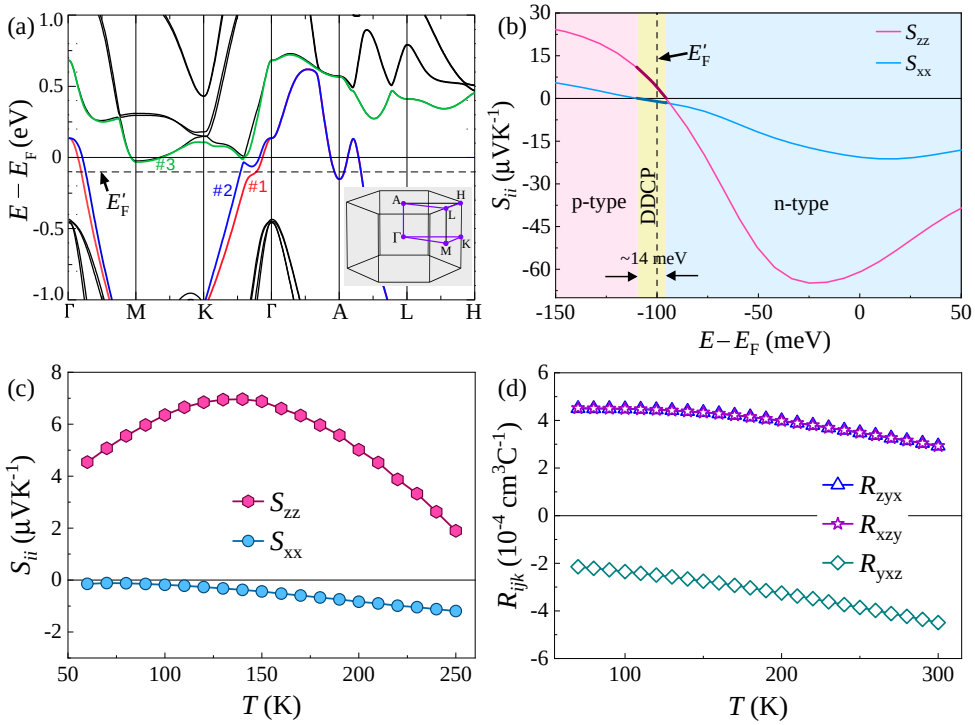

Figure 6.3: Results of theoretical calculations on CrSb. a Band structure along high-symmetry paths (see inset) of the BZ with SOC turned on. The bands crossing the shifted E'_F (dashed line) are highlighted in color and labeled numerically. (b) In-plane (S_{xx}) and cross-plane (S_{zz}) Seebeck coefficients at 100 K as a function of change in Fermi energy, showing the DDCP behavior existing within a small energy window. The black dashed line represents the shifted Fermi energy E'_F (see text). (c) Temperature dependence of S_{xx} and S_{zz} calculated at E'_F. (d) Temperature dependence of the Hall coefficient components calculated at E'_F.

The Seebeck coefficient tensor was evaluated as a function of the Fermi energy around E_F at 100 K, as shown in Fig. 6.3 (b). Our calculations reveal a pronounced anisotropy in the Seebeck coefficient upon slightly shifting the Fermi energy to E'_F, with the effect persisting over a narrow energy range of approximately 14 meV. This shift corresponds to hole doping of roughly 0.13 carriers per unit cell. The sign of the Seebeck coefficient captures the direction-dependent conduction polarity in CrSb. The Fermi surface (FS) computed at E'_F (Fig. 6.5) matches well with those observed in ARPES experiments on CrSb [27–29]. This agreement supports the idea that small deviations from ideal stoichiometry in real samples effectively shift the Fermi level below the theoretical value. The trends of the in-plane (S_{xx}) and cross-plane (S_{zz}) components of the Seebeck coefficient with temperature is shown in Fig. 6.3 (c). Over the studied temperature range, the magnitude of S_{xx} increases gradually and monotonically with temperature, remaining negative throughout.

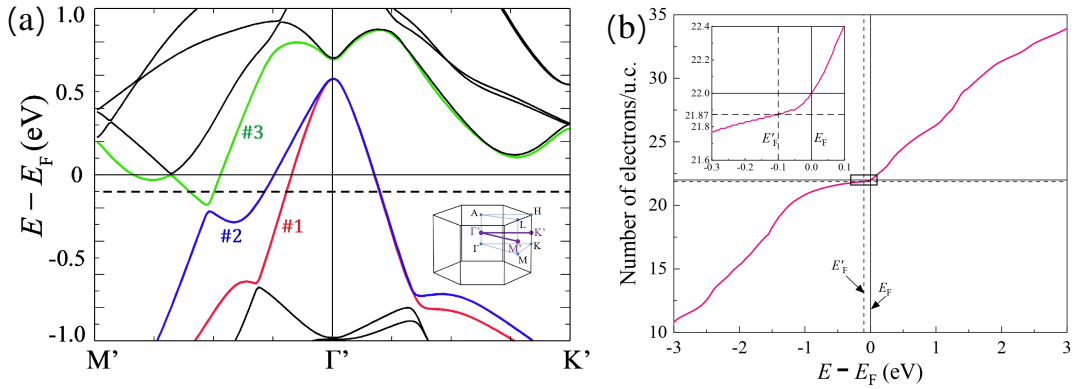

Figure 6.4: (a) Band dispersion (with SOC turned on) along high symmetry lines for a particular fixed plane $k_z = 0.2\pi/c$. (b) Number of electrons per unit cell as a function of energy.

In contrast, S_{zz} is consistently positive, first increasing with temperature, reaching a broad maximum, and subsequently decreasing. These trends qualitatively agree with the experimental findings reported by Banik Rai *et al.* [14]. Although the theoretical temperature dependence does not quantitatively reproduce experimental results, this discrepancy likely arises from the limitations of the approximations used in our calculations. In particular, the influence of phonon has been neglected, including contributions from electron-phonon interactions and phonon drag effects [24, 30, 31]. Figure 6.3 (d) displays the temperature dependence of the Hall coefficient components. The component R_{yxz} remains negative across all temperatures considered, while R_{xzy} and R_{zyx} are consistently positive. Furthermore, the equality $R_{xzy} = R_{zyx}$, which follows from the magnetic point group symmetry of CrSb, is preserved in our calculations. Although electron and hole carriers usually contribute Seebeck coefficients of opposite sign, the sign reversal observed here can also result from anisotropic contributions to different tensor components of the Seebeck coefficient [5, 10]:

$$S_{ii} = -\frac{\pi^2 K_B^2 T}{3\,|e|}\left[\frac{1}{n(E)}\frac{dn(E)}{dE} + \frac{1}{\tau_{ii}(E)}\frac{d\tau_{ii}}{dE} + m^*_{ii}\frac{d}{dE}\left(\frac{1}{m^*_{ii}}\right)\right]_{E=E_F} \tag{6.2}$$

Here, $n(E)$ and $\tau_{ii}(E)$ are the energy-dependent carrier concentration and relaxation-time tensor. Although $n(E)$ is a scalar and cannot cause anisotropy in the sign of S_{ii} and $\tau_{ii}(E)$ is a tensor and can have different values in different directions. However, the quantity $\dfrac{1}{\tau_{ii}(E)}\dfrac{d\tau_{ii}}{dE}$, which appears in the expression of S_{ii}, depends on the nature of the scattering mechanism of the conduction electrons and must have an isotropic sign in a clean single crystal having negligible defects. In our theoretical calculation $\tau_{ii}(E)$ is assumed to be constant. Thus, the anisotropy in the sign of S_{ii} must arise from m^*_{ii} as the

quantity $\frac{d}{dE}\left(\frac{1}{m^*_{ii}}\right)$ is always negative for energy bands with cosine-like dispersion [5]. To understand the mechanism of direction dependent conduction polarity in CrSb, we calculated the Fermi surface at E'_{F}, as shown in Fig. 6.3 a. Three distinct Fermi pockets labeled α, β, and γ correspond to three different bands (#1, #2, and #3, respectively) that cross E'_{F}. Although band #3 does not cross E'_{F} at $k_z = 0$ plane, it crosses E'_{F} at some finite value of k_z, as shown in Fig. 6.4 b. The α and β pockets appear to be nearly hyperboloid in shape, meaning they are closed in the $k_{\mathrm{x}} - k_{\mathrm{y}}$ plane and open along the k_{z} direction, apparently exhibiting both convex and concave features. Each of these pockets includes a small hemispherical sub-pocket around A point of the Brillouin zone. The γ pocket consists of 12 symmetry-related similar sub-pockets. These sub-pockets are closed and have an anisotropic, bead-like shape, elongated along the k_{z}-direction. In the presence of multiple Fermi pockets with varying geometries, including hyperboloid-like and anisotropic features, the mechanism of direction dependent conduction polarity in CrSb may not be determined simply by observing the shape of the Fermi surface. We therefore investigated the origin of this behavior by calculating the inverse effective mass (IEM) tensor, $m^{*^{-1}}_{ij}$, at each point of the Fermi surface. This involves the curvature of the electronic band dispersion at that point, as described by Eq. (6.1).

Table 6.1: Average normalized inverse effective mass (IEM) values for the individual Fermi pockets α, β, γ, and the entire Fermi surface along different directions.

Fermi pockets	$\left\langle \frac{m_e}{m^*_{\mathrm{xx}}} \right\rangle$	$\left\langle \frac{m_e}{m^*_{\mathrm{yy}}} \right\rangle$	$\left\langle \frac{m_e}{m^*_{\mathrm{zz}}} \right\rangle$
α	-1.65	-1.63	-0.47
β	-1.16	-1.15	-2.33
γ	4.42	4.37	4.55
All over Fermi Surface	0.04	0.05	-1.56

Fig. 6.5 b-d shows the distribution of the diagonal components of the inverse effective mass tensor, normalized by the free electron mass (m_e), on the three Fermi pockets. The pockets α and β host both have positive and negative distributions of inverse effective mass along both out of plane (z) and in-plane (x and y) directions, with negative inverse effective mass dominating the overall distribution. Notably, the small hemispherical α and β sub-pockets also display positive inverse effective mass along all directions, indicating that they are electron pockets as well. Table 6.1 presents the inverse effective mass values averaged over each of the three individual Fermi pockets and the entire Fermi surface along x, y, and z-directions. From this table, it is evident that both the α and β pockets do not produce direction dependent conduction polarity on their own (goniopolarity) as they have an overall hole character (negative effective mass) along all directions.

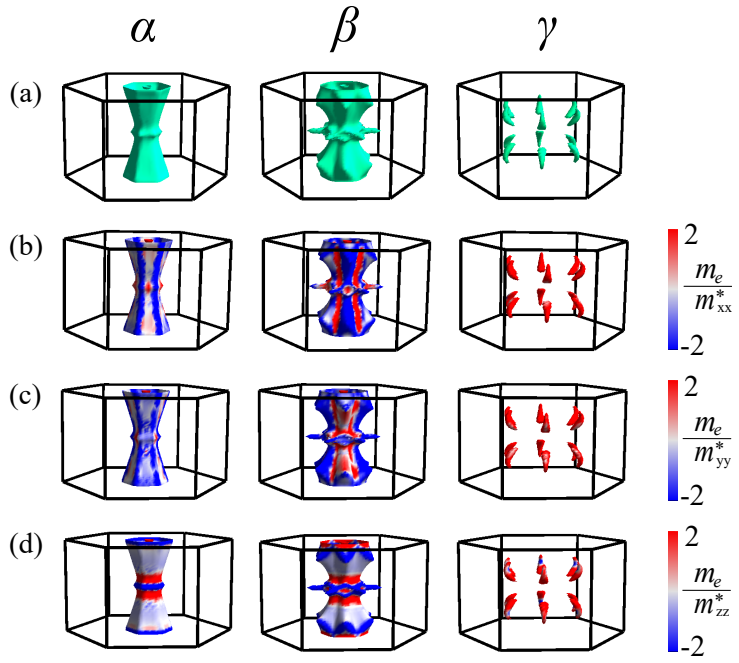

Figure 6.5: (a) Calculated Fermi pockets α, β, and γ associated with three distinct bands #1, #2, and #3, respectively, that cross E'_F. (b)-(d) The distribution of IEM strength on the Fermi pockets along (b) x-, (c) y-, and (d) z-directions.

The average inverse effective mass values for the γ pocket along all directions are positive which means it has overall electron character along all the directions. When the entire Fermi surface is considered, the in-plane average IEM values become positive, while the cross-plane average IEM value becomes negative, giving rise to direction-dependent conduction polarity. This suggests that direction-dependent conduction polarity in CrSb arises from the multicarrier mechanism, where in-plane conduction is dominated by electrons and cross-plane conduction is dominated by holes.

6.4 Conclusion

In summary, we have investigated the anisotropic transport properties of the altermagnet CrSb. Both the Hall and Seebeck coefficients indicate that CrSb exhibits direction-dependent carrier polarity, with in-plane conduction dominated by electrons and cross-plane conduction dominated by holes. Our DFT calculations, based on the Boltzmann transport equation and the relaxation-time approximation, qualitatively support the experimental results. We show that the direction-dependent carrier polarity in CrSb arises from a multicarrier mechanism, identifying two hole pockets and one electron pocket as the dominant contributors to cross-plane and in-plane conduction, respectively. The

emergence of direction-dependent conduction polarity in CrSb is a consequence of its unique Fermi surface geometry, shaped by altermagnetic spin splitting. However, it is important to emphasize that altermagnetic spin splitting does not inherently lead to direction-dependent carrier polarity in all materials. In the case of CrSb, the particular Fermi surface geometry happens to facilitate direction-dependent carrier polarity, but this behavior is not a universal feature of altermagnets. Moreover, our calculations predict that the direction-dependent conduction polarity in CrSb is fragile and can be suppressed by a small amount of doping. This prediction is validated by experimental results from Banik Rai et al [14], which observed the disappearance of direction-dependent conduction polarity in minimally hole-doped $Cr_{0.98}V_{0.02}Sb$.

Bibliography

[1] Alexandr Trofimovich Burkov and Marat Victorovich Vedernikov. Anomalous anisotropy of high temperature of thermo-emf in beryllium. *Fizika Tverdogo Tela*, 28(12):3737–3739, 1986.

[2] V.A. Rowe and P.A. Schroeder. Thermopower of mg, cd and zn between 1.2° and 300°k. *Journal of Physics and Chemistry of Solids*, 31(1):1–8, 1970.

[3] Alexandr Trofimovich Burkov, Marat Victorovich Vedernikov, VA Elenskii, and GP Kovtun. Anisotropy of thermo-emf and electroconductivity of high purity rhenium. *Fizika Tverdogo Tela*, 28(3):785–788, 1986.

[4] Duck-Young Chung, Tim P. Hogan, Melissa Rocci-Lane, Paul Brazis, John R. Ireland, Carl R. Kannewurf, Marina Bastea, Ctirad Uher, and Mercouri G. Kanatzidis. A new thermoelectric material: Csbi4te6. *Journal of the American Chemical Society*, 126(20):6414–6428, May 2004.

[5] Bin He, Yaxian Wang, Maxx Q. Arguilla, Nicholas D. Cultrara, Michael R. Scudder, Joshua E. Goldberger, Wolfgang Windl, and Joseph P. Heremans. The fermi surface geometrical origin of axis-dependent conduction polarity in layered materials. *Nat. Mater.*, 18:568–572, 2019.

[6] J. Dolinšek, M. Komelj, P. Jeglič, S. Vrtnik, D. Stanić, P. Popčević, J. Ivkov, A. Smontara, Z. Jagličić, P. Gille, and Yu. Grin. Anisotropic magnetic and transport properties of orthorhombic $al_{13}co_4$. *Phys. Rev. B*, 79:184201, May 2009.

[7] W. Kiehl, H.M. Duan, and A.M. Hermann. Anisotropic seebeck coefficient in $Tl_2Ba_2CuO_{6-\delta}$ single crystals. *Physica C: Superconductivity*, 253(3):271–278, 1995.

[8] Shunta Harada, Katsushi Tanaka, Kyosuke Kishida, and Haruyuki Inui. Crystal structure and thermoelectric properties of resi1.75 based alloys. In *Advanced Materials and Processing*, volume 26 of *Advanced Materials Research*, pages 197–200. Trans Tech Publications Ltd, 12 2007.

[9] Karl G. Koster, Ziling Deng, Curtis E. Moore, Joseph P. Heremans, Wolfgang Windl, and Joshua E. Goldberger. Axis-dependent conduction polarity in WSi_2 single crystals. *Chem. Mater.*, 35:4228–4234, 2023.

[10] Yaxian Wang, Karl G. Koster, Andrew M. Ochs, Michael R. Scudder, Joseph P. Heremans, Wolfgang Windl, and Joshua E. Goldberger. The chemical design principles for axis-dependent conduction polarity. *J. Am. Chem. Soc.*, 142:2812–2822, 2020.

[11] Yang Tang, Boya Cui, Chuanle Zhou, and Matthew Grayson. p×n-type transverse thermoelectrics: A novel type of thermal management material. *J. Electron. Mater.*, 44:2095–2104, 2015.

[12] Hikari Manako, Shoya Ohsumi, Yoshiki J Sato, R Okazaki, and D Aoki. Large transverse thermoelectric effect induced by the mixed-dimensionality of fermi surfaces. *Nat. Commun.*, 15(1):3907, 2024.

[13] Michael R. Scudder, Bin He, Yaxian Wang, Akash Rai, David G. Cahill, Wolfgang Windl, Joseph P. Heremans, and Joshua E. Goldberger. Highly efficient transverse thermoelectric devices with Re_4Si_7 crystals. *Energy Environ. Sci.*, 14(7):4009–4017, 2021.

[14] Banik Rai, Krishnendu Patra, Satyabrata Bera, Sk Kalimuddin, Kakan Deb, Mintu Mondal, Priya Mahadevan, and Nitesh Kumar. Direction-dependent conduction polarity in altermagnetic CrSb. *Advanced Science*, n/a(n/a):2502226, 2025.

[15] Libor Šmejkal, Jairo Sinova, and Tomas Jungwirth. Beyond conventional ferromagnetism and antiferromagnetism: A phase with nonrelativistic spin and crystal rotation symmetry. *Phys. Rev. X*, 12(3):031042, 2022.

[16] Libor Šmejkal, Jairo Sinova, and Tomas Jungwirth. Emerging research landscape of altermagnetism. *Phys. Rev. X*, 12(4):040501, 2022.

[17] P. E. Blöchl. Projector augmented-wave method. *Phys. Rev. B*, 50:17953–17979, 1994.

[18] G. Kresse and J. Hafner. Ab initio molecular dynamics for liquid metals. *Phys. Rev. B*, 47:558–561, 1993.

[19] G. Kresse and J. Hafner. Ab initio molecular-dynamics simulation of the liquid-metal-amorphous-semiconductor transition in germanium. *Phys. Rev. B*, 49:14251–14269, 1994.

[20] G. Kresse and J. Furthmüller. Efficient iterative schemes for ab initio total-energy calculations using a plane-wave basis set. *Phys. Rev. B*, 54:11169–11186, 1996.

[21] John P. Perdew, Kieron Burke, and Matthias Ernzerhof. Generalized gradient approximation made simple. *Phys. Rev. Lett.*, 77:3865–3868, 1996.

[22] A. Kallel, H. Boller, and E.F. Bertaut. Helimagnetism in MnP-type compounds: MnP, FeP, CrAs and $CrAs_{1-x}Sb_x$ mixed crystals. *J. Phys. Chem. Solids*, 35(9):1139–1152, 1974.

[23] Hendrik J. Monkhorst and James D. Pack. Special points for Brillouin-zone integrations. *Phys. Rev. B*, 13:5188–5192, 1976.

[24] Georg K.H. Madsen, Jesús Carrete, and Matthieu J. Verstraete. BoltzTraP2, a program for interpolating band structures and calculating semi-classical transport coefficients. *Comput. Phys. Commun.*, 231:140–145, 2018.

[25] A. I. Snow. Neutron diffraction investigation of the atomic magnetic moment orientation in the antiferromagnetic compound CrSb. *Phys. Rev.*, 85(2):365–365, 1952.

[26] Jibao Yuan, Yuzhu Song, Xianran Xing, and Jun Chen. Magnetic structure and uniaxial negative thermal expansion in antiferromagnetic CrSb. *Dalton Trans.*, 49:17605–17611, 2020.

[27] Jianyang Ding, Zhicheng Jiang, Xiuhua Chen, Zicheng Tao, Zhengtai Liu, Tongrui Li, Jishan Liu, Jianping Sun, Jinguang Cheng, Jiayu Liu, Yichen Yang, Runfeng Zhang, Liwei Deng, Wenchuan Jing, Yu Huang, Yuming Shi, Mao Ye, Shan Qiao, Yilin Wang, Yanfeng Guo, Donglai Feng, and Dawei Shen. Large band splitting in g-wave altermagnet CrSb. *Phys. Rev. Lett.*, 133(20):206401, 2024.

[28] Meng Zeng, Ming-Yuan Zhu, Yu-Peng Zhu, Xiang-Rui Liu, Xiao-Ming Ma, Yu-Jie Hao, Pengfei Liu, Gexing Qu, Yichen Yang, Zhicheng Jiang, Kohei Yamagami, Masashi Arita, Xiaoqian Zhang, Tian-Hao Shao, Yue Dai, Kenya Shimada, Zhengtai Liu, Mao Ye, Yaobo Huang, Qihang Liu, and Chang Liu. Observation of spin splitting in room-temperature metallic antiferromagnet CrSb. *Adv. Sci.*, 11(43):2406529, 2024.

[29] Guowei Yang, Zhanghuan Li, Sai Yang, Jiyuan Li, Hao Zheng, Weifan Zhu, Ze Pan, Yifu Xu, Saizheng Cao, Wenxuan Zhao, Anupam Jana, Jiawen Zhang, Mao Ye, Yu Song, Lun-Hui Hu, Lexian Yang, Jun Fujii, Ivana Vobornik, Ming Shi, Huiqiu Yuan, Yongjun Zhang, Yuanfeng Xu, and Yang Liu. Three-dimensional mapping of the altermagnetic spin splitting in CrSb. *Nat. Commun.*, 16(1):1442, 2025.

[30] Raveena Gupta, Baljinder Kaur, Jesús Carrete, and Chandan Bera. A theoretical model of the thermoelectric properties of SnS_xSe_{1-x} and how to further enhance its thermoelectric performance. *J. Appl. Phy.*, 126(22):225105, 2019.

[31] VG Vaks, AV Trefilov, and SV Fomichev. Singularities of resistivity and thermoelectric power of metals in phase transitions of order $2\frac{1}{2}$. *Th. Eksp. Teor. Fiz*, 80:1613, 1981.

Chapter 7

Multiple Lifshitz transitions in chiral Weyl semimetal RhSi-Origin and Consequences

7.1 Introduction

Over the last several years, Weyl semimetals have emerged as a prominent topic in condensed matter physics. A Weyl semimetal features discrete points near the Fermi level, known as Weyl points, where bands with opposite curvature cross each other [1–3]. These band crossing points are topologically protected, carry non-zero Chern numbers, and appear in pairs of opposite chirality. They are connected in momentum space by surface states known as Fermi arcs. The emergence of Weyl nodes requires the breaking of either time-reversal symmetry or inversion symmetry. Typically, these nodes are characterized by two-fold band degeneracy and correspond to quasiparticles that behave like spin-$\frac{1}{2}$ fermions. Experimental realizations of such Weyl nodes have been reported in a variety of materials, notably in non-centrosymmetric transition metal monopnictides such as TaAs, NbAs, TaP, and NbP [4–10], as well as in magnetic systems including $Co_3Sn_2S_2$ [11, 12] and Co_2MnGa [13]. A typical characteristic of these Weyl semimetals is the appearance of short Fermi arcs, indicating that the topologically nontrivial surface states persist only over a narrow energy window. However these materials have not been ideal platforms to explore many-body interactions involving topological boundary states due to the overlap with trivial electronic states within the same energy window [14]. The RhSi family of compounds (including RhSi, CoSi, RhGe, and CoGe), which crystallize in a chiral cubic structure with space group $P2_13$ [15, 16], have recently attracted considerable attention as promising candidates. First-principles calculations of their electronic structure reveal that the bulk hosts Weyl nodes with degeneracies higher than two. These nodes display a six-fold degeneracy (3×2) at the Brillouin zone center (Γ point) when spin-orbit coupling is neglected. Upon inclusion of spin-orbit interactions, the degeneracy is lifted, resulting in chiral fermionic excitations that are four-fold degenerate at the Fermi energy. These quasiparticles can be interpreted as a mixture of two spin-3/2 and two spin-1/2 Weyl fermions. At the zone boundary (the R point), the 4×2-fold degenerate Weyl node evolves into a six-fold degenerate double spin-1 fermion under the influence

of spin-orbit coupling [17–19]. These materials exhibit a wide momentum-space energy window characterized by nontrivial topological features, along with long Fermi arcs on their surfaces [17,18,20–22]. Such characteristics make them especially suitable for investigating many-body effects linked to topological surface states [14,20]. Furthermore, their unique electronic structures make them attractive candidates for realizing the circular photogalvanic effect [17,23–27]. The presence of unconventional chiral fermions in these systems also opens a path for experimental investigations into materials that support topological surface modes, as well as the possibility of observing bulk chiral transport phenomena [22,28–30].

The topological characteristics of multifold Weyl semimetals have been extensively studied through theoretical methods, especially within the density functional theory (DFT) framework [31,32]. Recent studies combining scanning tunneling microscopy (STM) and density functional theory (DFT) calculations have revealed a one-dimensional charge density wave (CDW) on the (001) surface of CoSi [14,33]. The observed CDW in this topologically nontrivial system is considered to result from electron-electron interactions. Some studies using density functional theory in conjunction with dynamical mean-field theory (DFT+DMFT) for CoSi have reported notable modifications in the band structure including the simultaneous presence of coherent quasiparticle peaks and incoherent spectral weight [34,35]. A substantial gap still exists in the current literature concerning a direct link between unconventional chiral fermions and electron correlation effects.

In this chapter,[1] we focus on RhSi as a prototypical member of the RhSi family to investigate the role of local electron correlations, implemented through GGA+U calculations. To obtain a reasonable value for the on-site Coulomb interaction U on the Rh d orbitals, which dominate the low-energy electronic structure from approximately 6 eV below to 3.5 eV above the Fermi level, we employed the constrained random phase approximation (cRPA) method [37]. Our results reveal a nontrivial electronic structure featuring a double-hump dispersion near the Fermi energy, which suggests the occurrence of multiple successive Lifshitz transitions around the Weyl node at the Γ point, triggered by small shifts in the chemical potential. A Lifshitz transition, driven by a continuous variation of an external parameter such as doping or pressure, results in a transformation iof the topology of the Fermi surface [38]. To simulate such effects, we modeled hole and electron doping via rigid shifts of the chemical potential and computed the Seebeck coefficient, a thermodynamic quantity known to exhibit discontinuities at such transitions [38,39]. Furthermore, using a realistic tight-binding Hamiltonian, we traced the microscopic origin of the observed Lifshitz transition to the interplay between Rh d–Rh d and Rh d–Si p

[1] Chapter 7 is based on publication [36]. The cRPA calculation is done by Prof. Ferdi Ferdi Aryasetiawan and Christiansson Viktor.

hopping interactions. This transformation is particularly relevant in the context of Weyl semimetals [40, 41], as Lifshitz transitions near Weyl points are often linked to emergent correlated electronic phases, such as unconventional superconductivity [42, 43].

7.2 Methodology

We employed the experimentally determined simple cubic crystal structure of RhSi, belonging to the non-centrosymmetric space group $P2_13$ [15], for our first-principles calculations. The electronic structure calculations were carried out using a plane-wave basis set within the density functional theory (DFT) formalism, utilizing the Vienna *ab initio* Simulation Package (VASP) [44–47]. The interaction between the valence electrons and the ionic cores was modeled using the projector augmented-wave (PAW) approach. To describe the exchange-correlation potential, we employed the generalized gradient approximation (GGA) as proposed by Perdew, Burke, and Ernzerhof [48]. Spin-orbit coupling (SOC) effects were explicitly included, and local electronic correlations were treated via the GGA+U method following the Dudarev approach [49], where an effective Hubbard U_{eff} was applied to the Rh d states. The value of U_{eff} was obtained from We employed the experimentally determined simple cubic crystal structure of RhSi, belonging to the non-centrosymmetric space group $P2_13$ [15], for our first-principles calculations. The electronic structure was computed using a plane-wave basis set within the framework of density functional theory, as implemented in the Vienna *ab initio* simulation package (VASP) [44–47]. The interaction between valence electrons and ionic cores was treated using the projector augmented wave (PAW) method. For the exchange-correlation potential, we adopted the generalized gradient approximation (GGA) as formulated by Perdew, Burke, and Ernzerhof [48]. Spin-orbit coupling (SOC) effects were explicitly included, and local electronic correlations were treated via the GGA+U method following the Dudarev approach [49], where an effective Hubbard U_{eff} was applied to the Rh d states. The value of U_{eff} was obtained using the constrained random phase approximation(cRPA) [37].

Spread of the Wannier functions (Å)^2		
Atomic Orbital	Largest spread	Smallest spread
Rh-d	1.44	1.25
Si-p	2.66	2.66

Table 7.1: The range of spreads of the Wannier functions for Rh d and Si p orbitals.

All internal atomic positions were fully relaxed by minimizing the total energy, while maintaining the lattice parameters at their experimentally determined values. A kinetic

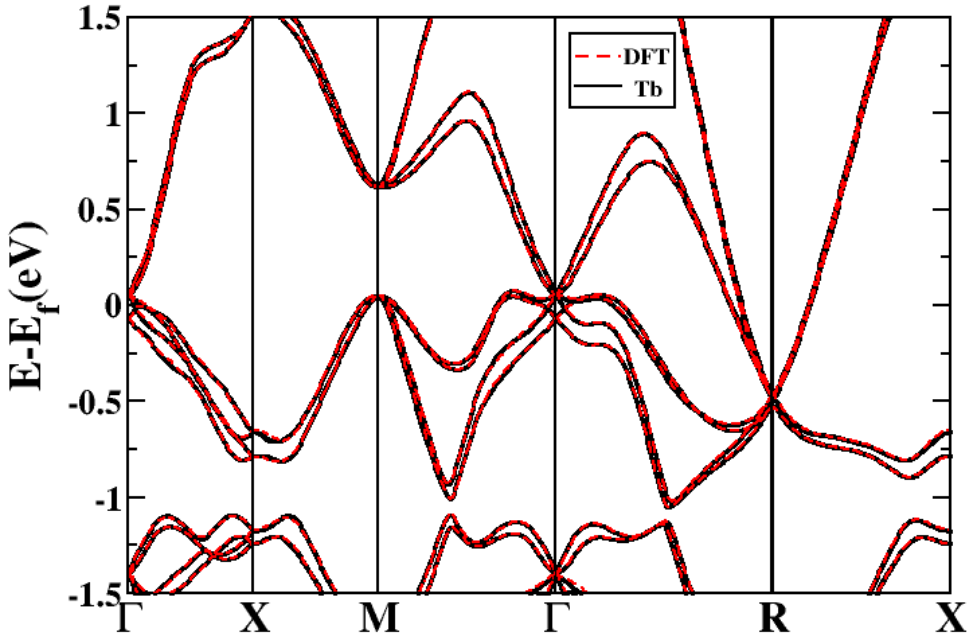

Figure 7.1: Comparison of the band dispersions obtained from *ab initio* calculations (red dashed line) with those from the tight-binding model (black solid line).The *ab initio* calculations were carried out within GGA+U+SOC using a U=2.5 eV on the Rh d states.

energy cutoff of 400 eV was applied to truncate the plane-wave basis set, ensuring convergence of the total energy. For Brillouin zone sampling, a $9\times9\times9$ Monkhorst-Pack k-point grid [50] was employed, offering adequate resolution for precise electronic structure evaluations. To gain further insight into the contributions of various orbital hybridizations influencing the low-energy electronic structure, we mapped the DFT-derived band structure onto a tight-binding Hamiltonian built using maximally localized Wannier functions (MLWFs), employing Rh d and Si p orbitals as the basis set. The matrix elements of the tight-binding Hamiltonian were obtained using the wannier90-VASP interface [51,52]. The model provides a good agreement with the first-principles band structure, ensuring that the chosen Wannier basis accurately represents the relevant states near the Fermi level. We thus employ this Hamiltonian for subsequent analysis. The Berry curvature distribution was computed within the tight-binding framework using WannierTool [53].

To investigate thermoelectric behavior, specifically the Seebeck coefficient, we introduced doping effects by applying a rigid shift to the chemical potential, effectively representing electron or hole doping. The Seebeck coefficient was evaluated using semiclassical Boltzmann transport theory, wherein the DFT band structure was interpolated onto a dense $35\times35\times35$ k-point mesh. These computations were carried out within the constant relaxation time approximation utilizing the BoltzTraP2 package [54]. The Seebeck

coefficient at temperature T is given by [55, 56]:

$$S = \frac{e}{T\sigma} \int_{-\infty}^{\infty} \Xi(E,T)\,(E-\mu) \left(-\frac{\partial f_0}{\partial E}\right) dE, \tag{7.1}$$

where μ represents the chemical potential, f_0 is the equilibrium Fermi-Dirac distribution, e denotes the elementary charge, and σ is the electrical conductivity, expressed as:

$$\sigma = e^2 \int_{-\infty}^{\infty} \Xi(E,T) \left(-\frac{\partial f_0}{\partial E}\right) dE. \tag{7.2}$$

Here, $\Xi(E,T)$ is the energy- and temperature-dependent transport distribution function, defined by:

$$\Xi(E,T) = \int \mathbf{v_k} \otimes \mathbf{v_k}\, \tau_{\mathbf{k}}\, \delta(E - E_{\mathbf{k}})\, \frac{d\mathbf{k}}{8\pi^3}, \tag{7.3}$$

where $\mathbf{v_k}$ is the group velocity associated with the electronic state $\mathbf{k}$, $E_{\mathbf{k}}$ refers to the corresponding band energy (Kohn-Sham eigenvalue), and $\tau_{\mathbf{k}}$ is the relaxation time for state $\mathbf{k}$.

7.3 Result and Discussion

Figure 7.2 displays the low-energy band structure of RhSi, derived from GGA+U+SOC computations. Panel (a) of Fig. 7.2 illustrates the computed band structure along selected high-symmetry paths for $U = 0$. Without incorporating spin-orbit coupling (SOC), the system exhibits multifold Dirac-like band crossings, including an eightfold degeneracy at the R point and a sixfold degeneracy at the Γ point. When SOC is taken into account, these degeneracies are partially lifted, yielding sixfold and fourfold degeneracies at the R and Γ points, respectively. Furthermore, a nearly dispersionless band appears near the Fermi level along the M–Γ–R direction. These results are consistent with previous findings [17]. As phenomena associated with correlated systems, such as charge density waves, has been observed on the [0,0,1] surface of CoSi [14, 33], we proceed to determine an appropriate value of U for RhSi using the constrained random phase approximation (cRPA). These calculations yield an effective on-site Coulomb interaction of $U_{eff} = 2.5$ eV. Incorporating U_{eff} in our GGA+U calculations, we obtain the band dispersions shown in Fig. 7.2 (b). The inclusion of a finite U preserves the Weyl points in the electronic structure and maintains all underlying crystal symmetries. However, significant modifications arise in the band dispersion near the Γ point, particularly along the M–Γ–R path. Whereas the U = 0 case exhibits a nearly flat band in this region, the U = 2.5 eV case reveals a distinct double-hump structure within a very small energy window around

the Fermi energy. The emergence of this double-hump feature indicates the possibility of multiple Lifshitz transitions [57, 58], which could be driven by external parameters such as pressure or doping.

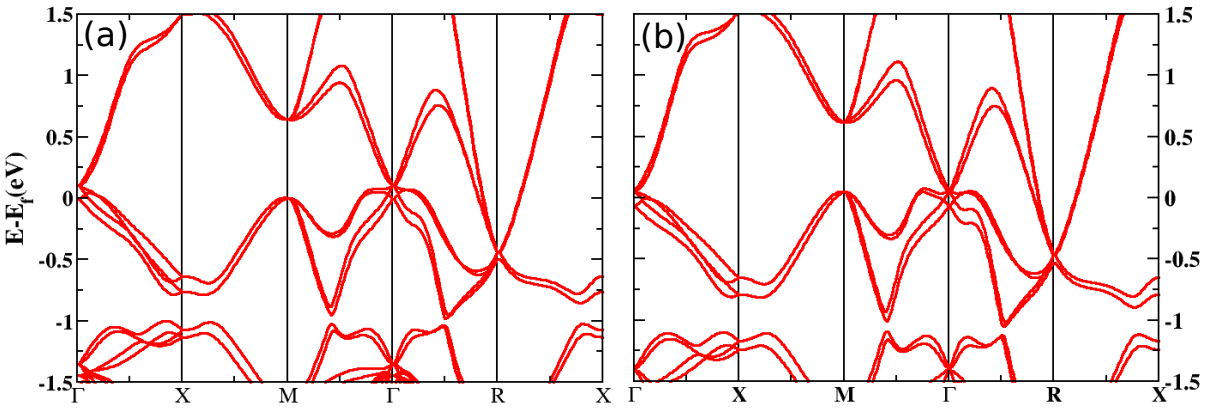

Figure 7.2: The electronic band structures computed using GGA+U+SOC for (a) U = 0.0 eV and (b) U = 2.5 eV applied to the Rh d orbitals. The Fermi level is indicated by E_{f}. .

In the current scenario, the Lifshitz transition is induced by adjusting the chemical potential through doping hole or electrons. Within the static band approximation, three distinct Fermi level positions,labeled I, II, and III,corresponding to three distinct doping levels, are illustrated in Fig. 7.3 (a). Label I corresponds to hole doping of 0.05 carriers per formula unit, while labels II and III represent electron doping of 0.04 and 0.09 carriers, respectively. Fermi levels I and II lie close to the Weyl point at the Γ point, whereas levels II and III span the peaks of the double-hump structure observed near the Fermi energy. Figures 7.3 (b–d) display the corresponding Fermi surfaces for the three doping concentrations. A clear transition in the Fermi surface topology can be seen across the three scenarios. At label I, a closed hole pocket is observed around the Γ point. For label II, this pocket opens up, forming an extended hole-like feature. By label III, the hole pocket has vanished, and a widened electron pocket appears. These topological changes in the Fermi surface across the three doping levels mark consecutive Lifshitz transitions.

Lifshitz transitions can be probed by Various thermodynamic measurements , among which the Seebeck coefficient is particularly sensitive to changes in the Fermi surface topology. In Fig. 7.4, we present the Seebeck coefficient as a function of temperature for different levels of carrier doping. For case I (0.05 holes doped), the Seebeck coefficient is positive and approximately linear within the considered temperature range, suggesting that holes dominate the charge transport. In region II (0.04 electrons doped), the Seebeck coefficient remains positive but displays a distinct temperature dependence. It increases

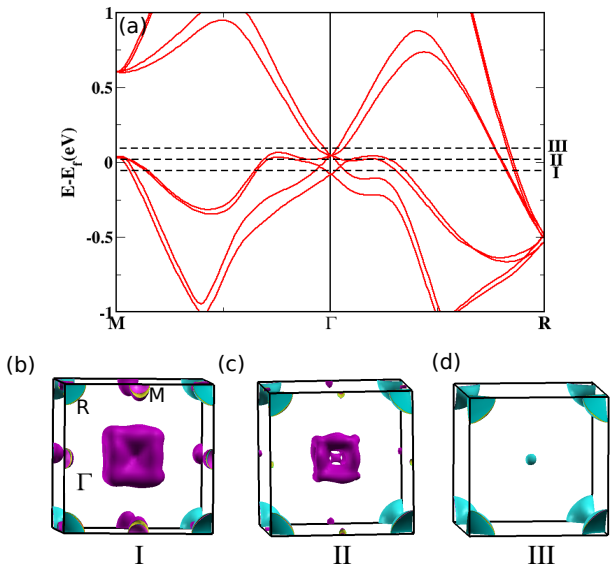

Figure 7.3: (a) Band structure of RhSi along the M-Γ-R direction, computed within GGA+U+SOC using $U = 2.5$ eV on the Rh d orbitals. The corresponding Fermi surfaces for three distinct Fermi levels, labeled as I, II, and III, are displayed in panels (b), (c), and (d), respectively. These represent doping levels of 0.05 holes, 0.04 electrons, and 0.09 electrons.

initially with temperature and then saturates to an almost constant value between 100 K and 400 K. In case III (0.09 electrons doped), the Seebeck coefficient becomes negative, indicating that electrons are now the dominant carriers. It decreases with temperature at first, and subsequently flattens out beyond 300 K. These changes in the sign and behavior of the Seebeck coefficient across different doping levels further support the occurrence of successive Lifshitz transitions.

The temperature dependence of the isobaric Seebeck coefficient can be written as, [59]

$$S = -\frac{k_B T \beta}{e\eta} \int \frac{\partial n(\epsilon, V)}{\partial V} f(\epsilon, T)\, d\epsilon - \frac{1}{eT\eta V} \int n(\epsilon, V) f(\epsilon, T)(1 - f(\epsilon, T))(\epsilon - \mu) d\epsilon. \quad (7.4)$$

Here, β is the volume thermal expansion coefficient, $n(\epsilon, V)$ represents the density of states, and $f(\epsilon, T)$ denotes the Fermi-Dirac distribution function and

$$\eta = \frac{1}{V} \int n(\epsilon, V) f(\epsilon, T)(1 - f(\epsilon, T)) d\epsilon. \quad (7.5)$$

The Seebeck coefficient, as shown in Fig. 7.4, exhibits an approximately linear dependence on temperature. This behavior can arise directly from the variations in the effective mass of the charge carriers and changes in the density of states. Upon examining Eq. (7.4), it becomes evident that the first contribution originates from the thermal

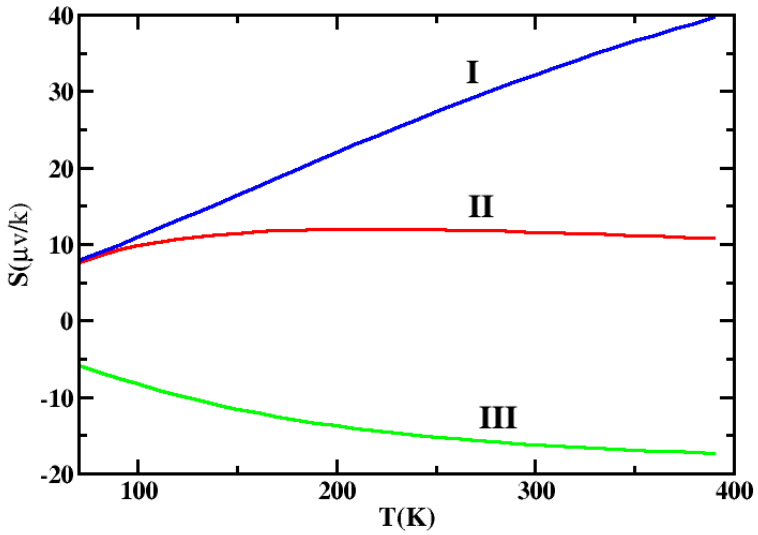

Figure 7.4: Seebeck coefficient as a function of temperature for three distinct chemical potentials—labeled I, II, and III in Fig. 7.3—corresponding to 0.05 hole doping (blue), 0.04 electron doping (red), and 0.09 electron doping (green), respectively.

expansion coefficient, while the second term refers to the temperature dependence of the carrier concentration. When the Fermi energy is located near level II, it lies close to the Weyl point. In this regime, the available phase space for thermally excited carriers diminishes with increasing temperature, resulting in a negligible temperature dependence of the Seebeck coefficient. Such behavior has previously been reported in graphene-based materials [60]. Thus, we observe pronounced changes in the Seebeck coefficient with only minimal changes in the carrier doping. This sensitivity directly reflects the modifications in the low-energy electronic structure and underscores the significance of Lifshitz transitions in determining thermoelectric behavior. To examine the influence of the electronic structure on the Seebeck coefficient, we have computed the Seebeck coefficient as a function of the Fermi energy at three different temperatures: 80 K, 90 K, and 100 K. As noted earlier, the low-energy electronic structure for $U = 0$ displays a flat band, which transforms into a double-hump feature upon incorporating correlation effects on the Rh d-orbitals. The corresponding Seebeck coefficients are shown in Fig. 7.5 for both (a) $U = 0$ and (b) $U = 2.5$ eV. While the overall temperature dependence remains qualitatively similar across both cases, noticeable differences arise in their magnitudes. For $U = 0$ eV, we observe a broad peak in the Seebeck coefficient within the energy range of 0-60 meV. This energy window corresponds to the location of the flat band in the $U = 0$ electronic structure.

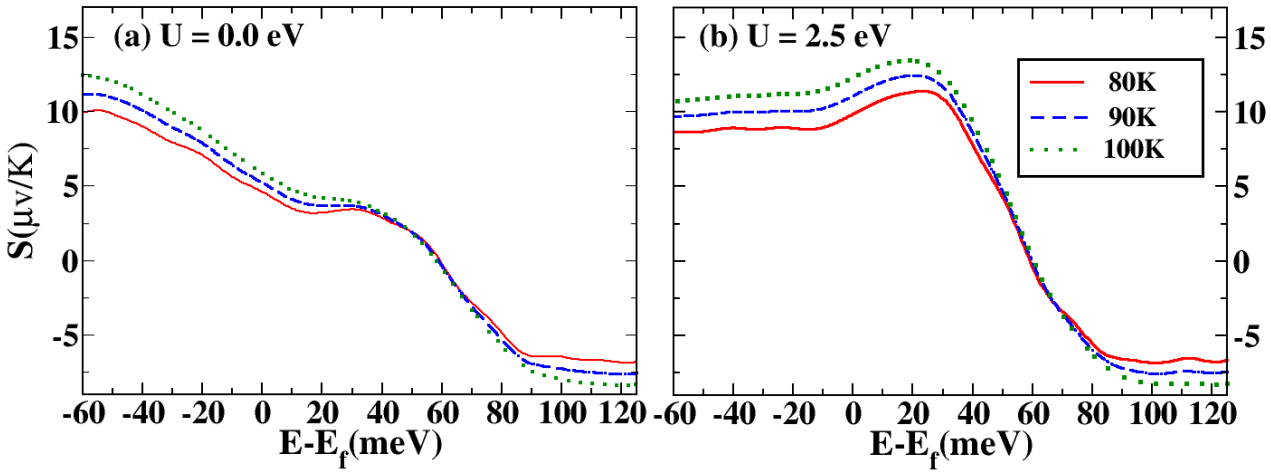

Figure 7.5: Variation of the Seebeck coefficient with Fermi energy for (a) $U = 0.0$ eV and (b) $U = 2.5$ eV applied to the Rh d orbitals, computed at temperatures of 80, 90, and 100 K.

For $U = 2.5$ eV, the same feature becomes sharper and shifts to the 0-40 meV range, aligning with the double-hump region in the modified band structure. To investigate the source of this peak, we examined the density of states within this energy interval (Fig. 7.6) and found no significant changes, indicating that the Seebeck coefficient variations arise from alterations in the band dispersion rather than in the density of states.

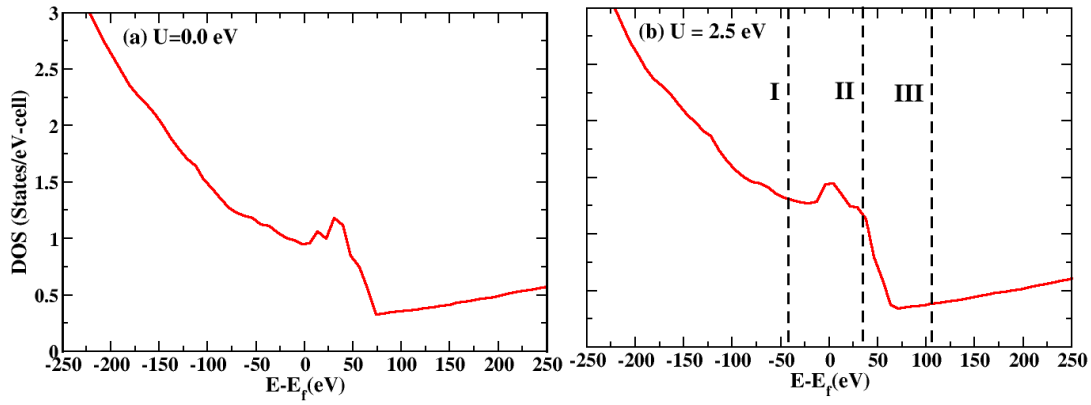

Figure 7.6: Total density of states obtained from *ab-initio* calculations for (a) $U = 0.0$ eV and (b) $U = 2.5$ eV applied to the Rh d orbitals. The Fermi level of the undoped system is taken as the reference energy (zero). Markers I, II, and III denote the Fermi levels corresponding to 0.04 hole doping, 0.05 electron doping, and 0.09 electron doping, respectively, for the $U = 2.5$ eV case.

Beyond Fermi surface topology, we further explored the topological aspects of the electronic wavefunctions by analyzing the Berry curvature distribution for $U = 2.5$ eV. Berry curvature plays a crucial role in driving various Hall effects, including the planar Hall effect [61]. Figure 7.7 shows the x-component of the Berry curvature in the $k_z = 0$

plane for the three Fermi level positions labeled I, II, and III. A slight variation in the Fermi energy leads to significant changes in the Berry curvature distribution. Notably, there is a pronounced enhancement in regions close to the Weyl point crossings at the Γ and M points.

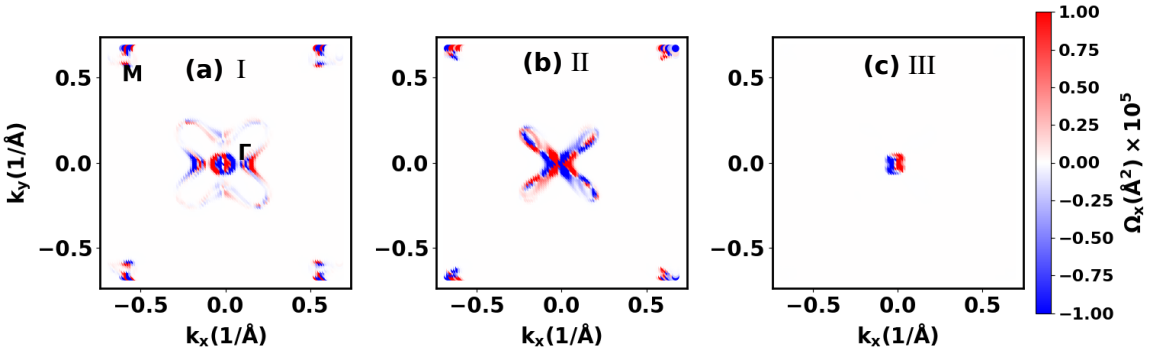

Figure 7.7: Distribution of the x-component of the Berry curvature in the $k_z = 0$ plane for three different Fermi energy values: (a) I, (b) II, and (c) III. The calculations were performed using GGA+U+SOC with $U = 2.5$ eV.

When the Fermi level corresponds to case I, the Berry curvature is primarily concentrated around Γ and M, with a slight extension from Γ toward the X direction. In region II, the distribution becomes more pronounced along the Γ–M path. For case III, the Berry curvature is predominantly localized near the Γ point. These observations indicate that even modest tuning of the Fermi level via carrier doping can effectively switch on or off the topological contributions to transport phenomena, such as the planar Hall effect.

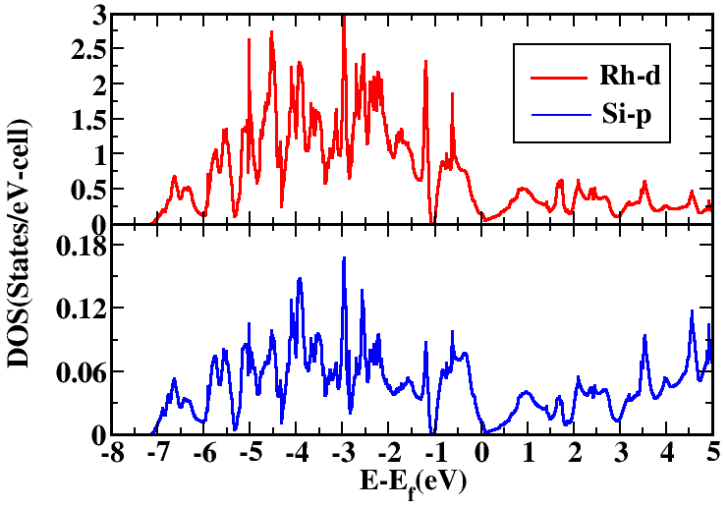

Figure 7.8: Orbital projected density of states for Rh d (top panel) and Si p (bottom panel) orbitals obtained from *ab initio* calculations with $U = 2.5$ eV applied to the Rh d states. The zero of the energy scale is set as Fermi energy.

To further investigate the origin of the double-hump structure observed in the band dispersion, we mapped the *ab initio* band structure onto a tight-binding model constructed using a basis comprising Rh d and Si p orbitals. A satisfactory agreement between the *ab initio* and tight-binding band structures was achieved and the spatial spread of each Wannier function is summarized in Table 7.1. Using this tight-binding framework, we systematically varied model parameters to identify the microscopic origin of the observed features. Specifically, we found that decreasing the on-site energies of the Si-p orbitals significantly affects this feature. The modified electronic structure which is obtained by lowering the Si-p on-site energies by 10 eV is presented in Fig. 7.9. Notably, the characteristic double-hump feature around the Γ point is completely suppressed and does not revert to a flat-band-like dispersion.

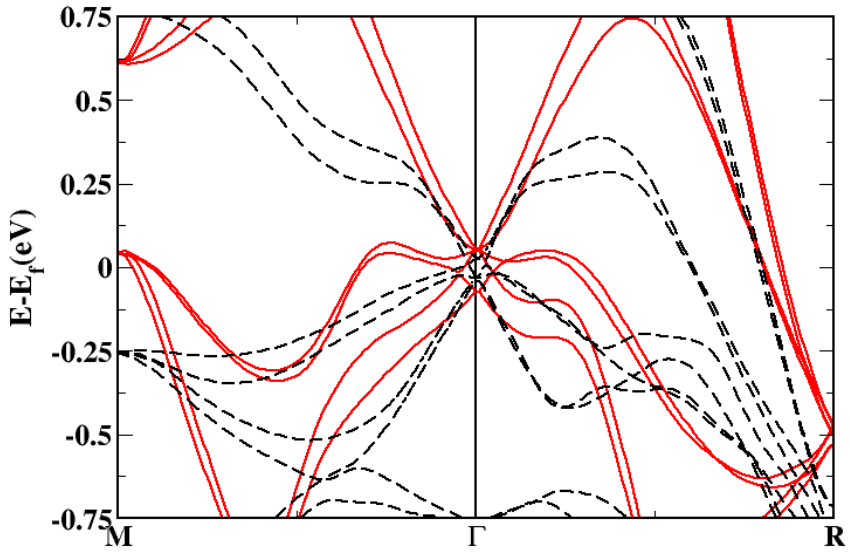

Figure 7.9: The electronic band dispersions along the M-Γ-R symmetry direction from the tight-binding model of RhSi. The red curve denotes the original band structure, while the black curve corresponds to the modified model with the on-site energies of the Si-p orbitals reduced by 10 eV. The bands are aligned at the Weyl point at the Γ point for comparison.

An examination of the electronic structure projected onto atomic orbitals reveals that the Rh-d states dominate near the Fermi level (Fig. 7.8), and might therefore be presumed to control the low-energy physics. Specifically, the interaction between Rh d and Si p orbitals plays a non-negligible role in shaping the electronic structure. The interplay between Rh d–Rh d and Rh d–Si p interactions,each possessing distinct momentum (k) dependencies,gives rise to the double-hump feature in the band dispersion. When the on-site energies of the Si-p orbitals are artificially reduced, the corresponding states are pushed deeper into the valence band. As a result, the effective interactions between Rh d and Si p states diminishes, leading to the disappearance of the double-hump structure.

This highlights the crucial role of Rh–Si hybridization in the emergence of the observed low-energy features.

7.4 Conclusions

Multiple Lifshitz transitions near Fermi energy arise due to the on-site Coulomb interaction introduced by the Hubbard U on the Rh d orbitals. The microscopic origin of these transitions is attributed to the interplay between competing Rh d–Si p and Rh d–Rh d interactions. Given that the hybridization between Rh d and Si p states plays a significant contribution in shaping the low-energy electronic structure, it is of interest to also consider effective non-local Coulomb interactions between electrons on these distinct atomic sites. This intersite interaction, denoted by V, can be incorporated within an extended Hubbard framework such as DFT+U+V [62], or through more sophisticated many-body techniques like the GW+EDMFT scheme [63], which account for both local and non-local interactions as well as dynamic screening effects.

The impact of multiple Lifshitz transitions induced by small shifts in the Fermi energy has been examined through the temperature dependence of the Seebeck coefficient. Remarkably, even minimal changes in carrier concentration result in significant variations in the Seebeck response. When the Fermi level lies near a Weyl point, the Seebeck coefficient becomes nearly temperature-independent. This behavior arises due to the reduction in phase space volume available for thermally excited carriers. Moreover, these Fermi energy shifts also alter the Berry curvature distribution, which can manifest in transport measurements, providing further evidence of the topological nature of the underlying electronic structure.

Bibliography

[1] Shuichi Murakami. Phase transition between the quantum spin hall and insulator phases in 3d: emergence of a topological gapless phase. *New Journal of Physics*, 9(9):356, sep 2007.

[2] Xiangang Wan, Ari M. Turner, Ashvin Vishwanath, and Sergey Y. Savrasov. Topological semimetal and Fermi-arc surface states in the electronic structure of pyrochlore iridates. *Phys. Rev. B*, 83:205101, May 2011.

[3] A. A. Burkov and Leon Balents. Weyl semimetal in a Topological Insulator Multilayer. *Phys. Rev. Lett.*, 107:127205, Sep 2011.

[4] Shin-Ming Huang, Su-Yang Xu, Ilya Belopolski, Chi-Cheng Lee, Guoqing Chang, BaoKai Wang, Nasser Alidoust, Guang Bian, Madhab Neupane, Chenglong Zhang, Shuang Jia, Arun Bansil, Hsin Lin, and M. Zahid Hasan. A Weyl Fermion semimetal with surface Fermi arcs in the transition metal monopnictide TaAs class. *Nature Communications*, 6(1):7373, Jun 2015.

[5] Hongming Weng, Chen Fang, Zhong Fang, B. Andrei Bernevig, and Xi Dai. Weyl Semimetal Phase in Noncentrosymmetric Transition-Metal Monophosphides. *Phys. Rev. X*, 5:011029, Mar 2015.

[6] Su-Yang Xu, Ilya Belopolski, Nasser Alidoust, Madhab Neupane, Guang Bian, Chenglong Zhang, Raman Sankar, Guoqing Chang, Zhujun Yuan, Chi-Cheng Lee, Shin-Ming Huang, Hao Zheng, Jie Ma, Daniel S. Sanchez, BaoKai Wang, Arun Bansil, Fangcheng Chou, Pavel P. Shibayev, Hsin Lin, Shuang Jia, and M. Zahid Hasan. Discovery of a Weyl fermion semimetal and topological Fermi arcs. *Science*, 349(6248):613–617, Aug 2015.

[7] N. Xu, H. M. Weng, B. Q. Lv, C. E. Matt, J. Park, F. Bisti, V. N. Strocov, D. Gawryluk, E. Pomjakushina, K. Conder, N. C. Plumb, M. Radovic, G. Autès, O. V. Yazyev, Z. Fang, X. Dai, T. Qian, J. Mesot, H. Ding, and M. Shi. Observation of Weyl nodes and Fermi arcs in tantalum phosphide. *Nature Communications*, 7(1):11006, Mar 2016.

[8] B. Q. Lv, H. M. Weng, B. B. Fu, X. P. Wang, H. Miao, J. Ma, P. Richard, X. C. Huang, L. X. Zhao, G. F. Chen, Z. Fang, X. Dai, T. Qian, and H. Ding. Experimental Discovery of Weyl Semimetal TaAs. *Phys. Rev. X*, 5:031013, Jul 2015.

[9] B. Q. Lv, N. Xu, H. M. Weng, J. Z. Ma, P. Richard, X. C. Huang, L. X. Zhao, G. F. Chen, C. E. Matt, F. Bisti, V. N. Strocov, J. Mesot, Z. Fang, X. Dai, T. Qian, M. Shi, and H. Ding. Observation of Weyl nodes in TaAs. *Nature Physics*, 11(9):724–727, Sep 2015.

[10] L. X. Yang, Z. K. Liu, Y. Sun, H. Peng, H. F. Yang, T. Zhang, B. Zhou, Y. Zhang, Y. F. Guo, M. Rahn, D. Prabhakaran, Z. Hussain, S.-K. Mo, C. Felser, B. Yan, and Y. L. Chen. Weyl semimetal phase in the non-centrosymmetric compound TaAs. *Nature Physics*, 11(9):728–732, Sep 2015.

[11] D. F. Liu, A. J. Liang, E. K. Liu, Q. N. Xu, Y. W. Li, C. Chen, D. Pei, W. J. Shi, S. K. Mo, P. Dudin, T. Kim, C. Cacho, G. Li, Y. Sun, L. X. Yang, Z. K. Liu, S. S. P. Parkin, C. Felser, and Y. L. Chen. Magnetic Weyl semimetal phase in a Kagomé crystal. *Science*, 365(6459):1282–1285, Sep 2019.

[12] Noam Morali, Rajib Batabyal, Pranab Kumar Nag, Enke Liu, Qiunan Xu, Yan Sun, Binghai Yan, Claudia Felser, Nurit Avraham, and Haim Beidenkopf. Fermi-arc diversity on surface terminations of the magnetic Weyl semimetal $Co_3Sn_2S_2$. *Science*, 365(6459):1286–1291, Sep 2019.

[13] Ilya Belopolski, Kaustuv Manna, Daniel S. Sanchez, Guoqing Chang, Benedikt Ernst, Jiaxin Yin, Songtian S. Zhang, Tyler Cochran, Nana Shumiya, Hao Zheng, Bahadur Singh, Guang Bian, Daniel Multer, Maksim Litskevich, Xiaoting Zhou, Shin-Ming Huang, Baokai Wang, Tay-Rong Chang, Su-Yang Xu, Arun Bansil, Claudia Felser, Hsin Lin, and M. Zahid Hasan. Discovery of topological Weyl fermion lines and drumhead surface states in a room temperature magnet. *Science*, 365(6459):1278–1281, Sep 2019.

[14] Zhicheng Rao, Quanxin Hu, Shangjie Tian, Qing Qu, Congrun Chen, Shunye Gao, Zhenyu Yuan, Cenyao Tang, Wenhui Fan, Jierui Huang, Yaobo Huang, Li Wang, Lu Zhang, Fangsen Li, Kedong Wang, Huaixin Yang, Hongming Weng, Tian Qian, Jinpeng Xu, Kun Jiang, Hechang Lei, Yu-Jie Sun, and Hong Ding. Charge instability of topological Fermi arcs in chiral crystal CoSi. *Science Bulletin*, 68(2):165–172, 2023.

[15] S. Geller and E. A. Wood. The crystal structure of rhodium silicide, RhSi. *Acta Crystallographica*, 7(5):441–443, May 1954.

[16] I Engstrom and Torsten Johnsson. Least-Squares Refinement of the Structure of RhSi (FeSi-type). *Acta Chemica Scandinavica*, 19(6):1508, 1965.

[17] Guoqing Chang, Su-Yang Xu, Benjamin J. Wieder, Daniel S. Sanchez, Shin-Ming Huang, Ilya Belopolski, Tay-Rong Chang, Songtian Zhang, Arun Bansil, Hsin Lin, and M. Zahid Hasan. Unconventional Chiral Fermions and Large Topological Fermi Arcs in RhSi. *Phys. Rev. Lett.*, 119:206401, Nov 2017.

[18] Peizhe Tang, Quan Zhou, and Shou-Cheng Zhang. Multiple Types of Topological Fermions in Transition Metal Silicides. *Phys. Rev. Lett.*, 119:206402, Nov 2017.

[19] Nico Huber, Kirill Alpin, Grace L Causer, Lukas Worch, Andreas Bauer, Georg Benka, Moritz M Hirschmann, Andreas P Schnyder, Christian Pfleiderer, and Marc A

Wilde. Network of topological nodal planes, multifold degeneracies, and Weyl points in CoSi. *Physical Review Letters*, 129(2):026401, 2022.

[20] Zhicheng Rao, Hang Li, Tiantian Zhang, Shangjie Tian, Chenghe Li, Binbin Fu, Cenyao Tang, Le Wang, Zhilin Li, Wenhui Fan, Jiajun Li, Yaobo Huang, Zhehong Liu, Youwen Long, Chen Fang, Hongming Weng, Youguo Shi, Hechang Lei, Yujie Sun, Tian Qian, and Hong Ding. Observation of unconventional chiral fermions with long Fermi arcs in CoSi. *Nature*, 567(7749):496–499, Mar 2019.

[21] Daichi Takane, Zhiwei Wang, Seigo Souma, Kosuke Nakayama, Takechika Nakamura, Hikaru Oinuma, Yuki Nakata, Hideaki Iwasawa, Cephise Cacho, Timur Kim, Koji Horiba, Hiroshi Kumigashira, Takashi Takahashi, Yoichi Ando, and Takafumi Sato. Observation of Chiral Fermions with a Large Topological Charge and Associated Fermi-Arc Surface States in CoSi. *Phys. Rev. Lett.*, 122:076402, Feb 2019.

[22] Daniel S. Sanchez, Tyler A. Cochran, Ilya Belopolski, Zi-Jia Cheng, Xian P. Yang, Yiyuan Liu, Tao Hou, Xitong Xu, Kaustuv Manna, Chandra Shekhar, Jia-Xin Yin, Horst Borrmann, Alla Chikina, Jonathan D. Denlinger, Vladimir N. Strocov, Weiwei Xie, Claudia Felser, Shuang Jia, Guoqing Chang, and M. Zahid Hasan. Tunable topologically driven Fermi arc van Hove singularities. *Nature Physics*, 19(5):682–688, May 2023.

[23] Fernando de Juan, Adolfo G. Grushin, Takahiro Morimoto, and Joel E. Moore. Quantized circular photogalvanic effect in Weyl semimetals. *Nature Communications*, 8(1):15995, Jul 2017.

[24] Dylan Rees, Kaustuv Manna, Baozhu Lu, Takahiro Morimoto, Horst Borrmann, Claudia Felser, J. E. Moore, Darius H. Torchinsky, and J. Orenstein. Helicity-dependent photocurrents in the chiral Weyl semimetal RhSi. *Science Advances*, 6(29):0509, 2020.

[25] Zhuoliang Ni, K. Wang, Y. Zhang, O. Pozo, B. Xu, X. Han, K. Manna, J. Paglione, C. Felser, A. G. Grushin, F. de Juan, E. J. Mele, and Liang Wu. Giant topological longitudinal circular photo-galvanic effect in the chiral multifold semimetal CoSi. *Nature Communications*, 12(1):154, Jan 2021.

[26] Ching-Kit Chan, Netanel H. Lindner, Gil Refael, and Patrick A. Lee. Photocurrents in Weyl semimetals. *Phys. Rev. B*, 95:041104, Jan 2017.

[27] Qiong Ma, Su-Yang Xu, Ching-Kit Chan, Cheng-Long Zhang, Guoqing Chang, Yuxuan Lin, Weiwei Xie, Tomás Palacios, Hsin Lin, Shuang Jia, Patrick A. Lee, Pablo

Jarillo-Herrero, and Nuh Gedik. Direct optical detection of Weyl fermion chirality in a topological semimetal. *Nature Physics*, 13(9):842–847, Sep 2017.

[28] Shudan Zhong, Joel E. Moore, and Ivo Souza. Gyrotropic Magnetic Effect and the Magnetic Moment on the Fermi Surface. *Phys. Rev. Lett.*, 116:077201, Feb 2016.

[29] Jing Ma and D. A. Pesin. Chiral magnetic effect and natural optical activity in metals with or without Weyl points. *Phys. Rev. B*, 92:235205, Dec 2015.

[30] Chen Fang, Ling Lu, Junwei Liu, and Liang Fu. Topological semimetals with helicoid surface states. *Nature Physics*, 12(10):936–941, Oct 2016.

[31] P. Hohenberg and W. Kohn. Inhomogeneous Electron Gas. *Phys. Rev.*, 136:B864–B871, Nov 1964.

[32] W. Kohn and L. J. Sham. Self-Consistent Equations Including Exchange and Correlation Effects. *Phys. Rev.*, 140:A1133–A1138, Nov 1965.

[33] Geng Li, Haitao Yang, Peijie Jiang, Cong Wang, Qiuzhen Cheng, Shangjie Tian, Guangyuan Han, Chengmin Shen, Xiao Lin, Hechang Lei, Wei Ji, Ziqiang Wang, and Hong-Jun Gao. Chirality locking charge density waves in a chiral crystal. *Nature Communications*, 13(1):2914, May 2022.

[34] Paromita Dutta and Sudhir K. Pandey. Studying the electronic structure of FeSi & CoSi by using DFT+DMFT. *AIP Conference Proceedings*, 2115(1):030347, Jul 2019.

[35] Paromita Dutta and Sudhir K. Pandey. Electronic correlation effect on nontrivial topological fermions in CoSi. *The European Physical Journal B*, 94(4):81, Apr 2021.

[36] Krishnendu Patra, Viktor Christiansson, Ferdi Aryasetiawan, and Priya Mahadevan. Origin of multiple lifshitz transitions in the weyl semi-metal rhsi, 2024.

[37] F. Aryasetiawan, M. Imada, A. Georges, G. Kotliar, S. Biermann, and A. I. Lichtenstein. Frequency-dependent local interactions and low-energy effective models from electronic structure calculations. *Phys. Rev. B*, 70:195104, Nov 2004.

[38] IM Lifshitz. Anomalies of electron characteristics of a metal in the high pressure region. *Sov. Phys. JETP*, 11(5):1130–1135, 1960.

[39] VG Vaks, AV Trefilov, and SV Fomichev. Singularities of resistivity and thermoelectric power of metals in phase transitions of order $2\frac{1}{2}$. *Th. Eksp. Teor. Fiz*, 80:1613, 1981.

[40] H. F. Yang, L. X. Yang, Z. K. Liu, Y. Sun, C. Chen, H. Peng, M. Schmidt, D. Prabhakaran, B. A. Bernevig, C. Felser, B. H. Yan, and Y. L. Chen. Topological Lifshitz transitions and Fermi arc manipulation in Weyl semimetal NbAs. *Nature Communications*, 10(1):3478, Aug 2019.

[41] N. Xu, Z. W. Wang, A. Magrez, P. Bugnon, H. Berger, C. E. Matt, V. N. Strocov, N. C. Plumb, M. Radovic, E. Pomjakushina, K. Conder, J. H. Dil, J. Mesot, R. Yu, H. Ding, and M. Shi. Evidence of a Coulomb-Interaction-Induced Lifshitz Transition and Robust Hybrid Weyl Semimetal in T_d-MoTe_2. *Phys. Rev. Lett.*, 121:136401, Sep 2018.

[42] M. R. Norman, Jie Lin, and A. J. Millis. Lifshitz transition in underdoped cuprates. *Phys. Rev. B*, 81:180513, May 2010.

[43] X. Shi, Z.-Q. Han, X.-L. Peng, P. Richard, T. Qian, X.-X. Wu, M.-W. Qiu, S. C. Wang, J. P. Hu, Y.-J. Sun, and H. Ding. Enhanced superconductivity accompanying a Lifshitz transition in electron-doped FeSe monolayer. *Nature Communications*, 8(1):14988, Apr 2017.

[44] P. E. Blöchl. Projector augmented-wave method. *Phys. Rev. B*, 50:17953–17979, Dec 1994.

[45] G. Kresse and J. Hafner. Ab initio molecular dynamics for liquid metals. *Phys. Rev. B*, 47:558–561, Jan 1993.

[46] G. Kresse and J. Hafner. Ab initio molecular-dynamics simulation of the liquid-metal-amorphous-semiconductor transition in germanium. *Phys. Rev. B*, 49:14251–14269, May 1994.

[47] G. Kresse and J. Furthmüller. Efficient iterative schemes for ab initio total-energy calculations using a plane-wave basis set. *Phys. Rev. B*, 54:11169–11186, Oct 1996.

[48] John P. Perdew, Kieron Burke, and Matthias Ernzerhof. Generalized Gradient Approximation Made Simple. *Phys. Rev. Lett.*, 77:3865–3868, Oct 1996.

[49] S. L. Dudarev, G. A. Botton, S. Y. Savrasov, C. J. Humphreys, and A. P. Sutton. Electron-energy-loss spectra and the structural stability of nickel oxide: An LSDA+U study. *Phys. Rev. B*, 57:1505–1509, Jan 1998.

[50] Hendrik J. Monkhorst and James D. Pack. Special points for Brillouin-zone integrations. *Phys. Rev. B*, 13:5188–5192, Jun 1976.

[51] Arash A. Mostofi, Jonathan R. Yates, Young-Su Lee, Ivo Souza, David Vanderbilt, and Nicola Marzari. wannier90: A tool for obtaining maximally-localised Wannier functions. *Computer Physics Communications*, 178(9):685–699, 2008.

[52] C Franchini, R Kováčik, M Marsman, S Sathyanarayana Murthy, J He, C Ederer, and G Kresse. Maximally localized Wannier functions in $LaMnO_3$ within PBE+U, hybrid functionals and partially self-consistent GW: an efficient route to construct ab initio tight-binding parameters for e_g perovskites. *Journal of Physics: Condensed Matter*, 24(23):235602, may 2012.

[53] QuanSheng Wu, ShengNan Zhang, Hai-Feng Song, Matthias Troyer, and Alexey A. Soluyanov. Wanniertools: An open-source software package for novel topological materials. *Computer Physics Communications*, 224:405–416, 2018.

[54] Georg K.H. Madsen, Jesús Carrete, and Matthieu J. Verstraete. BoltzTraP2, a program for interpolating band structures and calculating semi-classical transport coefficients. *Computer Physics Communications*, 231:140–145, 2018.

[55] Georg K.H. Madsen and David J. Singh. BoltzTraP. A code for calculating band-structure dependent quantities. *Computer Physics Communications*, 175(1):67–71, 2006.

[56] Raveena Gupta, Baljinder Kaur, Jesús Carrete, and Chandan Bera. A theoretical model of the thermoelectric properties of SnS_xSe_{1-x} and how to further enhance its thermoelectric performance. *Journal of Applied Physics*, 126(22):225105, Dec 2019.

[57] Naoko Ito, Mayu Ishii, and Ryuji Okazaki. Enhanced Seebeck coefficient by a filling-induced Lifshitz transition in K_xRhO_2. *Phys. Rev. B*, 99:041112, Jan 2019.

[58] Yoshihiko Okamoto, Atsushi Nishio, and Zenji Hiroi. Discontinuous Lifshitz transition achieved by band-filling control in Na_xCoO_2. *Phys. Rev. B*, 81:121102, Mar 2010.

[59] Yi Wang, Yong-Jie Hu, Brandon Bocklund, Shun-Li Shang, Bi-Cheng Zhou, Zi-Kui Liu, and Long-Qing Chen. First-principles thermodynamic theory of seebeck coefficients. *Phys. Rev. B*, 98:224101, Dec 2018.

[60] Seung-Geol Nam, Dong-Keun Ki, and Hu-Jong Lee. Thermoelectric transport of massive dirac fermions in bilayer graphene. *Phys. Rev. B*, 82:245416, Dec 2010.

[61] S. Nandy, Gargee Sharma, A. Taraphder, and Sumanta Tewari. Chiral anomaly as the origin of the planar hall effect in weyl semimetals. *Phys. Rev. Lett.*, 119:176804, Oct 2017.

[62] Vivaldo Leiria Campo and Matteo Cococcioni. Extended DFT + U + V method with on-site and inter-site electronic interactions. *Journal of Physics: Condensed Matter*, 22(5):055602, jan 2010.

[63] S. Biermann, F. Aryasetiawan, and A. Georges. First-Principles Approach to the Electronic Structure of Strongly Correlated Systems: Combining the *GW* Approximation and Dynamical Mean-Field Theory. *Phys. Rev. Lett.*, 90:086402, Feb 2003.

Chapter 8

Conclusion and Outlook

In this thesis, I have primarily investigated the unconventional ordered states observed in transition metal compounds, most of which involve 3d electrons and exhibit strong electronic correlations. We have also attempted to understand the various features of their ground states.

In the case of $NdNiO_3$, we have examined the behavior of the bond-disproportionated phase under both hole and electron doping. At low doping concentrations, the additional charge carriers do not distribute uniformly across the lattice, instead, they tend to localize on specific Ni atoms, leading to the formation of polaronic states. The bond-disproportionated phase is known to be stable only within a certain range of negative charge-transfer energy (Δ), and any deviation from this range whether by increasing or decreasing Δ can destabilize the phase. Our DFT calculations show that changes in Δ due to doping are not uniform but depend on the local environment of each Ni site. When a hole or electron becomes trapped at a particular Ni atom, the corresponding change in Δ remains within the stability range for bond disproportionation. As a result, instead of completely suppressing the bond-disproportionated state, low levels of doping induce a transformation of Ni^{2+} and Ni^{4+} ions into intermediate Ni^{3+} states. Moreover, the unoccupied Ni $4p$ density of states serves as an effective experimental probe,distinguishing not only Ni^{2+} and Ni^{4+} but also doping-induced Ni^{3+} states. This phenomenon can be verified through observations of the shift in the Ni K absorption edge via X-ray absorption spectroscopy. For future studies, the presence of this polaronic state needs a quantitative model that incorporates all relevant aspects of this regime to accurately predict the relative energetics and identify when the crossover occur.

Next, we investigated the magnetic ground state of Ca_3CoMnO_6 in the ordered limit and demonstrated that the so-called uudd magnetic configuration can be stabilized by positional disorder. Here we have used the Heisenberg model to determine the nature of exchange interaction. Constructing a tight binding model, we quantified the strength of hopping interactions in different exchange pathways by evaluating the change in total energy upon switching off the specific hopping pathways. We revealed that the dominant contribution arises primarily from nearest-neighbor interactions, which are mediated through non-magnetic ligand atoms. For this study, we considered only the ground-state magnetic configuration and examined various exchange pathways. This approach provides insight into the relative interaction strengths in different hopping pathways and enables

the construction of a minimal model that captures the essential features of the magnetic ground state.

In the Heisenberg case, the nature of this exchange interactions is predicted by treating hopping as a perturbation. However, in the next project we have shown that by incorporating Coulomb interactions into the tight-binding model, we can not only capture the relative hopping strength across different exchange pathways but also determine whether the exchange interaction is antiferromagnetic or ferromagnetic. Our model operates under the mean-field approximation and does not treat hopping as a perturbation. We applied this model to examine magnetism in 25% Fe-intercalated $NbSe_2$. The tight-binding part was derived by mapping the DFT band structure onto a tight-binding model using Wannier functions. The results obtained from this model are consistent with DFT+U calculations. To analyze the interactions, we selectively switched off different interactions and computed the energy gain, comparing it across various magnetic configurations while keeping the optimized structure fixed. Using this model, we can capture the exchange interaction without taking multiple complex magnetic configurations.

We then examined the transport properties in altermagnet CrSb. For the first time, we demonstrated that CrSb can exhibit direction-dependent conduction polarity (DDCP) over a narrow energy window supported by the experiment, which holds promising potential for spintronic applications. We proposed that this phenomenon originates from a multiband carrier mechanism, and we supported this by calculating the average effective mass through interpolation of DFT data. Our results suggest that the nature of the polarity can be inferred from the average effective mass calculated over the Fermi surface.

Lastly, we explored RhSi, a topological Weyl semimetal. By introducing a finite Coulomb interaction (U), we observed the emergence of a double-hump structure in the electronic band dispersion, corresponding to multiple Lifshitz transition points. This feature holds significant implications for both thermoelectric and strongly correlated systems. We analyzed how thermal transport, quantified by the Seebeck coefficient, undergoes notable changes in the low-energy regime near the Fermi level while remaining nearly constant with temperature near the Weyl point due to the reduced phase space for thermally excited carriers. Additionally, topological features such as the Berry curvature exhibit pronounced variations in this regime. Our findings suggest that doping-induced tuning of the chemical potential could control both transport properties and topological characteristics. Furthermore, we investigated how modifying the Rh-d, Rh-d, and Rh-d, Si-p orbital interactions can be used to manipulate the double-hump feature, offering a pathway for engineering electronic and topological behavior in such systems.